The Philosophical Magazine

FIRST PUBLISHED IN 1798

A Journal of Theoretical Experimental and Applied Physics

Vol. 3 April 1958 No. 28
Eighth Series

£1 5s. 0d., plus postage
Annual Subscription £13 10s. 0d., payable in advance

Printed and Published by
TAYLOR & FRANCIS LTD
RED LION COURT, FLEET STREET, LONDON, E.C.4

THE PHILOSOPHICAL MAGAZINE

Authors wishing to submit papers for publication in the Journal should send manuscripts directly to the Publishers.

Manuscripts should be typed in *double* spacing on one side of quarto (8×10 in.) paper, and authors are urged to aim at absolute clarity of meaning and an attractive presentation of their texts.

References should be listed at the end in alphabetical order of authors and should be cited in the text in terms of author's name and date. Diagrams should normally be in Indian ink on white card, with lettering in soft pencil, the captions being typed on a separate sheet.

A leaflet giving detailed instructions to authors on the preparation of papers is available on request from the Publishers.

Authors are entitled to receive 25 offprints of a paper in the Journal free of charge, and additional offprints can be obtained from the Publishers.

The *Philosophical Magazine* and its companion journal, *Advances in Physics*, will accept papers for publication in experimental and theoretical physics. The *Philosophical Magazine* publishes contributions describing new results, letters to the editor and book reviews. *Advances in Physics* publishes articles surveying the present state of knowledge in any branch of the science in which recent progress has been made. The editors welcome contributions from overseas as well as from the United Kingdom, and papers may be published in English, French and German.

The Magnetic Susceptibility and Electrical Resistivity of Some Transition Metal Silicides†

By D. A. Robins
Research Laboratories of The General Electric Company Limited, Wembley, England

[Received October 30, 1957]

Abstract

Sintered samples have been prepared of a number of silicides formed by the Groups IVa, Va and VIa transition metals and silicon. Magnetic susceptibility measurements have been made at room temperature and 500°c and the electrical resistivity and temperature coefficient of resistivity determined for the range 20°c to 120°c. The results are discussed in relation to the type of bonding present in these compounds and it is shown that the transition metal silicides are essentially metallic in character.

§ 1. Introduction

The transition metals form with silicon a series of compounds which are in many ways analogous to the transition metal carbides. As for carbides, the most stable silicides are those containing metals from Groups IVa Va and VIa of the periodic table. Many of these silicides have high melting points and their apparent refractory nature is evidenced by extreme room temperature brittleness. The limited and sometimes conflicting published data on the electrical properties of these compounds show, however, that they possess high electrical conductivity and, at least in the case of molybdenum disilicide, a positive temperature coefficient of resistivity (Glaser 1951). The present paper reports the results of some magnetic and electrical measurements which have been carried out on some of the more stable silicides in order to gain information on the type of bonding present in these materials.

§ 2. Experimental Method

It has been shown that specific homogeneous silicides can be prepared by mixing together silicon powder with the required quantity of metal powder and then heating a compact of the mixture to produce reaction (Robins and Jenkins 1955). This method of preparation has been employed in the present investigation using the same starting materials as in the earlier work. The mixed powders were pressed into bars and then heated in a static atmosphere of argon (99·7%) to a temperature at which reaction took place. The temperature required varied between

† Communicated by the Author.

1300°c and 1550°c for the different mixtures. The reaction product was crushed to a powder which would pass through a 200 mesh screen and the powder was subjected to x-ray examination to confirm that the material was both single phase and homogeneous.

2.1. *Magnetic Susceptibility Measurements*

Susceptibility measurements were made on both powdered silicides and on sintered compacts by measuring the force on a sample held in an inhomogeneous magnetic field. The sintered compacts were prepared by compacting powder in a brass die at 10 tons/in^2 and then treating the compacts in the manner listed in table 1. It had been shown previously that no change in the silicide would be expected to take place during the sintering process (Robin and Jenkins 1956). After sintering, the compacts were all ground to the same size (6.30 mm dia. and 1·25 mm thick) care being taken to prevent any possible contamination by ferromagnetic impurities.

For the examination of powders, the samples were placed in a small flat-bottomed silica container (6 mm dia.) which was filled to a constant depth of 1·5 mm with a known weight of powder. The container was supported by a silica rod between the flat pole pieces of an electromagnet, and the upper end of the silica rod was attached to a Sucksmith balance. For measurements on sintered samples the specimens were attached to the silica rod by a small cradle of thin platinum wire. During the experiments at room temperature the pole faces of the magnet were spaced 1 cm apart, but for measurements at elevated temperatures the separation was increased to 2·5 cm to allow a non-inductively wound platinum furnace to be placed around the specimen. Measurements on each sample were carried out at three different current settings for the magnet and at least three determinations of the displacement were made at each setting. Before each measurement the electromagnet was moved in a vertical direction until the specimen was in that part of the field where $H(dH/dx)$ was largest, this position giving the maximum deflection. The measured deflections were corrected for the effect of the holder and supports.

Since the method of measurement of susceptibility employed was only comparative, a sample of high purity tantalum ground to the same dimensions as the sintered compacts was used as a standard sample. To confirm that the measuring technique was satisfactory, titanium and zirconium compacts were prepared by compacting and sintering metal hydride powder in a vacuum (Robins 1956) and the measured susceptibility values were compared with the published values for these two metals.

All the measurements on powders were only carried out at room temperature but, for many of the sintered samples, the variation in suceptibility over the temperatures range room temperature to 500°c was determined. The measurements were carried out in air and, to

Table 1. The Preparation of Sintered Compacts

Compound		Melting point °c	Sintering conditions			Density[1] of bars (g/cm³)	Density of −200 mesh powder (g/cm³)	x-ray density (g/cm³)	Density of bar × 100 / Density of silicide
Formula	Wt. % Si		Temp. °c	Time (hr.)	Atmosphere				
$TiSi_2$	54·0	1540[2]	1475	1·0	Argon	3·83	4·04	4·12	94·8
$ZrSi_2$	38·1	(1520)[3]	1450	1·0	Argon	4·42	4·79	4·91	92·3
VSi_2	52·5	1670[4]	1600	1·0	Argon	4·33	4·61	4·76	93·9
$NbSi_2$	37·7	1950[4]	1700	0·5	Argon	4·88	5·47	5·69	89·2
$TaSi_2$	23·7	2400[6]	1700	0·5	Argon	7.60	8·84	9·14	86·0
$CrSi_2$	51·9	1550[5]	1450	1·0	Hydrogen	4·60	4·91	5·01	93·7
$MoSi_2$	36·9	1870[6]	1475–1600	0·25–2·0	Hydrogen	5·23–6·03	6.10	6·28	85·7–98·9
WSi_2	23·0	2050[6]	1600–1800	1·0	Hydrogen	8·02–9·02	9·62	9·86	83·4–93·8
Ti_5Si_3	26·0	2120[2]	1550	1·0	Argon	3·82	4·27	4·31	89·5
TiSi	36·9	(1760)[2]	1400	1·0	Argon	4·00	4·18	No data	95·7
ZrSi	23·5	2100[3]	1400	1·0	Argon	4·70	5·60	5·65	83·9

[1] The densities of the compacts used for the magnetic susceptibility measurements were not determined.

[2] Hansen *et al.* 1952. [3] Kieffer *et al.* 1954.

[4] Kieffer *et al.* 1956. [5] Kieffer *et al.* 1953.

[6] Schwarzkopf and Kieffer 1953.

confirm that significant contamination by oxygen or nitrogen at the elevated temperatures had not taken place, the room temperature susceptibility measurements were made both before and after the high temperature measurements.

2.2. *Electrical Measurements*

For the resistivity measurements bars of silicide, approximately 11 cm long, 1 cm wide and 0·5 cm thick were prepared by pressing the silicide powder in a steel die at 40 tons/in^2 and then sintering the pressed bars using the treatments listed in table 1. The density of the sintered bars was measured and compared with pycnometrically determined values using the −200 mesh powder. The percentage of residual porosity could then be calculated. Densities of the silicides calculated from published x-ray data where these are available are also included in table 1. A considerable amount of residual porosity was present in some of the sintered bars and in order to assess the effect of this porosity on both the room temperature resistivity and the temperature coefficient of resistivity a number of bars of molybdenum disilicide and tungsten disilicide were prepared under different conditions to produce material of different densities. Only a limited amount of experimental work was carried out with hot pressed material due to the difficulties of preventing contamination by oxygen, nitrogen or carbon when using this technique with fine, reactive powders.

The resistivity measurements were carried out using a Kelvin bridge having an accuracy of better than 0·5% and for both room temperature and elevated temperature measurements the bar and supporting framework were contained in a long tube furnace wound non-inductively. Resitance measurements were made up to a temperature of 160°C and the temperature coefficient of resistivity calculated for the temperature range 20°C to 120°C.

§ 3. Magnetic Susceptibility Results

Assuming the room temperature magnetic susceptibility of tantalum to be $0{\cdot}84\times10^{-6}$ e.m.u./g (Kriessmann and Callen 1954), average values for the susceptibility of sintered samples of titanium and zirconium were found to be $3{\cdot}24\times10^{-6}$ and $1{\cdot}25\times10^{-6}$ e.m.u./g, respectively. A comparison of these results with the accepted values for these elements ($3{\cdot}2\times10^{-6}$ e.m.u./g for titanium and $1{\cdot}3\times10^{-6}$ e.m.u./g for zirconium) showed that the experimental technique was satisfactory. The variation of the susceptibility of tantalum with temperature over the range room temperature to 500°C also agreed with the results of Kriessmann and Callen (1954), the paramagetism decreasing linearly with increasing temperature from $0{\cdot}84\times10^{-6}$ to $0{\cdot}78\times10^{-6}$ e.m.u./g.

The results of the susceptibility measurements on both powdered and sintered silicide samples are given in table 2 each value being the average of at least three readings. Paramagnetic values are given as positive and diamagnetic values as negative. In most cases results are given for

Table 2. Magnetic Susceptibility Results

Compound	χ e.m.u./g $\times 10^6$				χ e.m.u./g mol $\times 10^6$		χ e.m.u./g atom of metal $\times 10^3$	
	Room temp. (2 amps)	Room temp. (3 amps)	Room temp. (12 amps)	500°c (12 amps)	Room temp. (12 amps)	500°c (12 amps)	Room temp.	500°c?
$TiSi_2$	+1·27	+1·27	+1·24	+1·08	+129	+112	+136	+119
$ZrSi_2$	−0·68	−0·70	−0·70	−0·77	−103	−113	−96	−106
VSi_2	+1·63	+1·53	+1·50	+1·00	+161	+107	+168	+114
$NbSi_2$	−0·23	−0·25	−0·25	—	−37	—	−30	—
$TaSi_2$	—	−0·16	−0·17	—	−40	—	−33	—
$CrSi_2$	+0·42	+0·39	+0·38	+0·33	+41	+36	+48	+43
$MoSi_2$	−0·23	−0·25	−0·24	−0·44	−36·5	−67	−29·5	−60
WSi_2	−0·35	−0·33	−0·34	−0·35	−82	−84	−75	−77
Ti_5Si_3	+2·50	+2·50	+2·54	—	+810	—	+164	—
TiSi	+0·68	+0·74	+0·72	—	+55	—	+59	—
ZrSi	−0·58	−0·57	−0·56	—	−67	—	−63	—

determinations at three different currents in the electromagnet but, particularly when carrying out measurements with powders having a small susceptibility, the deflections produced at the lowest current were too small for accurate measurement. In each case the value obtained at 12 amps was the most accurate, due to the larger deflection, and the accuracy of these values is considered to be better than $\pm 0{\cdot}05 \times 10^{-6}$ e.m.u./g. All the values have been corrected for the effect of the holder, this correction being small except where the sample has a small susceptibility. For solid specimens the deflection due to the platinum wire holder corresponded to approximately 2% of the deflection produced by the calibrating sample, and for the holder used with the powdered samples to approximately 5%.

No marked variation of susceptibility with field strength was found for any of the samples showing that ferromagnetic impurities were not affecting the results. It was known, however, that some of the powders used in the preparation of the silicides contained traces of iron and the absence of ferromagnetic impurity in the silicide was possibly due to the ferromagnetic element being present in the combined state. To confirm this a quantity of molybdenum disilicide powder was ground in a steel ball-mill to produce iron contamination, and subsequent magnetic measurements on this powder showed that significant contamination had taken place. Sintered compacts were then prepared from this contaminated powder and their susceptibility redetermined at different field strengths. The sintering treatment had caused all trace of the ferromagnetic impurity to disappear.

Table 2 also contains susceptibility values for a number of the disilicides at 500°C, and for all the samples examined no marked deviation from linearity was found for the variation of susceptibility with temperature over the range room temperature to 500°C. High temperature susceptibility measurements were not made on the niobium disilicide and tantalum disilicide samples, due to the possibility of excessive contamination by oxygen caused by the reactive nature of these materials and the high porosity of the sintered compacts.

The susceptibility values obtained at the maximum field strength for both room temperature and 500°C are recorded in table 2 as electromagnetic units per gram molecule, and assuming that the value of $-3{\cdot}65 \times 10^{-6}$ e.m.u./g atom for the susceptibility of silicon (Bates 1951) remains unchanged on combination with a transition metal, the magnetic susceptibility for a gram atom of the combined metal has been calculated. Any error introduced by this assumption is likely to be small since a change in the character of the silicon to $Si^{4+}(-1 \times 10^{-6}$ e.m.u./g ion—Selwood 1956) would alter only slightly the value obtained for the susceptibility of the metal atoms.

The disilicides of the first period transition elements were all paramagnetic, whereas the disilicides of the two later transition periods all exhibited diamagnetism. Increasing temperature increased the tendency

towards diamagnetism, although the magnitude of the effect varied considerably for different compounds. In a number of cases the diamagnetic values obtained were numerically rather high. For the lower silicides of titanium and zirconium there was a general tendency for increasing silicon content to reduce the paramagnetism, although the titanium in the compound Ti_5Si_3 had a slightly greater paramagnetism than unalloyed titanium. Conflicting data have been published regarding the compounds present in the zirconium–silicon system (Kieffer *et al.* 1954, Lundin *et al.* 1953), but a compound corresponding to Zr_5Si_3 was prepared and its magnetic susceptibility was found to be $+0{\cdot}46\times10^{-6}$ e.m.u./g corresponding to $+52\times10^{-6}$ e.m.u./g atom of metal. For the zirconium–silicon compounds, therefore, increasing silicon content did systematically reduce the paramagnetism of the metal.

Only for chromium disilicide were there any previous data with which the present results could be compared. Foëx (1938) reported for this compound a weak, temperature independent diamagnetism ($-0{\cdot}094\times10^{-6}$ e.m.u./g), whereas the material examined in the present investigation possessed a weak paramagnetism.

§ 4. Electrical Resistivity Results

The effect of residual porosity on the electrical resistivity of sintered molybdenum disilicide and tungsten disilicide compacts is shown in figs. 1 and 2, and it is apparent that the porosity had a greater effect on the resistivity than could be accounted for by the presence of isolated pores assuming that isolated porosity only reduced the effective area of cross section of the sintered bars. Examination of the samples showed, however, that only isolated porosity was in fact present, the size of the pores decreasing with increasing sintering temperature. To confirm that the different sintering temperatures for the various bars were not producing a change in the basic material, additional bars of molybdenum disilicide were prepared varying both the sintering time and the sintering temperature to give material of the same density by different sintering treatments. The resistivity values again fell on the curve given in fig. 2. As additional confirmation, sintered material was crushed to powder, compacted and resintered and again the resistivity values corresponded to the curve in fig. 1. The reason for the large variation in resistivity with density for the molybdenum and tungsten disilicide samples was not established. It was found, however, that although this variation was large, no marked variation of the temperature coefficient of resistivity with density was observed. Temperature coefficient of resistivity values determined on bars containing an appreciable amount of porosity are, therefore, likely to be more reliable than the resistivity values ; these latter values are likely to be too high.

Table 3 lists the room temperature resistivity and the temperature coefficient of resistivity over the temperature range 20°c to 120°c for the compounds studied in this investigation, the resistivity values for

molybdenum and tungsten disilicides being taken from figs. 1 and 2. Published data on resistivity, where these are available, are also listed in table 3. The high conductivity of titanium disilicide as found by Glaser and Moskowitz (1953) was confirmed, its resistivity being less than that of the pure metal. The resistivity of the zirconium disilicide samples was a little lower than that found by Gallistl for hot pressed

Fig. 1

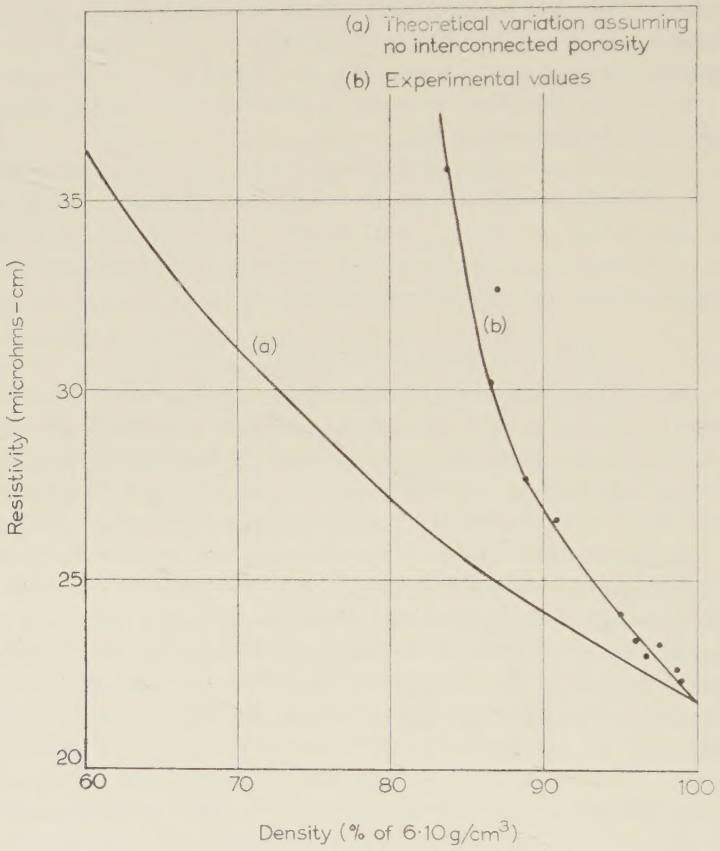

The variation of room temperature resistivity with density for sintered molybdenum disilicide.

material (and reported by Schwarzkopf and Kieffer 1953), but the resistivity was still more than double that of zirconium metal and considerably greater than the resistivity of titanium disilicide. The conductivity of the sintered vanadium disilicide was a little less than that reported for hot pressed material and this difference is possibly associated with a difference in residual porosity. A detailed study of the resistivity of niobium and tantalum disilicides was not carried out due to the large amount of porosity in the sintered samples, but some preliminary

measurements on tantalum disilicide gave a resistivity value considerably greater than that obtained by Gallistl as might be expected from the low density of the sintered material. The measured resistivity of molybdenum and tungsten disilicides agreed well with published data for these compounds (Glaser 1951, Schwarzkopf and Kieffer 1953).

Fig. 2

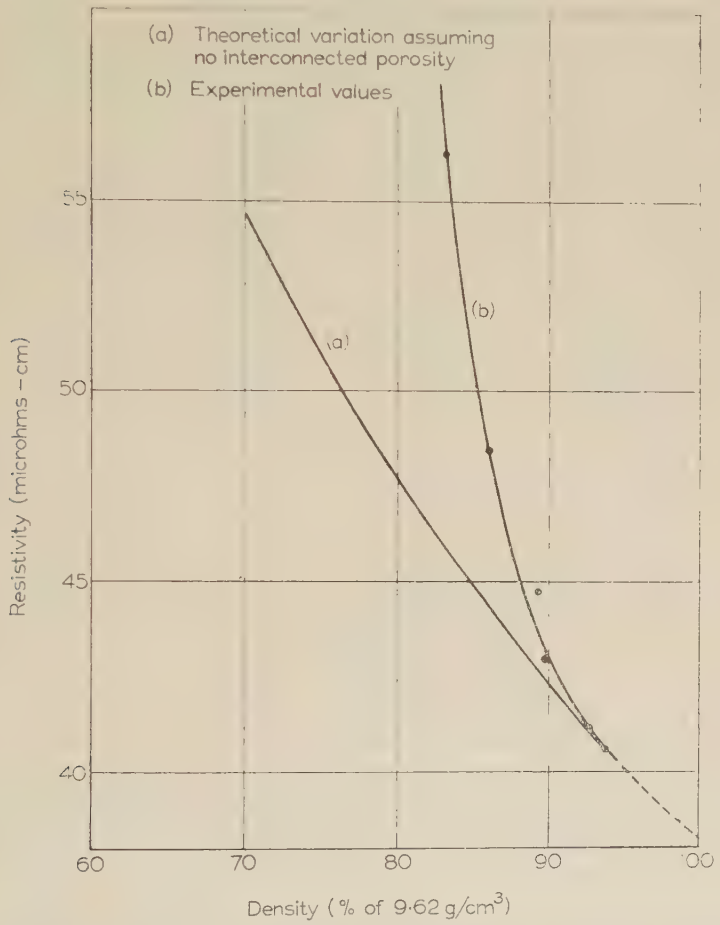

The variation of room temperature resistivity with density for sintered tungsten disilicide.

Chromium disilicide was exceptional in having a very much higher resistivity than any of the other silicides examined. It is interesting to note that the most stable titanium–silicon compound Ti_5Si_3 had a lower conductivity than either titanium or titanium disilicide.

All the compounds examined exhibited a positive temperature coefficient of resistivity and there was a general tendency for a large temperature coefficient to be associated with high room temperature

conductivity. Over the temperature range investigated the resistivity increased linearly with temperature, but the temperature coefficient for molybdenum disilicide of $6{\cdot}38 \times 10^{-3}$ was considerably greater than that of $1{\cdot}3 \times 10^{-3}$ calculated from data given by Glaser (1951) for the temperature range 22°c to 65°c.

Table 3. Electrical Properties

Compound	Resistivity at 20°c (microhms cm)		Temperature coefficient ($\times 10^3$)
	Present investigation	Published data	
$TiSi_2$	16·7	123[4] 19 [2]	4·63
$ZrSi_2$	106·2	161[4]	1·30
VSi_2	13·3	9·5[4]	3·51
$NbSi_2$	—	6·3[4]	—
$TaSi_2$	(38·0)	8·5[4]	3·32
$CrSi_2$	1420	>250[3]	2·93
$MoSi_2$	21·8	21·5[1]	6·38
WSi_2	38·2	33·4[4]	2·91
Ti_5Si_3	350	—	0·86
TiSi	39·3	—	4·13
ZrSi	49·4	—	3·52

[1] Glaser 1951.
[2] Glaser and Moskowitz 1953.
[3] Kieffer *et al.* 1953.
[4] Schwarzkopf and Kieffer 1953.

§ 5. Discussion

In order to facilitate discussion of the results, the data obtained in this investigation are summarized in table 4 ; the room temperature resistivity values for the silicides of vanadium, niobium and tantalum are those given by Gallistl (and reported by Schwarzkopf and Kieffer 1953). Table 4 also lists for comparison the room temperature resistivity, temperature coefficient of resistivity, and magnetic susceptibility of the transition metals. The variation of magnetic susceptibility with temperature exhibited by the transition metals is in all cases small, each element in a particular group showing the same type of temperature dependence : the sign of the temperature coefficient alternates from one group to the next, the paramagnetic susceptibility increasing with temperature for the Group IVa and VIa elements and decreasing with temperature for the Group Va elements (Kriessman and Callen 1954).

The following features of the experimental results may be put forward as evidence for the metallic character of the transition metal silicides.

Table 4. Magnetic and Electrical Properties of some Transition Metals and their Disilicides

Element	Disilicides				Metals		
	χ (e.m.u./g atom of metal $\times 10^6$)		Resistivity (microhms cm)	$\alpha \times 10^3$	χ (e.m.u./g atom) (Kriessman and Callen 1954)	Resistivity (microhms cm) (Smithells 1955)	$\alpha \times 10^3$ (Smithells 1955)
	Room Temp.	500°C					
Ti	+136	+119	16·7	4·6	153	55	3·5
Zr	− 96	−106	106·2	1·3	119	41	4·4
V	+168	+114	9·5[1]	3·5	255	26	2·8
Nb	− 30	—	6·3[1]	—	208	13·1	3·95
Ta	− 33	—	8·5[1]	3·3	152	13·5	3·8
Cr	+ 48	+ 43	1420	2·9	171	18·9	5·88
Mo	− 29·5	− 60	21·8	6·4	90	5·17	4·6
W	− 75	− 77	38·2	2·9	55	5·5	4·6

[1] Values obtained by Gallistl and reported by Schwarzkopf and Kieffer 1953.

1. The electrical conductivity of the silicides is high and in a number of cases is, in fact, greater than the conductivity of the uncombined metal.

2. The temperature coefficient of resistivity is in all cases positive and of the same order as for the transition metals.

3. The silicides of the metals of the first transition series exhibit paramagnetism, the magnitude of which may be associated with 'free' electrons and there is no reason to expect a marked difference in the nature of the silicides of the first and later periods.

4. The variation of the susceptibility with temperature is small. If the Weiss equation

$$\chi_m = C/(T-\theta) \qquad (1)$$

is assumed to hold then the results for titanium disilicide and vanadium disilicide, yield values for the Curie temperature (θ) of -3050°K and -720°K respectively, and Bohr magneton values, calculated from the Curie constant (C), of 1·9 and 1·2, respectively. The large negative values of θ would suggest that the susceptibility cannot be interpreted in terms of the classical theory of paramagnetism and that any ionic contribution must be small.

5. The magnetic susceptibility of the various compounds in the titanium–silicon and zirconium–silicon systems changes in an almost symmetrical manner with increasing silicon content.

It is apparent, therefore, that these compounds are essentially metallic and they should be considered either in terms of band theory or the more empirical resonating covalent bond approach.

When considering the experimental results in more detail it must be borne in mind that the disilicides do not all possess the same crystal structure (Robins and Jenkins 1955) and in each case the structure is unrelated to that of the original metal. An analysis of the various interatomic distances has shown that the metal–metal distances in the disilicides are so large that any significant amount of bonding between the metal atoms seems improbable and, therefore, the metallic behaviour of these materials must be associated with the character of the strong metal–silicon bonds (Robins and Jenkins 1955).

There is a general correspondence between the pattern of the magnetic susceptibility results for the disilicides and that of the transition metals, although all the transition metals exhibit paramagnetism, whereas many of the silicides are diamagnetic. For both the metals and the silicides, the tendency towards diamagnetism increases with increasing atomic number in a given group, although only the silicides in the first transition series are paramagnetic. The transition metals exhibit alternately relatively high and low values of room temperature susceptibility for the first five elements in a given transition series (Stoner 1954); the Group Va elements have high values and the elements of Group IVa and VIa relatively low values. This is also true for the disilicides. Vanadium disilicide exhibits the highest paramagnetism of the various compounds

examined and the disilicides having numerically the highest diamagnetism contain elements from Groups IVa and VIa.

The large paramagnetism of the transition metals is due to the high density of states at the top of the Fermi distribution, resulting from the interaction of incomplete d shells. Stoner (1954) has shown, however, that estimated values of the magnetic susceptibility of these elements calculated from the electronic contribution to the specific heat, assuming any additional interaction to be negligible, are considerably less than the observed values. There must be present in the transition metals, therefore, exhange interaction contributing to the observed paramagnetism. Although no direct comparison can be made between the magnetic properties of the silicides and those of the transition metals, it would seem probable that the increased metal metal separation in the silicides would reduce both the density of states at the top of the Fermi distribution and also the magnitude of any exchange forces between the incomplete d shells. However, the value of the susceptibility of titanium calculated from the electronic specific heat is given by Stoner (1954) as 48×10^{-6} e.m.u. g atom which is lower than the susceptibility after combination with silicon. In titanium disilicide, therefore, in addition to a high density of states there must also be a significant contribution to the paramagnetism from exchange forces. It would seem likely that, for vanadium disilicide also, the high paramagnetism can only be explained by assuming both a high density of electron states at the top of the Fermi distribution and a significant contribution from exchange forces. Since, as has been shown above, the metal–metal distances are such that direct interaction between incomplete d shells seems improbable, the high paramagnetism of titanium and vanadium disilicides lends support to Zener's hypothesis (1951 a, b, 1952) that the d shells are indirectly coupled through the conduction electrons.

The high paramagnetism of titanium disilicide and vanadium disilicide is associated with a high electrical conductivity which in both cases is considerably greater than the conductivity of the unalloyed metal. Since in the transition metals the high electrical resistivity is caused by the large scattering effect of the high density of states in the incomplete d bands, the low resistivity of these silicides would suggest that the scattering effect is reduced due to a decrease in the density of states. On Pauling's hypothesis this increase in conductivity may be associated with the role of the silicon atoms as centres of pivoting resonance thereby reducing the contribution from the scattering effect of the metal atoms.

The marked difference between both the electrical and magnetic properties of titanium disilicide and zirconium disilicide is most striking, particularly since the crystal structures are very similar. The high diamagnetism of zirconium disilicide would suggest that the zone structure is such that the effective electron mass of the electrons in the highest zone is small. This interpretation of slight overlap is supported by the high electrical resistivity of this compound which is an order of magnitude

greater than that of titanium disilicide. It is possibly of significance that the interatomic distances in zirconium disilicide are greater than in titanium disilicide.

The high electrical conductivity of niobium disilicide and tantalum disilicide would suggest the presence of 'free' electrons which would produce a weak paramagnetic effect and the observed weak diamagnetism is, no doubt, due to the diamagnetism of the completed shells and paired electrons being greater than the Pauli paramagnetism. The absence of a large paramagnetic effect as is present in vanadium disilicide shows that any exchange interaction must be small possibly due to the interatomic distances in the silicides increasing with increasing atomic weight of the metal.

The results obtained for the disilicides of the Group VIa metals present a number of interesting features. Chromium disilicide, unlike the disilicides of molybdenum and tungsten, has the same crystal structure as the Group Va disilicides. It exhibits a weak, almost temperature independent, paramagnetism which is coupled with a very high electrical resistivity. Molybdenum and tungsten disilicides, however, both have comparatively low resistivity values, and are diamagnetic. The numerical value of the diamagnetism of molybdenum disilicide increases considerably with temperature as also does the electrical resistivity. A theoretical analysis of the band structure of molybdenum and tungsten disilicides has been carried out by Schenk and Dehlinger (1956) who predict from their results that these compounds should possess diamagnetism. As for niobium disilicide and tantalum disilicide, the Pauli paramagnetism must be more than balanced by the underlying diamagnetism.

§ 6. Conclusions

The high electrical conductivity of the silicides studied in this investigation and their positive temperature coefficient of resistivity showed that these compounds are essentially metallic.

The disilicides of the elements in the first transition series are paramagnetic and for titanium disilicide and vanadium disilicide, the magnitude of the paramagnetism is comparable with that of the transition metals. This would suggest that for those compounds, in addition to a high density of states at the top of the Fermi distribution, there must also be a significant contribution to the paramagnetism from exchange forces in spite of the large metal–metal separation. The disilicides of the elements in the second and third transition series are all diamagnetic, zirconium having a particularly large diamagnetism coupled with a relatively high electrical resistivity. The variation of magnetic susceptibility with temperature over the range room temperature to 500°c was small, for the compounds studied.

It is apparent from the results that the study of this type of compound may be of importance as a method of obtaining additional information on the nature of the transition metals.

References

Bates, L. F., 1951, *Modern Magnetism* (Cambridge : University Press), p. 32.

Foëx, G., 1938, *J. Phys. Radium*, **9**, 37.

Glaser, F. W., 1951, *J. appl. Phys.*, **22**, 103.

Glaser, F. W., and Moskowitz, D., 1953, *Powder Metall. Bull.*, **6**, 178.

Hansen, M., Kessler, H. D., and McPherson, D. J., 1952, *Trans. Amer. Soc. Metals*, **44**, 518.

Kieffer, R., Benesovsky, F. and Machenschalk, R., 1954, *Z. Metallk.*, **45**, 493.

Kieffer, R., Benesovsky, F., and Schmid, H., 1956, *Z. Metallk.*, **47**, 247.

Kieffer, R., Benesovsky, F., and Schroth, H., 1953, *Z. Metallk.*, **44**, 437.

Kriessmann, C. J., and Callen, H. B., 1954, *Phys. Rev.*, **94**, 837.

Lundin, C. E., McPherson, D. J., and Hansen, M., 1953, *Trans. Amer. Soc. Metals*, **45**, 901.

Robins, D. A., 1956, *Light Metals*, **19**, 60.

Robins, D. A., and Jenkins, I., 1955, *Acta Met.*, **3**, 598 ; 1956, *Plansee. Proc.*, 1955 (London : Pergaman Press), p. 187.

Schenk, H., and Dehlinger, U., 1956, *Acta Met.*, **4**, 7.

Schwarzkopf, P., and Kieffer, R., 1953, *Refractory Hard Metals* (New York : Macmillan).

Selwood, P. W., 1956, *Magnetochemistry*, 2nd ed. (New York : Interscience Publishers), p. 78.

Smithells, C. J., 1955, *Metals Reference Book*, Vol. II (London : Butterworths), p. 673.

Stoner, E. C., 1954, *Acta Met.*, **2**, 259.

Zener, C., 1951 a, *Phys. Rev.*, **81**, 440 ; 1951 b, *Ibid.*, **82**, 403 ; 1952, *Ibid.*, **85**, 324.

$\pi^{\pm} \rightarrow \pi^0 + e^{\pm} + \nu + 8m_e c^2$?†

By E. Feenberg and H. Primakoff
Washington University, St. Louis, Missouri, U.S.A.

[Received December 16, 1957]

Abstract‡

The process $\pi^+ \rightarrow \pi^0 + e^+ + \nu$ has not yet been observed. Estimates of its branching ratio relative to $\pi^+ \rightarrow \mu^+ + \nu$ can be derived (1): from a phase space volume argument in conjunction with the available experimental information on π^+ and (assumed analogous) K^+ processes, and (2): from a calculation of the rate of the beta decay transition between the 'π^+' and 'π^0' states of a bound nucleon–antinucleon structure.

A possible experimental scheme for detection of $\pi^+ \rightarrow \pi^0 + e^+ + \nu$ in the presence of the overwhelmingly more frequent $\pi^+ \rightarrow \mu^+ + \nu$ is outlined.

§ 1. Introduction

The process $\pi^{\pm} \rightarrow \pi^0 + e^{\pm} + \nu$ has not up to now been observed. This process is interesting in the context of known beta decay modes of π and K particles. Empirical information on corresponding π and K beta decay modes is exhibited in the table. The experimental evidence on a, b, d, and a' is consistent with the interpretation of the neutral unobserved particles as a neutrino.

We first note that processes b and d are about equally probable: hence each of the two reactions

$$K^{\pm} \rightarrow \pi^0 + \mu^{\pm} + \nu \qquad . \ . \ . \ . \ . \ . \ . \ . \ (b)$$

$$K^{\pm} \rightarrow \pi^0 + e^{\pm} + \nu \qquad . \ . \ . \ . \ . \ . \ . \ . \ (d)$$

may have the same type of coupling and the same coupling constant. (The phase space volume factor in the transition probability for the muon mode b is only slightly smaller than for the electron mode d.)

Modes c and c' have not so far been observed. In particular the branching ratio of π^+ decay by c' is now known to be less than 10^{-5}§.

The direct analogue of b is b': however b' is energetically forbidden and can occur, if at all, only as a virtual process.

---

† Communicated by the Authors. This research was supported in part by the Office of Naval Research of the Navy Department and the Air Force Office of Scientific Research of the Air Research and Development Command.

‡ A preliminary version of this note has been given by Feenberg and Primakoff (1957). See also the discussion by Weinberg (1957).

§ The most recent experimental results on c' are due to Anderson (1957). The branching ratio of π^+ decay for the radiative form of c': $\pi^+ \rightarrow e^+ + \nu + \gamma$ is $(3 \pm 7) \times 10^{-6}$ (Cassels 1957).

These remarks suggest the possibility of a close analogy between each of the π decay processes $a', \ldots d'$ and the corresponding K processes $a, \ldots d$. We use this analogy to obtain an estimate of the rate of the as yet unobserved process d': $\pi^{\pm} \rightarrow \pi^0 + e^{\pm} + \nu$. The argument leading to our estimate is fairly arbitrary so that we consider that the result has

Information on Corresponding K^+ and π^+ Decay Processes†

Process		$Q/m_e c^2$	$\frac{p}{m_e c}$ (μ^+ or e^+)‡ or $\frac{p_{\max}}{m_e c}$ (μ^+ or e^+)‡	Partial decay rate
(a)	$K^+ \rightarrow \mu^+ + \nu$	759	462	5×10^7/sec
(b)	$K^+ \rightarrow \pi^0 + \mu^+ + \nu$	495	422	4×10^6/sec
(c)	$K^+ \rightarrow e^+ + \nu$	965	483	not observed
(d)	$K^+ \rightarrow \pi^0 + e^+ + \nu$	701	448	4×10^6/sec
(a')	$\pi^+ \rightarrow \mu^+ + \nu$	66	57	4×10^7/sec
(b')	$\pi^+ \rightarrow \pi^0 + \mu^+ + \nu$	—	—	energetically forbidden
(c')	$\pi^+ \rightarrow e^+ + \nu$	272	136	not observed
(d')	$\pi^+ \rightarrow \pi^0 + e^+ + \nu$	8	9	?

† Shapiro (1956). ‡ Computed.

value only as a guide in the search for reaction d'. Clearly, observation of this reaction would be of considerable fundamental interest, but even experimental evidence that its branching ratio is appreciably smaller than our estimate would be helpful in the development of a coherent theory.

§ 2. Estimate of Branching Ratio

Let now M_x denote the effective transition matrix element for process $x (x = a, b, \ldots, d')$, ρ_x the associated number of final states per unit final energy range, i.e. the associated 'phase space volume', and R_x the corresponding partial decay rate. Then, with p_ν, p_μ, p_e representing the neutrino, muon, and electron momenta, we have:

$$R_x = \frac{2\pi}{\hbar} |M_x|^2 \rho_x \quad \ldots \ldots \quad (1)$$

$$\rho_x \equiv (\text{const})\, p_\nu^2 \Big/ \left(\frac{\partial E_{\text{fin}}}{\partial p_\nu}\right); \; x = a, c, a', c' \quad \ldots \ldots \quad (2)$$

$$\rho_x = (\text{const}) \int_0^{(p_l)_{\max}} dp_l p_l^2 \int_0^{\pi} d\theta_{l\nu} \sin\theta_{l\nu} \left\{ p_\nu^2 \Big/ \left(\frac{\partial E_{\text{fin}}}{\partial p_\nu}\right)\right\}; \; p_l = p_\mu \text{ or } p_e; \quad x = b, d, d'. \quad (3)$$

Thus, writing m_{K^+}, m_{π^+}, m_{π^0}, m_μ for the kayon, charged pion, neutral pion, and muon masses, and with use of the table, we have the processes a' and a:

$$\frac{R_{a'}}{R_a} = \frac{|M_{a'}|^2}{|M_a|^2}\frac{\rho_{a'}}{\rho_a} = \frac{|M_{a'}|^2}{|M_a|^2}\left\{\frac{[(m_{\pi^+}{}^2 - m_\mu{}^2)/m_{\pi^+}]^2[1+(m_\mu/m_{\pi^+})^2]}{[(m_{K^+}{}^2 - m_\mu{}^2)/m_{K^+}]^2[1+(m_\mu/m_{K^+})^2]}\right\} \quad (4)$$

$$\simeq \frac{4\times 10^7}{5\times 10^7}.$$

Consequently,

$$\left|\frac{M_{a'}}{M_a}\right| \simeq 6. \quad (5)$$

The corresponding calculation for the processes d' and d yields:

$$\frac{R_{d'}}{R_d} = \frac{|M_{d'}|^2}{|M_d|^2}\frac{\rho_{d'}}{\rho_d} \simeq \frac{|M_{d'}|^2}{|M_d|^2}\left\{\frac{(m_{\pi^+} - m_{\pi^0})^5/15}{(m_{K^+})^5/270}\right\} = \frac{|M_{d'}|^2}{|M_d|^2}(1{\cdot}2\times 10^{-9})$$

$$\simeq \frac{R_{d'}}{4\times 10^6}. \quad (6)$$

We now assume that the ratio of corresponding π and K effective transition matrix elements is independent of the decay channel, i.e. using also eqn. (5):

$$\left|\frac{M_{d'}}{M_d}\right| \simeq \left|\frac{M_{c'}}{M_c}\right| \simeq \left|\frac{M_{b'}}{M_b}\right| \simeq \left|\frac{M_{a'}}{M_a}\right| \simeq 6. \quad (7)$$

Eqns. (6), (7) and the table then give:

$$R_{d'} \simeq 0{\cdot}2/\text{sec}; \quad R_{d'}/R_{a'} \simeq 5\times 10^{-9} \quad (8)$$

so that, according to eqn. (8), approximately 5 out of every 10^9 charged pions are expected to decay via $\pi^\pm \to \pi^0 + e^\pm + \nu$.

An alternative estimate of $R_{d'}$ is obtained by interpreting process d' as a beta decay transition analogous to the beta decay of a bound system of nucleons and characterized by the same Fermi and Gamow–Teller types of interaction with the same coupling constants. Introducing the corresponding effective 'nuclear' matrix element $N_{d'}$ ($N_{d'}$ proportional to $M_{d'}$) and the f function of beta decay theory, and interpreting the transition as superallowed within a $T=1$ isobaric spin multiplet, we obtain:

$$|N_{d'}|^2 f(9m_e c^2)\frac{\ln 2}{R_{d'}} \simeq 5000 \quad (9)$$

with

$$|N_{d'}|^2 = |(T=1, T_3=0\,|\,T_1 - iT_2\,|\,T=1, T_3=1)|^2 = 2.$$

Also $f(9m_e c^2) \simeq 1700$. Equation (9) then yields

$$R_{d'} \simeq 0{\cdot}5/\text{sec}; \quad R_{d'}/R_{a'} \simeq 10^{-8} \quad (10)$$

quite close to the estimate of eqn. (8).

We may now attempt to place the above calculation on a possibly more secure basis by using a bound nucleon–antinucleon (Fermi–Yang) model

for the pion. In the two particle approximation of this model the π^+, π^0 wavefunctions are†:

$$\pi^+ \equiv [p(1)n^{\text{anti}}(2)]_{T=1,\, T_3=1}\psi_{J=0^-}(\mathbf{x}_1, \mathbf{x}_2, s_1, s_2) \quad . \quad . \quad . \quad . \quad . \quad . \quad . \quad (11)$$

$$\pi^0 \equiv 2^{-1/2}([p(1)p^{\text{anti}}(2)] - [n(1)n^{\text{anti}}(2)])_{T=1,\, T_3=0}\psi_{J=0^-}(\mathbf{x}_1, \mathbf{x}_2, s_1, s_2).$$

In this context the transition occurs via one or the other of the two processes

$$(p)_{\text{bound}} \rightarrow (n)_{\text{bound}} + e^+ + \nu \quad . \quad . \quad . \quad . \quad . \quad (12)$$

$$(n^{\text{anti}})_{\text{bound}} \rightarrow (p^{\text{anti}})_{\text{bound}} + e^+ + \nu.$$

These processes may contribute in-phase or 180°-out-of-phase to the $\pi^+ \rightarrow \pi^0$ transition amplitude depending on the type of coupling between the nucleon–antinucleon and lepton fields‡. In the in-phase case—provided that the coupling is such that the $\pi^+ \rightarrow \pi^0$ transition is not otherwise 'forbidden'‡—the estimate of eqns. (9) and (10) for the branching ratio $R_{d'}/R_{a'}$ is valid, but in the out-of-phase case the computed $R_{d'}/R_{a'}$ will be much smaller than 10^{-8}.

§ 3. Possible Experimental Scheme

We shall now discuss briefly a possible arrangement for detecting the process $\pi^+ \rightarrow \pi^0 + e^- + \nu$ in the presence of an overwhelming background from the process $\pi^- \rightarrow \mu^+ + \nu$. A beam of positive pions is stopped in an absorber. The process $\pi^+ \rightarrow \pi^0 + e^+ + \nu$ then gives rise to two pairs of photons from the reactions:

$$\pi^0 \rightarrow \gamma_{132m_e c^2} + \gamma_{132m_e c^2}$$

$$e^+ + e^- \rightarrow \gamma_{m_e c^2} + \gamma_{m_e c^2}$$

with the $m_e c^2$ photons from the e^+, e^- annihilation delayed relative to the $132m_e c^2$ photons from the π^0 decay by less than 10^{-9} sec. On the other hand, the process $\pi^+ \rightarrow \mu^+ + \nu$ is followed by

$$\mu^+ \rightarrow e^+ + \nu + \nu; \quad e^+ + e^- \rightarrow \gamma_{m_e c^2} + \gamma_{m_e c^2}$$

with any accompanying high energy ($\leqslant 104m_e c^2$) photons arising only from external or internal bremsstrahlung of the decay e^+ from the μ^+.

---

† In eqn. (11), the $\psi_{J=0^-}(\mathbf{x}_1, \mathbf{x}_2, s_1, s_2)$ are the angular momentum, parity eigenfunction factors in the π^+, π^0 wavefunctions, $\mathbf{x}_1$, $\mathbf{x}_2$, s_1, s_2 being the space and spin coordinates of the nucleon and antinucleon. For the forms of the nucleon–antinucleon $\mathbf{T}^2$, T_3 eigenfunction factors in eqn. (11), see for example, Malenka and Primakoff (1957).

‡ Thus, with the now current beta decay interaction Hamiltonian (which includes any existing non-invariant terms for charge conjugation, space reflection and time inversion in the lepton factor) the two processes (12) contribute in-phase for polar vector or tensor coupling and contribute 180°-out-of-phase for scalar, axial vector or pseudoscalar coupling. However, since the $\pi^+ \rightarrow \pi^0$ transformation involves a $J=0^- \rightarrow J=0^-$ transition, the tensor coupling contribution for each of the two processes (12) and so for their (in-phase) combination is 'second forbidden' and hence is much smaller (for given magnitudes of the coupling constants) than the 'allowed' polar vector coupling contribution.

With reference to fig. 1, the approximately oppositely directed $132m_e c^2$ photons can be detected in coincidence. Energy discrimination in the counting circuit can be used to decrease the number of background coincidences arising from, e.g. the above mentioned high energy bremsstrahlung photons accompanying the $\mu^+ \to e^+$ decay. If the production

Fig. 1

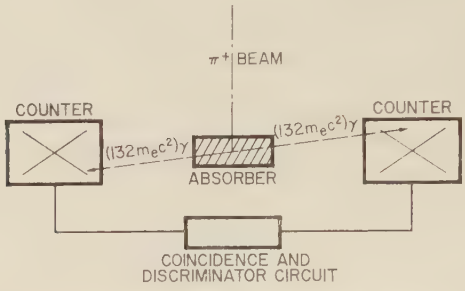

Block diagram of apparatus for detection of neutral pions produced in absorber.

of neutral pions in the absorber is demonstrated by this arrangement, an energy discriminating delayed fourfold coincidence circuit for the detection of the two $132m_e c^2$ photons and the two $m_e c^2$ photons —see fig. 2—can be used to determine whether the neutral pions are indeed produced by the process $\pi^+ \to \pi^0 + e^+ + \nu$ or whether they arise from a charge exchange reaction in the absorber:

$$\pi^+ + (Z, A) \to \pi^0 + (Z+1, A)\dagger.$$

Another possible source of background will arise from the conceivably existing radiative $\pi^+ \to e^+$ decay followed by (external) bremsstrahlung of the e^+ and its ultimate annihilation:

$$\pi^+ \to e^+ + \nu + \gamma; \quad e^+ \to (e^+)' + \gamma'; \quad (e^+)' + e^- \to \gamma_{m_e c^2} + \gamma_{m_e c^2}.$$

† The delay involves the time interval Δt between the instant of passage of the π^+ through a monitor counter in front of the absorber and the instant of detection of the (energy discriminated) fourfold coincidence. The number of delayed fourfold coincidences arising from the process sought: $\pi^+ \to \pi^0 + e^+ + \nu$, etc., will vary with Δt as $\exp(-\Delta t/\tau)$ ($\tau = \pi^+$ lifetime $= 2{\cdot}5 + 10^{-8}$ sec). On the other hand, the number of delayed fourfold coincidences associated with neutral pions which are not decay products of incident positive pions, will exhibit a dependence on Δt quite different from $\exp(-\Delta t/\tau)$. Thus, the delayed fourfold coincidence circuit should discriminate effectively against the $132m_e c^2$ photons from any promptly produced charge exchange neutral pions—there will also be effective discrimination, on a time basis as well as on the previously noted energy basis, against the relatively late appearing high energy bremsstrahlung photons associated with

$$\pi^+ \to \mu^+ + \nu; \quad \mu^+ \to e^+ + \nu + \nu + \gamma; \quad e^+ \to (e^+)' + \gamma'.$$

Finally, the number of prompt charge exchange neutral pions can be kept to a minimum by use of incident positive pions of low energy falling on a high Z absorber while the probability of external bremsstrahlung by the decay e^+ from the μ^+ can be decreased by making the absorber as thin as feasible.

In general however, the two photons γ, γ' will not be emitted mutually antiparallel and will not each have an energy close to $132 m_e c^2$. On the other hand, one may search for $\pi^- \rightarrow e^+ + \nu + \gamma$; $e^+ + e^- \rightarrow \gamma_{m_e c^2} + \gamma_{m_e c^2}$ with an appropriate modification of the apparatus of fig. 2.

Fig. 2

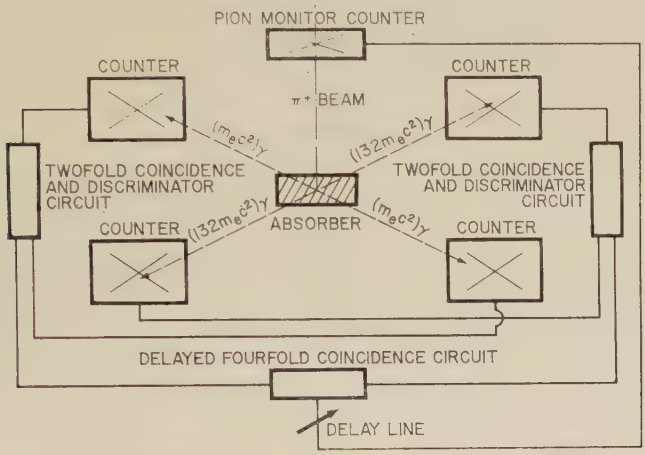

Block diagram of apparatus for detection of delayed four-fold coincidences from $\pi^+ \rightarrow \pi^0 + e^+ + \nu$.

References

Anderson, H., 1957, *Proceedings of Seventh Annual Rochester Conference* (New York: Interscience), p. ix+32 (reported by Telegdi).

Cassels, J. M., 1957, *Proceedings of Seventh Annual Rochester Conference* (New York: Interscience), p. ix+27.

Feenberg, E., and Primakoff, H., 1957, *Bull. Amer. phys. Soc.*, **2**, 39.

Malenka, B. J., and Primakoff, H., 1957, *Phys. Rev.*, **105**, 338.

Shapiro, A. M., 1956, *Rev. mod. Phys.*, **28**, 164.

Weinberg, S., 1957, *Phys. Rev.*, **106**, 1301.

The Decoration of Dislocations in Crystals of Silver Chloride with Gold†

By J. T. Bartlett and J. W. Mitchell
H. H. Wills Physical Laboratory, University of Bristol

[Received February 10, 1958]

Abstract

A new method is described for the decoration of dislocations in crystals of silver chloride. The crystals are sensitized by heating them, together with gold wire and cupric chloride, in an atmosphere of chlorine in sealed tubes at a temperature of 350°c. They are then strained, exposed to light with a wavelength which is not strongly absorbed by silver chloride, and heated for a few minutes at a temperature between 140 and 160°c. Nuclei which are formed along the dislocation lines during exposure increase to visible size during the subsequent thermal treatment.

The formation of systems of prismatic dislocations around precipitates in silver chloride crystals is described and it is suggested that the observations may be relevant to the interpretation of precipitation hardening in certain alloys.

§ 1. Introduction

Dislocations in crystals of silver chloride are made visible by exposing them to light, which causes silver to separate along the dislocation lines (Hedges and Mitchell 1953, Clark and Mitchell 1956, Mitchell 1957 c), and by etching the surfaces with a 3N solution of sodium thiosulphate (Jones and Mitchell 1957). Both the dislocations which remain after annealing and those which are introduced by plastic deformation are rendered visible by these two methods. The decoration of the dislocations in crystals of silver chloride and of silver bromide with photolytic silver does not depend on the introduction of foreign substances or upon thermal treatment of elevated temperatures. The configurations of dislocations which are observed in annealed and plastically deformed silver halide crystals are therefore likely to have been modified to a smaller extent by the decoration process than those in alkali halide crystals. The decoration of the dislocations is practically continuous and discrete particles of photolytic silver cannot usually be resolved.

The only real disadvantage of this method is that it has never been possible to decorate dislocations at a depth greater than 30 μ below the surface, even when the crystals have been sensitized by the deposition of thin films of silver or of silver sulphide upon their surfaces before exposure to light. The aim of the present work has therefore been to discover

† Communicated by the Authors.

a method for making dislocations visible throughout the thickness (usually 200 to 400 μ) of the thin silver chloride sheets which we use for much of our work on plastic deformation. Our object has been achieved with the development of a new method for decorating dislocations with platelets of gold.

§ 2. Experimental Methods and Observations

During their work on the photographic sensitivity of mixed crystals of aurous and silver halides, Clark and Mitchell (1956) observed that thin platelets of gold, with surfaces parallel to {111} planes, separated spontaneously when the crystals were stored at room temperature after exposure to visible light. We hoped that it might be possible to find conditions in which the gold would separate upon nuclei formed along dislocation lines.

The first stage in the present work was therefore the preparation of crystals of silver chloride with a range of concentrations of aurous chloride extending from 10^{-1} to 10^{-3} mol%. 10^{-1} mol% of anhydrous auric chloride, which decomposes to give aurous chloride, was added to the molten silver chloride and globules and thin sheet crystals were made as described by Clark and Mitchell. Hydrogen chloride was used as a protective gas throughout the operations. After separation from the glass plates, the crystals were cut into sections and annealed in a sealed tube in an atmosphere of chlorine at a pressure of 200 to 300 mm Hg at 350°C for 6 to 12 hours.

The crystals were then exposed to the light from a 250 watt mercury vapour lamp which was filtered through a thin sheet of silver chloride for a number of the experiments to remove strongly absorbed wavelengths. After exposure, the crystals were heated in air on thin microscope cover slips resting on the surface of a heated steel bar.

When annealed crystals containing 10^{-1} mol% of aurous chloride were exposed and either kept at room temperature for several weeks or heated for a few minutes to temperatures between 140 and 160°C, they darkened in the exposed areas due to the separation of platelets of gold throughout their thicknesses; no precipitation occurred in unexposed areas. Individual dislocations could not be recognized in these crystals but the density of gold platelets was appreciably greater on grain boundaries and sub-boundaries than elsewhere. All the earlier observations of Clark and Mitchell were confirmed.

Globules with progressively lower concentrations of aurous chloride were next prepared by diluting the 0·1 mol% material with silver chloride. Thin sheet crystals were made, cut into sections, annealed in chlorine and exposed and heated as just described. The density of gold platelets decreased with the concentration of aurous chloride and clusters in which platelets formed on all the {111} planes passing through a nucleus did not appear. The individual platelets of gold in a crystal containing 0·05 mol% aurous

chloride are shown in fig. 1, Pl. 9. This crystal was exposed at a distance of 25 cm from the mercury vapour lamp for 6 minutes without the production of any microscopically visible internal change. It darkened rapidly in the exposed area due to the formation of platelets of gold when it was heated for 1 minute at 140°C. These randomly distributed platelets, which have surfaces parallel to the {111} planes, are not formed when crystals with lower concentrations of aurous chloride are treated in the same way.

Crystals with 0·005 mol% aurous chloride were then prepared and annealed in chlorine at 350°C for 8 hours. This produces recrystallized areas around the cut edges in which very few dislocations remain and polygonizes the central areas of the crystal sections. Gold platelets did not separate near the surfaces when these crystals were heated after exposure. Precipitates were, however, formed within the crystals at distances greater than 50 μ from the surfaces and there was some decoration of dislocations. No precipitation was observed in crystals containing 0·001 mol% aurous chloride.

It seemed likely that some of the aurous chloride had diffused out when these crystals were annealed in chlorine at 350°C. We therefore heated a further batch of the crystals in a sealed tube with chlorine, together with a piece of gold wire, for 8 hours at the same pressure and temperature. The final concentration of aurous chloride after this treatment is not known but new and interesting phenomena were observed when the crystals were examined with the microscope after having been exposed for 1 to 5 minutes and heated for 5 to 15 minutes at temperatures between 140 and 160°C. After they had been annealed in chlorine, together with the gold wire, the crystals which had an initial concentration of 0·005 mol% aurous chloride contained microscopically visible internal particles, with a diameter of less than 1 μ, distributed throughout the thickness. When they were exposed for 5 minutes and heated for 15 minutes at 160°C, arrays of regularly spaced smaller precipitates appeared along the twelve ⟨110⟩ directions passing through the centres of the 1 μ particles. This new precipitation phenomenon which is illustrated in fig. 2, Pl. 9 will be discussed in § 3.

The dislocations of internal sub-boundaries in crystals which had an initial concentration of 0·001 mol% aurous chloride were decorated when they were exposed for 1 minute and heated for 6 minutes at 160°C. A decorated hexagonal network in the interior of a crystal is shown in fig. 3, Pl. 10; the high density of randomly distributed particles should be noted. The smaller secondary precipitates which are shown in fig. 2, Pl. 9 did not appear in these specimens. All the thin sheet crystals which were prepared from globules of silver chloride containing aurous chloride had a high density of particles after annealing and, although it proved possible to decorate the dislocations of the tilt and twist sub-boundaries, it was evident that such crystals would not be suitable for work on the behaviour of dislocations during plastic deformation.

Thin sheet crystals of very pure silver chloride were next prepared and annealed at 350°C for 8 hours in chlorine at a pressure of 200 to 300 mm Hg. They were then further annealed at 350°C for 2 hours in chlorine at a pressure of 30 mm Hg together with a piece of thin gold wire. This is essentially the technique which is described in the footnote to the paper by Barber *et al.* (1957). Gold does not separate spontaneously along dislocation lines when the silver chloride crystals are cooled down to room temperature and their properties differ in this respect from those of sodium chloride crystals. The dislocations remaining after the two annealing treatments were clearly decorated when the crystals were exposed for 5 minutes and then heated for 10 minutes at 140°C. During the heat treatment microscopically visible particles of gold never separated in unexposed areas. The quality of the decoration is shown in fig. 4, Pl. 10. The discrete nature of the gold particles is illustrated by the dislocations in the plane of the photomicrograph near the upper left hand corner of the field. All the phenomena which have already been described for crystals of pure silver chloride and silver bromide in which the dislocations have been decorated with photolytic silver have now been observed in crystals of silver chloride in which the dislocations have been decorated with gold, with the advantage that the decoration extends throughout the crystals instead of being confined to the surface region.

In an attempt to improve the decoration, the pressure of chlorine in the tube during the second anneal was next reduced from 30 first to 15 and then to 5 mm Hg at 350°C. Gold did not separate in any form when the crystals from these batches were heated to 160°C after exposure. Luckey (1953, 1955) had previously observed that silver bromide was sensitized for the liberation of bromine during exposure to light at temperatures around 100°C by the incorporation of cupric bromide. We therefore decided to investigate the effect of the introduction of cupric chloride on the separation of gold during the thermal treatment of exposed crystals of aurous and silver chlorides. By evaporating the required volume of a dilute solution to dryness, we deposited 5×10^{-5} gm of cupric chloride on the internal surface of the glass tube which was to be used for the second anneal. Previously annealed crystals were then heated for 4 hours at 400°C in chlorine at a pressure of 15 mm Hg, together with a piece of gold wire. They were exposed for 5 minutes and heated for 5 minutes at 160°C. The dislocations were clearly decorated throughout the thickness of the crystals by the separation of discrete particles of gold during the thermal treatment after exposure and there was a negligible background density of randomly distributed gold particles. The most interesting observations were made in the recrystallized areas around the edges, which have a very low initial density of dislocations. Dislocations introduced into these areas by plastic deformation after the diffusion of aurous and cupric chlorides into them are shown in figs. 5 and 6, Pl. 11. The decorating particles are larger and more widely separated than the particles of photolytic silver which form in dislocations near the surface during exposure, but optimum conditions may not yet have been established.

An example of the detail which can be observed is given in fig. 7, Pl. 10. In this specimen, the boundary separating the recrystallized area from the remainder of the crystal moved discontinuously during the first anneal in chlorine at 400°c and left behind a number of microscopic cavities on the surfaces corresponding with the arrest positions; some cupric chloride may have separated in these during the second anneal. The cusps formed when dislocation lines gliding in the recrystallized area were held back by these imperfections are clearly shown in the photomicrograph.

We have established that there is continuity between the sub-surface decoration of dislocations with photolytic silver and the internal decoration of dislocations with gold by exposing crystals to the full radiation from the mercury vapour lamp and then heating them to 150°c for 5 to 10 minutes. The dislocations of many tilt boundaries could then be followed downwards from the surface where the decoration was produced mainly by photolytic silver to the interior where the decoration was due to the separation of discrete particles of gold.

§ 3. Discussion

In this section, we shall discuss the mechanism of the decoration of dislocations in crystals of silver chloride with gold and the significance of the precipitation phenomenon which is illustrated in fig. 2, Pl. 9. After it had been established that dislocations could be decorated as shown in fig. 3, Pl. 10, our work was concentrated on eliminating the randomly distributed particles which were observed both after the diffusion of the aurous chloride into the crystals and after the subsequent exposure and heating. The density of these particles was reduced (1) when the specimens were recrystallized by annealing them for a long period in chlorine before the aurous chloride was diffused into them; (2) when the concentration of aurous chloride was decreased to the smallest value at which gold would precipitate and (3) when cupric chloride was diffused into the specimens at the same time as the aurous chloride.

The Schottky defects which are present in significant concentrations in crystals of silver chloride at temperatures near the melting point aggregate when the crystals are cooled to lower temperatures, with the formation of a random distribution of small dislocation loops and internal cavities. During the processes of decoration, gold nuclei are formed at these imperfections and grow into visible particles. Our observations show that the dislocation loops and cavities are usually eliminated when the areas around the cut edges of the thin crystals recrystallize during the course of a long anneal in chlorine at 350°c. Nuclei cannot then be formed in regions of the crystals free from dislocations unless vacant chloride ion lattice sites are available which can condense together with vacant silver ion lattice sites to produce internal cavities in which gold atoms can aggregate. At temperatures below 200°c, the concentration of vacant chloride ion lattice sites in silver chloride crystals is negligible; nuclei can therefore only be formed in dislocations and other crystal imperfections where space for the separation of gold atoms is already available.

Nuclei consisting of groups of silver and gold atoms are formed on the surfaces of internal cavities and along dislocation lines when the crystals are exposed to light with a wavelength beyond the absorption edge of silver chloride. The nuclei adsorb gold or silver ions and become positively charged when they exceed a certain critical size, the compensating negative charge being provided by vacant silver ion lattice sites (see Mitchell 1957 b for a discussion of these properties). When the crystals are heated to a temperature between 140 and 160°c, electrons are transferred from the full band (with the production of positive holes) to the low lying acceptor levels in the forbidden band associated with the positively charged nuclei. Their positive charge is restored by the adsorption of further cations and further vacant silver ion lattice sites are created. The positive holes and vacant silver ion lattice sites diffuse to the surface of the crystals where chlorine escapes. Copper chloride has a number of functions during sensitization, exposure and heat treatment. One of them appears to be that of increasing the efficiency with which chlorine molecules are liberated from the surfaces of the crystals during heat treatment at temperatures between 140 and 160°c. The cupric ions introduce acceptor levels in the forbidden band near the top of the full band to which electrons may be transferred by thermal activation with the creation of positive holes. A fraction of these positive holes, which are repelled by the positively charged gold nuclei, are trapped at the surface in the form of Cl_2^- -molecular ions. These then trap positive holes, liberated when electrons are transferred from the full band to the positively charged gold nuclei, and form chlorine molecules which escape (see Mitchell 1957 a, b for a detailed discussion of this process).

We turn now to the discussion of the significance of the fine precipitates which are shown in fig. 2, Pl. 9. It may be recalled that the central particles of the systems of precipitates were visible in the microscope when the crystals were removed from the tubes in which they had been heated with the gold wire in chlorine. The systems of regularly spaced fine precipitates extending along the ⟨110⟩ directions passing through the central particles first became visible after the crystals had been exposed to light at room temperature and heated to 160°c for 6 minutes.

Although the phenomena are on a smaller scale, there is a close analogy between these systems of fine precipitates and the systems of positive prismatic dislocations which form during cooling around glass spheres imbedded in silver chloride crystals and which have recently been described by Jones and Mitchell (1958). As a working hypothesis, which is consistent with all the observations which have been made, we propose that the central gold particle grows initially at the annealing temperature by a mechanism which depends on the diffusion of Schottky defects to its interface with the silver halide. Precipitation continues during cooling in the furnace but a stage is reached at which the rate of arrival of pairs of lattice vacancies at the interface is insufficient to make space available for the gold atoms separating there. The gold nuclei then increase in

size until the decrease in free energy accompanying the separation of gold atoms is balanced by the increase in free energy due to elastic deformation of the surrounding silver halide crystal. A radially symmetric compressive stress field is thus established around the gold particles which is of the same nature as the stress field around the glass spheres in the experiments of Jones and Mitchell. We suggest that this stress field is relaxed by the mechanism which they have described, namely, the formation of positive prismatic dislocations which glide away over the surfaces of twelve slip cylinders with ⟨110⟩ directions radiating from the central particle as axes. The decoration of these prismatic dislocations with gold during the subsequent exposure of the crystals at room temperature and their heating to 140 to 160°c gives rise to the systems of regularly spaced fine precipitates which are shown in fig. 2, Pl. 9. The structure of these precipitates cannot be resolved with the optical microscope.

Harvey and Mitchell (1958) have recently concluded that the systems of prismatic dislocations, formed during the cooling of crystals of sodium chloride containing aurous chloride, which have been described by Barber *et al.* (1957) and are illustrated in fig. 3 of their paper have the same origin. They have demonstrated that the dark central particles such as that shown in fig. 3 (*b*) of the paper are specks of gold. The positive character of the prismatic dislocations has been established by observing their inclinations in known stress fields (see fig. 7 in the paper by Jones and Mitchell 1958).

Parasnis and Mitchell (1958) have also observed systems of prismatic dislocations extending along all twelve ⟨110⟩ directions radiating from particles of photolytic silver formed during the exposure of crystals of silver chloride containing 0·1 mol% of cuprous chloride. From these observations they have concluded that space for the separation of silver is made available at the interface between a silver particle and the silver halide by the formation of positive prismatic dislocations which glide away from the interface along slip cylinders with the twelve ⟨110⟩ directions as axes.

There can be little doubt that these groups of independent observations provide evidence for a previously unrecognized phenomenon in precipitation reactions in the solid state. When the rate of growth of a precipitate particle exceeds the rate at which the material of the matrix can be removed from the interface by the condensation of vacant lattice sites, a compressive stress field is established which is relaxed by the formation of positive prismatic dislocations, which glide away from the interface. We believe that this may prove to be of importance for the understanding of precipitation hardening because we have observed that the systems of closely spaced prismatic dislocations which result from mutual interactions when there is a high density of precipitate particles present an effective barrier to the glide motion of dislocations. The observations show that the strain associated with a particle of a precipitate can be transmitted to distances many time the radius of the particle by the mutual repulsion of the prismatic dislocations. It seems that the possibility that some features of the observations of Preston and Guinier on the diffraction of

x-rays during the early stages of precipitation hardening in certain alloys could be interpreted in terms of diffraction by arrays of positive prismatic dislocations or by precipitates nucleated upon them should be considered.

§ 4. Summary and Conclusion

Dislocations may be decorated by the precipitation of gold throughout the volumes of sheet crystals of silver chloride with thicknesses between 200 and 400 μ. The essential features of the new experimental method are as follows. After separation from the glass plates, the crystals are cut into sections and annealed for 8 to 12 hours at a temperature between 350 and 400°c in chlorine at a pressure between 200 and 300 mm Hg During this anneal the areas around the cut edges of the crystals recrystallize and the remaining central area polygonizes. The crystals are then heated in a sealed tube in chlorine at a pressure of 15 to 30 mm Hg and at a temperature of 350°c together with a piece of gold wire and 5×10^{-5} gm of cupric chloride for 4 hours. They may then be strained at room temperature. They are exposed to light from a mercury vapour lamp to produce nuclei along the dislocation lines and heated at 140 to 160°c for 1 to 15 minutes to increase the size of these nuclei until they are visible in the microscope.

A new class of precipitation phenomena is described and discussed. Four independent groups of observations show that the compressive stress field around an inclusion or a growing precipitate particle may be relaxed by the generation of positive prismatic dislocations which glide away from the interface between the particle and the matrix along slip cylinders with the twelve ⟨110⟩ directions passing through the centre of the particle as axes.

Acknowledgment

This work has been carried out during the tenure of a D.S.I.R. Research Studentship by J. T. Bartlett. It has also been supported by a grant from Kodak Ltd., which is gratefully acknowledged.

References

Barber, D. J., Harvey, K. B., and Mitchell, J. W., 1957, *Phil. Mag.*, **2**, 704.
Clark, P. V. McD., and Mitchell, J. W., 1956, *J. photogr. Sci.*, **4**, 1.
Harvey, K. B., and Mitchell, J. W., 1958, *Phil. Mag.* (to be published).
Hedges, J. M., and Mitchell, J. W., 1953, *Phil. Mag.*, **44**, 223.
Jones, D. A., and Mitchell, J. W., 1957, *Phil Mag.*, **2**, 1047 ; 1958, *Ibid.*, **3**, 1.
Luckey, G. W., 1953, *J. phys. Chem.*, **57**, 791 ; 1955, *J. chem. Phys.*, **23**, 882.
Mitchell, J. W., 1957 a, *J. photogr. Sci.*, **5**, 49 ; 1957 b, *Rep. Progr. Phys.* (London : Physical Society), **20**, 433 ; 1957 c, *Dislocations and Mechanical Properties of Crystals* (New York : John Wiley), p. 69.
Parasnis, A. S., and Mitchell, J. W., 1958, *Phil. Mag.* (to be published).

The Thermal and Electrical Resistivity of Bismuth and Antimony at Low Temperatures†

By G. K. White and S. B. Woods
Division of Pure Physics, National Research Council, Ottawa, Canada

[Received December 18, 1957]

Abstract

Measurements are reported of the electrical resistivity of pure polycrystalline specimens of bismuth and antimony over the range 2 to 300°K and of the thermal conductivity up to 150°K. Some measurements in a magnetic field have also been made which allow separation of the thermal conductivity into electronic and lattice components. Below 50°K, it appears that the heat conductivity of bismuth is nearly all due to lattice waves; free electrons seem to contribute little to the conduction or to the scattering. In antimony, however, the lattice conductivity is smaller than might be expected at low temperatures suggesting significant scattering by free electrons. The electronic term, λ_e, in antimony is remarkably similar in its temperature dependence to that in a monovalent metal.

The electrical resistivity of both elements varies as about $T^{2\cdot75}$ for $T \leqslant \theta/10$. For bismuth the approximate proportionality of resistivity with temperature observed at normal temperatures extends to rather lower temperatures than is usual in a metal.

§ 1. Introduction

Bismuth and antimony are both elements with five valence electrons which are capable of filling a so-called Jones‡ zone exactly, but due to the smallness of the energy discontinuity at the zone boundary, a small number of electrons overlaps into the next band, leaving holes in the almost filled band (for example as discussed by Wilson 1953, pp. 92, 169 or Mott and Jones 1936, p. 302). Measurements of such properties as magneto-resistance, Hall effect, diamagnetism, anomalous skin effect and de Haas-van Alphen effect enable estimates of the number of free electrons per atom to be made. Unfortunately these measurements (see Wilson 1953, p. 230 and Shoenberg 1952) do not all indicate similar values for this number, estimates for bismuth varying from as low as about 10^{-5} to perhaps 10^{-2} electron per atom. It appears that much experimental evidence suggests about 10^{-3} electron per atom in bismuth and perhaps 10^{-2} in antimony. At ordinary temperatures the electrical resistivities of these elements are only an order of magnitude higher than for many good metallic conductors: it thus seems that the electron

† Communicated by the Authors.

‡ The use of the name Jones zone for certain energy zones which are not strictly zones in the sense defined by Brillouin, has been recently discussed in detail in a review by Reitz (1955).

mean free paths in these semi-metals must be very much longer than in normal metals. Sondheimer (1952) has pointed out that a long mean free path should be a consequence of the small number of free electrons in the almost empty conduction band ; these electrons may only interact with lattice vibrations of long wavelength and such interactions will be relatively unimportant except at low temperatures. This might also be expected to lead to a linear variation of electrical resistance with temperature down to rather low temperatures, e.g. to about 10°K for bismuth.

The small number of available free electrons may be affected appreciably by the presence of certain impurities, but fortunately antimony and bismuth are now readily available in a state of high purity and may be purified in the laboratory by zone melting techniques. Their electrical and thermal conductivities at low temperatures have been investigated experimentally for many years but most determinations have been concerned with the effect of magnetic fields and crystal anisotropy on these properties in rather restricted temperature intervals.

We have measured the electrical resistance of our samples over the relatively wide temperature range extending from 2°K to 300°K and the thermal resistance from 2°K to about 150°K. Polycrystalline specimens of high purity and fairly large grain size were used. As well as establishing the temperature dependence of the electrical resistance and of the thermal conductivity, we have tried to separate the latter into electronic and lattice components.

References to previous measurements of thermal conductivity by Gehlhoff, Rausch, Rosenberg, Eucken, Reddemann, Rodine, de Haas, Gruneisen, Capel and others may be found in the compilation of Powell and Blanpied (1954) and the review by Klemens (1956). Data on electrical resistance is discussed by Wilson (1953), and in the recent review by Gerritsen (1956).

A preliminary report of part of this work was presented (White and Woods 1957 a) at the Fifth International Conference on Low Temperature Physics and Chemistry (Madison, Wisconsin, U.S.A.) and thermal conductivity results for two of the less pure bismuth samples (Bi 1 and Bi 2) were reported in an earlier paper (White and Woods 1955).

§ 2. Experimental Method

The cryostat and method of measurement have already been described (White and Woods 1955), helium-filled gas thermometers being used for temperature measurement and a galvanometer-amplifier for observing the electrical resistance.

Table 1 lists the following characteristic parameters of the specimens used in this work : approximate diameter, D ; residual electrical resistivity, ρ_0 ; electrical resistivity at room temperature, ρ_{295} ; and the value assumed for the Debye characteristic temperature, θ_D (see Keesom and Pearlman 1956).

The specimens were rods about 6 cm long and connections were made by soldering to them—soft solder for antimony and Woods' metal for the bismuth specimens—except Bi 2 which was cast with copper potential leads in it. Their purity and general history are as follows

Table 1. Data for Specimens

	D (mm)	ρ_0 ($\mu\,\Omega$ cm)	ρ_{295} ($\mu\,\Omega$ cm)	θ (°K)
Bi 1	2	104	136	120
Bi 2	3	5·9	120	120
Bi 3	~3·5	$2{\cdot}0_7$	118 †	120
Bi 4	5×5×2·5	1·70	118 †	120
Bi 5	6×6	2·4	118 †	120
Sb 1	4·3×2·5	0·057	47·7	200
Sb 2 } Sb 2a }	5	0·054	41·3	200

† Because of the irregular dimensions of these specimens, this room temperature resistivity value was assumed (cf. Gerritsen 1956); the geometrical form factor of the specimen(s) was then calculated using this value together with the measured resistance of the specimen: i.e. $l/A = R/\rho$.

Bi 1 was cast and cooled quickly in a glass tube; it contained columnar crystals penetrating to the centre of the rod, 16 to 18 crystals being exposed on the circular section. Its original purity of 99·97% when supplied by Mining and Chemical Products (London) was no doubt affected by having been previously handled and cast before this final casting.

Bi 2 was cast in a brass former from granular bismuth of about 99·99% purity supplied by the General Chemical Division of Allied Chemical and Dye Corporation. Due to rather slower cooling, the columnar crystals appeared larger, there being about six crystals per circular section.

Bi 3 was zone-refined by Mr. Gaston Fischer of this laboratory starting with 99·999% bismuth from Varlacoid Chemical Company of New York. It was subsequently annealed in a larger tube for several days at a temperature just below the melting point. The crystals were about 1 cm long and had the lateral dimensions of the rod; these dimensions were somewhat irregular as it melted temporarily during annealing.

Bi 4 and Bi 5 were both cut from a zone-refined bar prepared by Mr. Fischer from Varlacoid bismuth. Bi 4 had a triangular cross section of sides 5, 5 and 2·5 mm and contained about three large crystals. Bi 5, of square section, consisted of crystals 1 to 2 cm long and from 2 to 4 mm wide, slightly inclined to the axis of the rod.

Sb 1 was sawn from a lump of 'extra high purity' grade antimony of the Bradley Mining Company (San Francisco); it was not annealed.

After measurements were made it was annealed but unfortunately broke before being remounted in the cryostat. However a second antimony specimen, Sb 2, was made by Mr. Fischer in this laboratory. It was prepared by zone-refining high-purity grade antimony from Bradley Mining Company and later annealing the specimen at about 600°C for a week. The crystals in Sb 2 varied from about 2 to 5 mm in width. The low electrical resistance ratio, $\rho_0/\rho_{295}=1{\cdot}3\times10^{-3}$, is a confirmation of the high chemical purity of these specimens.

Sb 2a is identical with Sb 2, having been merely remounted in the cryostat for the magneto-resistance studies.

§ 3. Results

3.1. *Thermal Conductivity*

Our results for bismuth, shown in fig. 1 together with values from Shalyt† (1944), indicate that at temperatures below 3°K the heat conductivity, λ, increases with temperature as T^n where $n=2{\cdot}7\pm0{\cdot}2$; at higher temperatures, from about 10 to 50°K, λ falls approximately inversely as the temperature. As we shall discuss below, this behaviour seems quite typical of a pure crystalline solid in which lattice waves conduct practically all the heat unimpeded by the presence of any free electrons. Only at the highest temperatures is there a departure suggesting that electrons may be making a contribution to the conductivity. The change in thermal conductivity with magnetic field tends to confirm this. At liquid oxygen temperatures a field of about 10^4 oe reduces the heat conductivity by 15 to 20% but has no noticeable effect at liquid helium temperatures, a behaviour observed also by Shalyt. The increase in electrical resistance due to a field of 10^4 oe is about 30-fold at 90°K, so that a field of this magnitude should be quite sufficient to reduce the electronic thermal conductivity, λ_e, to insignificance compared with the lattice conductivity, λ_g, provided that the Lorenz ratio , $L_e=\rho\lambda_e/T$, is not seriously affected by the field.

The results of our measurements on antimony are shown in fig. 2 together with those of Rosenberg (1955) and of Gehlhoff and Neumeier (1913). These latter results from 80 to 300°K seem representative of much of the earlier work in this temperature range (see for example curves in the compilation of Powell and Blanpied 1954). In contrast to the behaviour in bismuth, our antimony results show that at very low temperatures $\lambda\simeq aT$; at least for Sb 2, the constant, a, has a value close to $L_0/\rho_0=2{\cdot}45\times10^{-8}/\rho_0$ $W\ \mathrm{cm}^{-1}\ \mathrm{deg}^{-2}$, which indicates that the electronic component, λ_0 is dominant. For the unannealed rod Sb 1, the measured Lorenz ratio or the proportionality constant, a, is about 10% lower than the theoretical value. It seems most unlikely that this measurement is correct because it is well established for pure metals at very low temperatures that $\rho\lambda_e/T=L_0\simeq2{\cdot}45\times10^{-8}\,W\,\Omega\ \mathrm{deg}^{-2}$ and the presence of a lattice

† Obtained on a Hilger single crystal of high purity, which had a cross section of about 0·1 cm²: the residual resistance ratio ρ_0/ρ_{295} was about 20×10^{-3}, not very different from that for our samples 3, 4 and 5.

component only serves to increase the apparent value of L_0. As specimen Sb 1 was subsequently annealed and broken, another determination cannot be made but it is probable that the measurement of ρ_0 was in error. The specimen was short and of fairly large cross section so that an electrical resistance of about one micro-ohm had to be measured; for this it was necessary to use the galvanometer amplifier at its maximum sensitivity and a small calibration error may have occurred.

Fig. 1

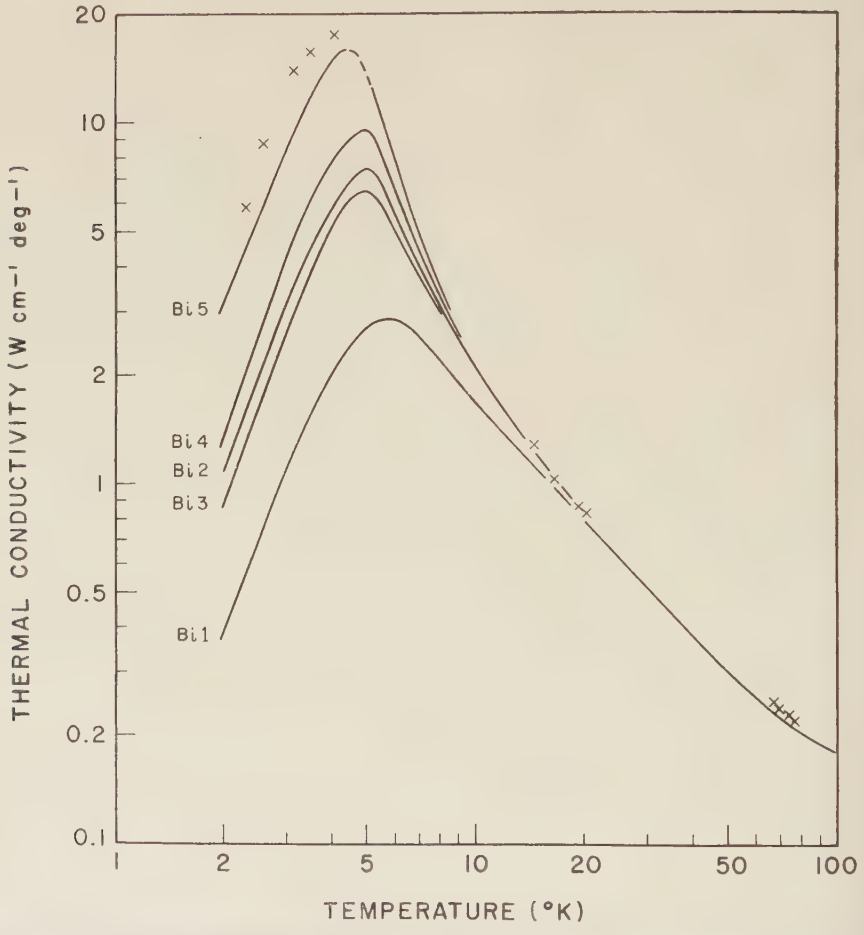

Thermal conductivity of bismuth: experimental points are omitted for clarity but curves have been drawn through the points (cf. fig. 2). X represents values obtained by Shalyt (1944).

As in the case of bismuth, the small effective number of free electrons in antimony is associated with a large magnetic field dependence of the electron transport properties. Since the electron component of thermal conductivity will be affected by magnetic fields while the lattice conductivity should be field insensitive, this provides a method of separating

the terms, λ_e and λ_g. The increase in the electrical resistance of Sb 2a at temperatures of 4·2°K, 11·4°K, 17·2°K, 24°K and 34·2°K when a field of 5 koe was applied was 200-fold, 300-fold, 60-fold, 11-fold and 3-fold respectively. At temperatures below 20°K, a field of 2 or 3 koe decreased the thermal conductivity considerably but larger fields, up to 10^4 oe, had no measurably greater effect so we have assumed that this 'saturation' value of λ, called λ_H, is the lattice conductivity, λ_g (in fig. 7).

Fig. 2

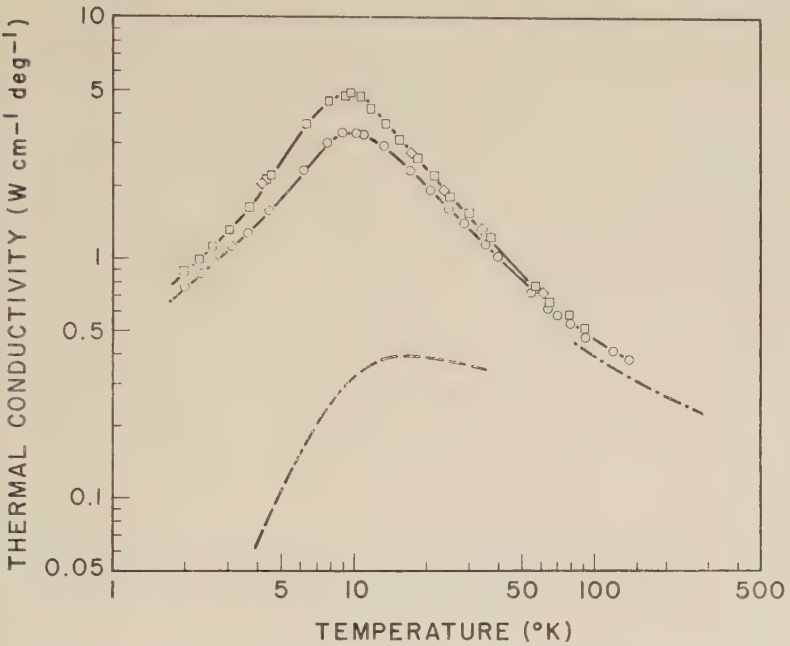

Thermal conductivity of antimony.

○ Sb 1 ——— Rosenberg (1955)

□ Sb 2 — · — Gehlhoff and Neumeier (1913)

◇ Sb 2a

At temperatures between 20 and 40°K a field of about 10^4 oe was used to obtain a value for $\lambda_g=\lambda_H$. At 58 and 91°K the method used by Rausch (1947, see also review by Olsen and Rosenberg 1953) has been followed to obtain the lattice conductivity. As shown in fig. 3, λ and ρ at a given temperature are measured in a series of magnetic fields; then it is assumed that the Lorenz ratio, $L_e=\rho\lambda_e/T$, is field-independent at that temperature and if

$$\lambda=\lambda_e+\lambda_g$$
$$=L_eT/\rho+\lambda_g$$

a graph of λ *vs* T/ρ should yield a straight line with intercept λ_g at $T/\rho=0$. Our values for λ_g as well as for the total thermal conductivity, $\lambda=\lambda_{H=0}$, and for $\lambda_e=\lambda-\lambda_g$ of specimen Sb 2a are shown in fig. 7.

3.2. *Electrical Resistivity*

The rather impure specimen, Bi 1, had a very high residual resistance (see table 1 and White and Woods 1955), showed strong departure from Matthiessen's additivity rule and a marked minimum in the electrical resistance at about 18°K. As discussed, for example, by Wilson (1953, p. 228), the band structure of bismuth is very sensitive to the presence of any impurities which increase or decrease the number of effective electrons or holes and these effects may be temperature sensitive giving a form of semiconductor behaviour in some cases.

Fig. 3

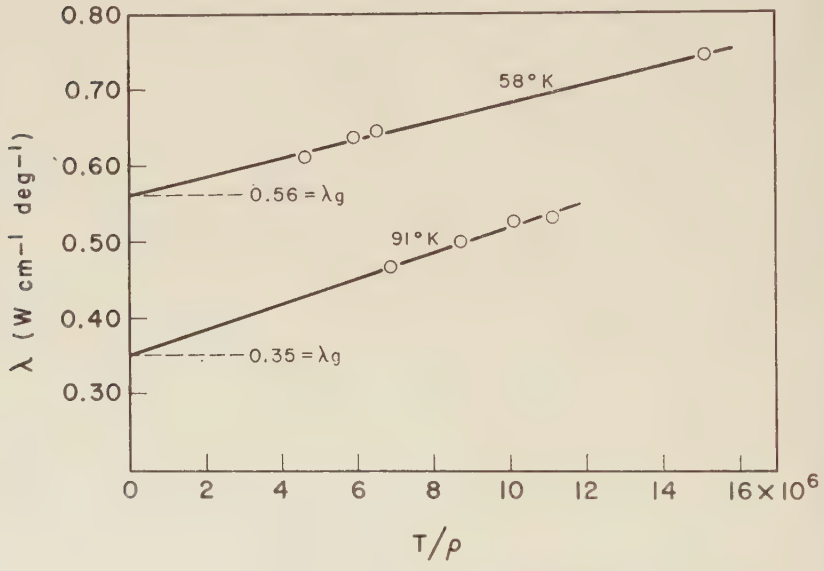

A graph of thermal conductivity, λ, as a function of T/ρ in magnetic fields of 0 to 14 koe.

For the other bismuth and antimony specimens the electrical resistivity ρ, appears sensibly constant below about 3°K, and values of the residual resistivity, ρ_0, assumed to be due to scattering by static imperfections, are given in table 1. Because of an uncertainty of a few per cent in their geometry the resistivities of specimens Bi 3, 4, and 5 have been normalized to give a room temperature value, $\rho_{295} = 118 \times 10^{-6}\ \Omega$ cm (see review by Gerritsen 1956). The values for the ideal resistivity, $\rho_i = \rho - \rho_0$, due to scattering by thermal vibrations, agree fairly well for different bismuth specimens, the maximum deviation being a few per cent between Bi 2 and Bi 3 in the region from 30 to about 150°K. This presumably reflects the different average crystal orientations in these two specimens. Mean values of ρ_i are given in table 2 and these accord quite well with mean values of the reduced electrical resistance, R/R_{273}, for different single crystals of bismuth investigated by Schubnikow and de Haas (1930).

Table 2. Smoothed Values of 'Ideal' Electrical Resistivity in micro-ohm cm

$T°K$	Bi	Sb	$T°K$	Bi	Sb
θ	44 (120°K)	25·9 (200°K)	50	19	3·2
295	116	41·3	40	15	$2·1_5$
273	105	37·6	30	10	1·2
250	96	34·0	20	5·8	$0·4_2$
200	74	25·9	15	3·4	$0·1_8$
150	55	17·9	10	$1·3_5$	$0·06_3$
100	37	10·0	5	$0·2_0$	~0·009
75	29	6·5			

Fig. 4

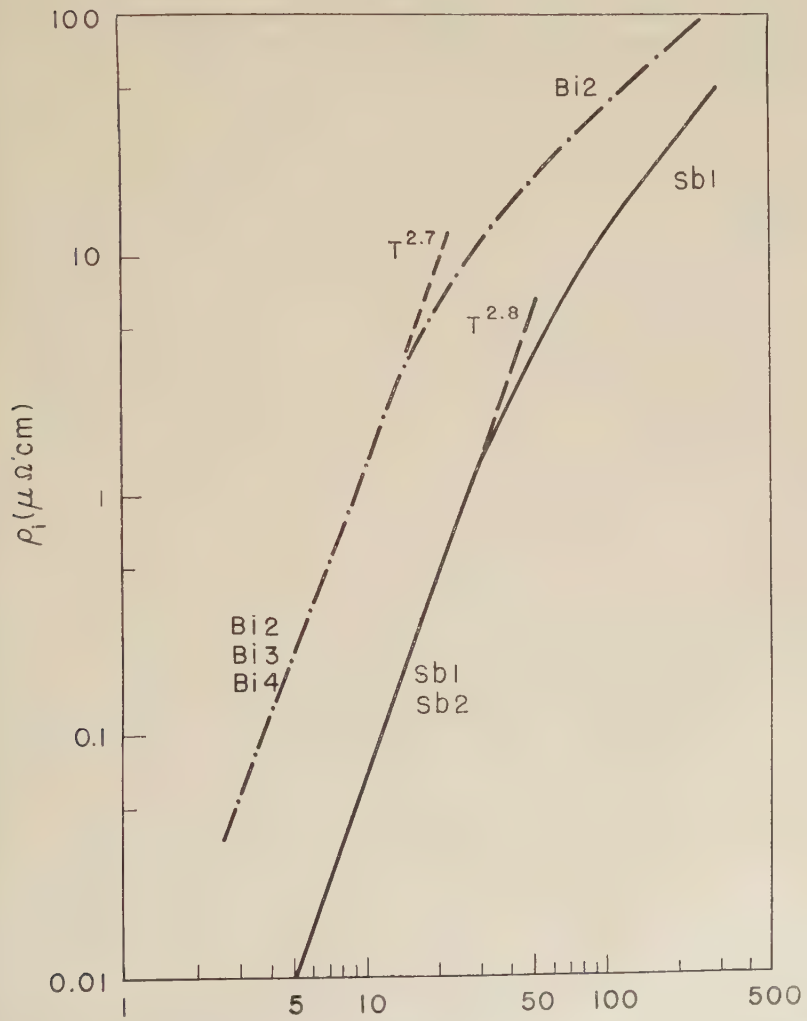

Ideal electrical resistivity, $\rho_i = \rho - \rho_0$, of bismuth and antimony. Experimental points are omitted for clarity.

The form of ρ_i as a function of temperature is illustrated in fig. 4. The rather high value shown in table 1 for the room temperature resistivity of Sb 1 (cf. review by Gerritsen 1956) may be due to uncertainty in the shape of the specimen, so the values quoted for antimony in table 2 were taken from the results for both Sb 1 and Sb 2, the Sb 1 values having first been normalized to give $\rho_{295}=41{\cdot}3\times10^{-6}\ \Omega$ cm.

§ 4. Discussion

4.1. *Thermal Resistivity*

General. Experiment and theory on the thermal conductivity of solids have not always been in good agreement during the past few years, but patterns of behaviour have emerged for crystalline insulators and for pure metallic elements which are fairly consistent. Reviews by Olsen and Rosenberg (1953), Berman (1953) and Klemens (1956) discuss the situation in detail. Briefly, we may expect the following behaviour:

(*a*) For pure metallic elements

$$\lambda=\lambda_e+\lambda_g \text{ where } \lambda_e\gg\lambda_g$$

and

$$1/\lambda\equiv W\simeq W_e=W_0+W_i$$

where the impurity resistivity, $W_0=\rho_0/L_0T$. Also for $T\geqslant\theta_D$, the ideal resistivity, W_i, becomes sensibly constant and equal to W_∞, the total thermal resistivity at high temperatures. It has been shown (MacDonald *et al.* 1956, White and Woods 1957 b, White 1956) that to a good approximation the ratio W_i/W_∞ is well represented by the function:

$$W_i/W_\infty=2(T/\theta_D)^2\int_0^{\theta/T}\frac{x^3dx}{(e^x-1)(1-e^{-x})}$$

for most metallic elements. For $T\ll\theta_D$ this expression reduces to $W_i/W_\infty\simeq14{\cdot}4\,(T/\theta_D)^2$.

(*b*) For crystalline insulators $\lambda=\lambda_g$ and

$$1/\lambda_g\equiv W_g=W_B+W_D+W_P+W_U,$$

where the resistivity components arise from scattering of the lattice waves by the crystal boundaries (W_B), by dislocations (W_D), by point imperfections (W_P), and from an anharmonic interaction between the lattice waves (W_U). For a crystal with no imperfections the thermal conductivity is limited at low temperatures by boundary scattering and $\lambda\propto T^3$ while at high temperatures, where the lattice wave interactions become important, $\lambda=1/W_U\propto1/T$.

In metals a term, W_E, must be added to W_B and W_U to account for scattering of the lattice waves by free electrons. This term, which varies as T^{-2} at low temperatures, is large enough to reduce λ_g to insignificance in comparison with λ_e if the metal is a pure element. In semiconductors and perhaps in semimetals (e.g. Bi, Sb), where the number of free electrons is small, this term is much less important.

Bismuth. Results on bismuth (fig. 1) suggest that boundary scattering of lattice waves is the main resistive mechanism at liquid helium

temperatures. The formula obtained by Casimir (1938) may be reduced to $\lambda_B \simeq 2{\cdot}3DT^3$† for the case of bismuth where D is the effective diameter of the crystals. A comparison of effective diameters calculated from

Fig. 5

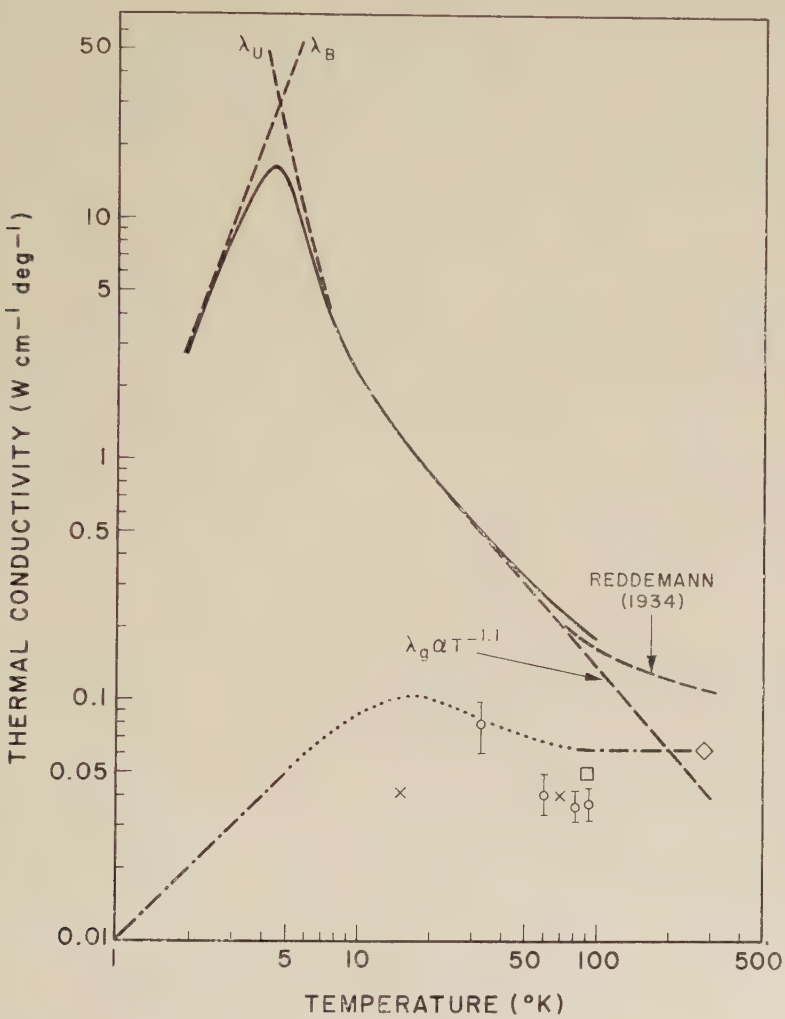

Thermal conductivity of bismuth

——— λ (Total) Bi 5

— · — λ_e calc. from $\lambda_e = L_0 T/\rho$

..... λ_e interpolated assuming $W_i = 2(T/\theta)^2 J_3(\theta/T)$

× λ_e deduced from Shalyt (1944)

⊙ λ_e from Bi 5

□ λ_e from Grüneisen *et al.* (1950)

◇ λ_e from Reddemann (1934)

† The numerical factor in this equation is slightly different from that quoted previously (White and Woods 1955) as we are now using the value $\theta_D = 120°$K suggested by recent specific heat data.

λ (at 2° K) using this equation and the actual grain dimensions is given below. Agreement is far from perfect but in view of the uncertainty of the average grain dimension, it seems to confirm that grain boundaries are the main cause of scattering of lattice waves at low temperatures.

Table 3. Crystal Dimensions for Bismuth Samples.

Sample	Bi 1	Bi 2	Bi 3	Bi 4	Bi 5	Shalyt
D (grain size) cm	~0·02	~0·1	0·1–0·3	0·2	0·2–0·4	~0·3
D (from $\lambda_{2°K}$) cm	0·02	0·06	0·05	0·07	$0·1_7$	0·2

In fig. 5, the total observed conductivity of Bi 5 is plotted again, together with the probable form of the lattice conductivity, λ_g, and possible form of the electron contribution, λ_e. The extrapolation of λ_g has been made with the aid of our measurements on Bi 5 in a magnetic field which gave $\lambda_g \simeq 0·16$ (91° K), 0·18 (78° K), 0·23 (60° K) and also those given by Reddemann (1934).

Thus we find that $\lambda_g \propto T^{-1·1}$ which is not very different from the expected $1/T$ variation due to anharmonic coupling. If, in fact we approximate the data in fig. 5 by

$$\lambda_g \simeq 14/T \quad W\,\mathrm{cm}^{-1}\,\mathrm{deg}^{-1},$$

we may then compare this expression with theoretical ones deduced by Leibfried and Schlömann (1954), Dugdale and MacDonald (1955) and Kontorova (1957). These expressions, strictly speaking only valid for simple isotropic solids, are based on extensions of a linear chain model and are essentially equivalent to one another. If we assume the average interatomic distance in bismuth to be about 3·3 Å and the Debye temperature to be 120° K, then the Leibfried–Schlömann formula reduces to $\lambda_U = 55/\gamma^2 T$. It seems misleading to give even an approximate value for the Grüneisen parameter, γ, but we may note that if $\gamma = 2$ (as it does approximately for many cubic solids) then remarkably good agreement with the experimental expression is obtained (cf. our remarks on Ge and Si (White and Woods 1956) and Te (Fischer *et al.* 1957).

Between 10 and 5° K the conductivity rises much more rapidly with decreasing temperature than a $1/T$ law would predict. Peierls (see for example reviews by Berman 1953 and Klemens 1956) has ascribed such a rise in the lattice conductivity to a rapidly decreasing probability of the Umklapp processes which gives rise to the thermal resistivity, W_U. If we assume that W_P, W_D and W_E are all zero so that $1/\lambda = W_B + W_U$, we may extrapolate $\lambda_U \equiv 1/W_U$, as shown in fig. 5, down to about 4° K with some confidence. If we now write $\lambda \simeq C'vl/3$ where C' is the specific heat per unit volume and v is the velocity of the phonons, (say $1·5 \times 10^5$ cm/sec in Bi), then the mean free paths, l (shown in fig. 6)

can be calculated from λ or from λ_U. The apparent exponential dependence of $l(\lambda_U)$ upon θ/T (fig. 6) which gives some confirmation of Peierls' theory of Umklapp processes, has also been observed for solid helium, diamond and sapphire (see review by Berman 1953).

Fig. 6

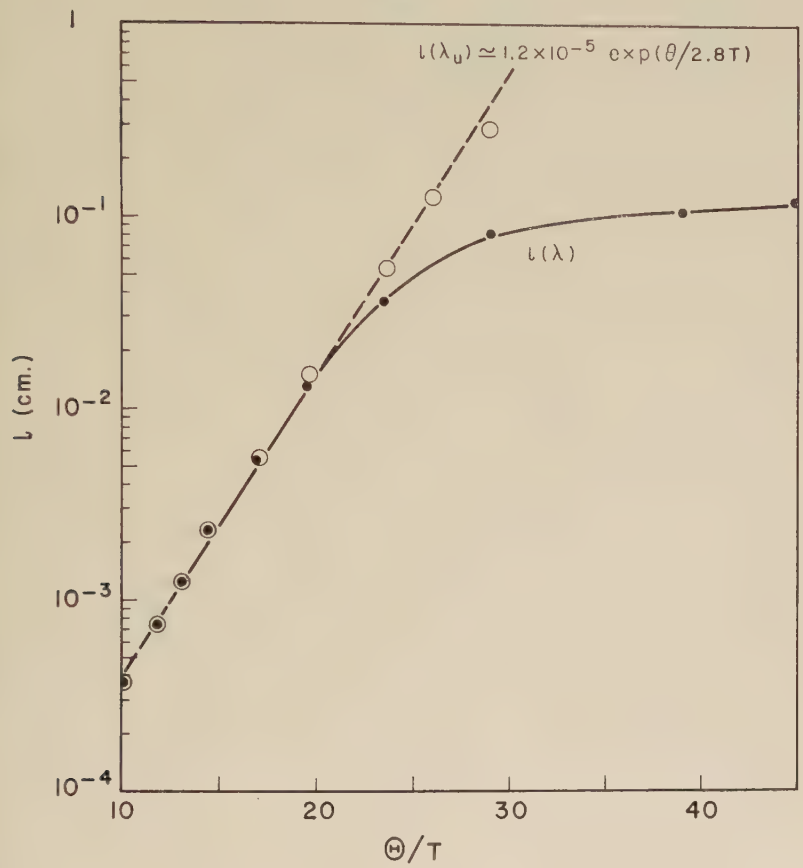

Mean free paths, l, of phonons calculated for Bi 5.
Points ○ are calculated from λ_U and points ● from λ.

Turning to the electronic component of heat conductivity, λ_e, in bismuth, we find less precise information. The low and high temperature extremities of the λ_e curve drawn in fig. 5, have been calculated from values of the residual electrical resistivity and the high temperature values of the ideal electrical resistivity (where $\rho_i \propto T$) assuming

$$\rho\lambda_e/T = 2{\cdot}45\times10^{-8}\ W\Omega\ \text{deg}^{-2}.$$

It does seem that this Wiedemann–Franz–Lorenz law should be valid in regions where scattering is elastic, that is where the effective mean free

paths of the electrons are the same for both electrical and thermal transport processes. However at intermediate temperatures the behaviour of the ideal thermal resistivity, $W_i = 1/\lambda_i$, for a semimetal like bismuth, seems unpredictable at present. In bismuth below 20°K the heat conducted by the electrons is so small compared to that conducted by the lattice that direct experimental measurement using a magnetic field only gives a crude value. Above 50°K we might expect values of $\lambda_e = \lambda - \lambda_g$ to be more reliable and they fall rather below the values calculated from the *W–F L* law except at room temperature where Reddemann's measurements give values of about 0·06 *W* cm $^{-1}$ deg $^{-1}$.

Fig. 7

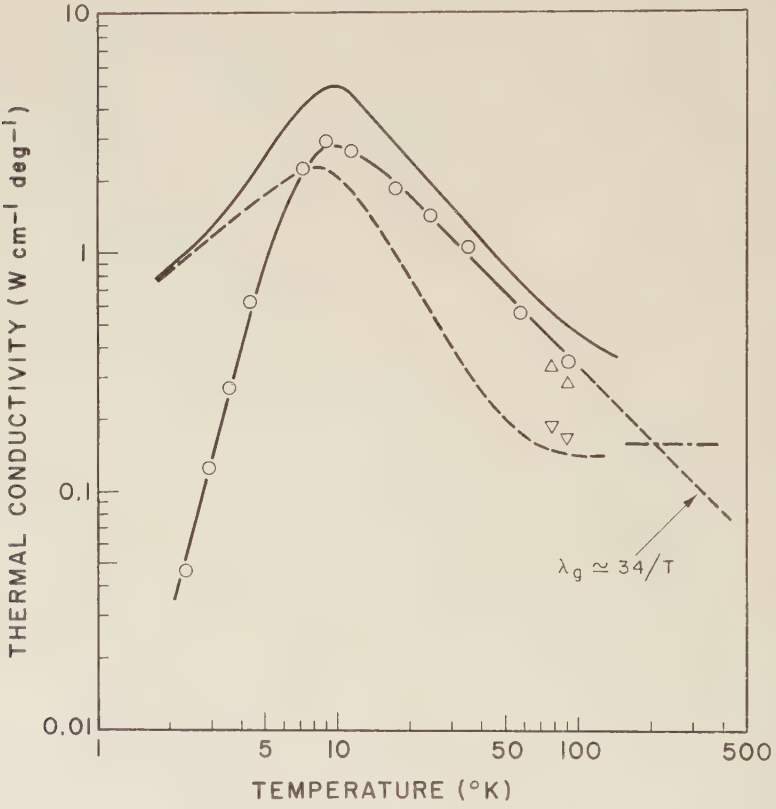

Thermal conductivity of antimony

——— λ (Sb 2, Sb 2a) — · — $\lambda_e = L_0 T/\rho$
— ○ — λ_g (Sb 2a) △ λ_g, ▽ λ_e : Rausch (1947)
— — — $\lambda_e = \lambda - \lambda_g$ (Sb 2a)

Antimony. The measured total heat conductivity, λ, for Sb 2 (and Sb 2a) is shown in fig. 7 together with values of the lattice conductivity measured with the aid of a magnetic field, and a dashed curve representing $\lambda - \lambda_g = \lambda_e$. The isolated experimental values for λ_e and λ_g at about

80 and 90 K are those obtained by Rausch (1947) for a single crystal measured in two directions in a plane perpendicular to the axis of trigonal symmetry. These two directions, which Rausch denoted by S_{II} and S_I and which gave similar results, are the [110] and [112] directions in the smallest rhombohedral unit cell.

Consider first the lattice conductivity, λ_g, for antimony: At high temperatures $\lambda_g \simeq 34\,T$ W cm^{-1} deg^{-1} which we may compare with a value of $\lambda_U \simeq 110/\gamma^2 T$ deduced from the Leibfried-Schlömann formula using 3·1 Å for the average interatomic distance. We may again remark that a value of γ in the vicinity of 2 gives close agreement but this should not be taken too seriously. The accepted values of cubic expansion coefficient, α, and compressibility, χ, for polycrystalline material lead to $\gamma = \alpha/\chi C \simeq 1$ (cf. Mott and Jones 1936, p. 318) for both antimony and bismuth. However Barron (1956) has pointed out that for anisotropic materials in which $\bar{\gamma}$ is small the variation in γ among individual normal modes can not be neglected; even in the limit where $\bar{\gamma}=0$ there will, in general, still be cubic terms in the crystal potential causing coupling of the normal modes of vibration.

At lower temperatures the behaviour of the lattice conductivity is rather more puzzling. In this very pure, well annealed sample, Sb 2, λ_g varies as about $T^{3\cdot6}$ below 4 K and the maximum mean free path of the lattice waves appears to be about 0·1 mm which is very much less than the grain size. Although we have no measurements in a magnetic field for the specimen Sb 1, comparison of Sb 1 and Sb 2 indicates that the lattice conductivity is much smaller still for Sb 1 at liquid helium temperatures but a high density of dislocations (e.g. $N \sim 10^{11}$ dislocations per cm^2 according to the formula of Klemens 1956) would explain the low lattice conductivity in this case. In Sb 2 not only are we faced with a small lattice conductivity below 4 or 5 K but also with a rather flat maximum at ~10 K and no very rapid variation of λ_g with temperature just above 10 K, i.e. between $\theta/20$ and $\theta/10$. This latter behaviour is similar to that in Ge, Si and Te but contrasts with that in bismuth or in solid helium, sapphire and diamond. It is tempting to attribute this flattening to the presence of other isotopes which contribute a point defect scattering term, W_P, to the thermal resistivity, a term sufficient to mask the sharp maximum such as is observed in bismuth. Bismuth consists of one stable isotope whereas antimony consists of two: Mass 121 (56%) and mass 123 (44%). However, a calculation of the isotope scattering term, W_P, using an equation due to Klemens (1957) yields $W_P^{-1} \equiv \lambda_P \simeq 1000/T$ watts per cm deg. It appears, therefore, that the presence of more than one isotopic species cannot be responsible for limiting the maximum. Perhaps there are sufficient free electrons present in antimony to modify the lattice conductivity at low temperatures although in bismuth there is no evidence of such a phonon–electron scattering process.

Consider now the electronic thermal conductivity of antimony as exemplified by specimen Sb 2 or Sb 2a. It appears similar to the thermal

conductivity of a metallic element in which there is about one free electron per atom. Assuming the validity of Matthiessen's rule for thermal resistivity we may write

$$1/\lambda_e \equiv W_e = W_0 + W_i.$$

Now at 2°K, $W_i \ll W_0$ and from values of the electronic thermal conductivity and the electrical resistivity, ρ_0, in this temperature region we obtain $\rho_0/W_0T \simeq 2{\cdot}3_3 \times 10^{-8}$ $W\,\Omega$ deg^{-2} for Sb 2. Assuming that the factor, W_0T, remains constant as the temperature is increased we have calculated values for the ideal thermal resistivity, W_i. As shown in fig. 8, W_i appears to be approaching a constant value of $W_\infty \simeq 7$ cm deg W^{-1} at high temperatures, which compares with a value of about 6 cm deg W^{-1} calculated from the electrical resisitivity near room temperature, using the Wiedemann–Franz–Lorenz law.

Fig. 8

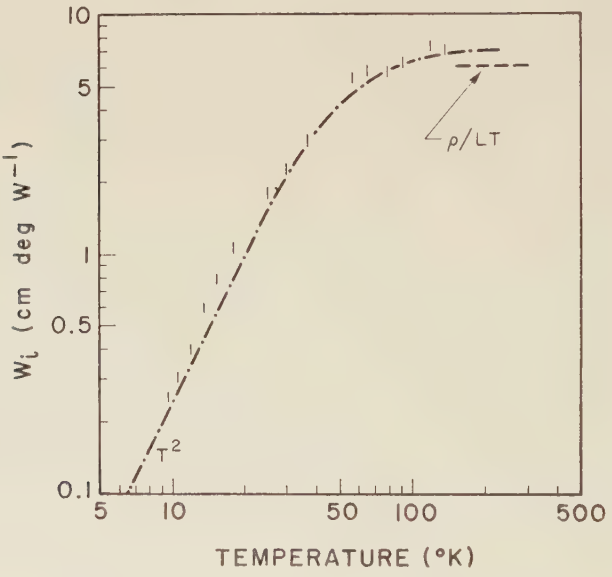

Values of 'ideal' electronic thermal resistivity, W_i, deduced for antimony. The broken curve represents $W_i = 2W_\infty(T/\theta)^2 J_3(\theta/T)$ assuming $\theta = 200°$K, and $W_\infty \simeq 7{\cdot}5$ cm deg W^{-1}.

At low temperatures, $W_i(T)$ is not very different from the function mentioned earlier:-

$$W_i = 2W_\infty(T/\theta)^2 \int_0^{\theta/T} \frac{x^3\,dx}{(e^x - 1)(1 - e^{-x})}$$

$$= 2W_\infty(T/\theta)^2 \quad J_3(\theta/T).$$

This semi-empirical function gives a useful representation of data for the alkali metals and many divalent and transition elements but it seems a little surprising that it may be extended to cover, even in an approximate fashion, data for antimony.

4.2. *Electrical Resistivity*

General. For a simple metal in which the charge carriers are free electrons in a single band the Grüneisen Bloch relation predicts

$$\rho_i \propto \frac{T^5}{\theta^6} \int_0^{\theta/T} \frac{x^5\,dx}{(e^x-1)(1-e^{-x})} \equiv (T^5/\theta^6)\, J_5(\theta/T)$$

which for $T \ll \theta$ reduces to

$$\rho_i \propto T^5.$$

If the characteristic temperature, θ, is identified with the Debye temperature, θ_D†, good agreement with experiment is obtained in the case of sodium. For other monovalent metals the T^5 dependence is usually observed at very low temperatures, but a value of θ somewhat less than θ_D may be required to give good agreement with experiment for the ratio of low and high temperature values.

For the transition elements in which the charge carriers in two bands (s and d bands) have very different effective masses, Wilson (1938) has shown that, provided interband transitions are not forbidden by momentum conservation requirements, there should be a large additional resistivity,

$$\rho_{sd} \propto (T/\theta)^3 \int_0^{\theta/T} \frac{x^3\,dx}{(e^x-1)(1-e^{-x})} \equiv (T/\theta)^3 \quad J_3(\theta/T).$$

$$\text{For } T \ll \theta, \quad \rho_{sd} \propto T^3.$$

In elements like antimony and bismuth, requirements of momentum conservation have a further effect (Sondheimer 1952). Only those lattice waves with wave number, q, smaller in magnitude than $2|\mathbf{k}|$ may interact with electrons having wave vector, $\mathbf{k}$, and for the electrons at the surface of the Fermi distribution $\mathbf{k}$ will be small in bismuth and antimony. Hence at normal temperatures the small number of free electrons may only interact with a relatively small group of phonons; thereby they have a large mean free path and also the range over which $\rho \propto T$ is extended to quite low temperatures.

Bismuth and Antimony. In both these elements, our data for the polycrystalline specimens (fig. 4) indicate that for $T \leqslant \theta/10$, $\rho \propto T^{2\cdot75}$. For bismuth, however, the transition from an approximately linear dependence at higher temperatures to this $T^{2\cdot7}$ dependence is much more sudden than for antimony. For neither element do the results appear to follow a Grüneisen–Bloch function, but for antimony ρ_i may be fitted

† θ_D as determined from specific heat data obtained in the range of temperature between $T \simeq \theta_D/2$ and $T \simeq \theta_D$.

tolerably well by the $(T/\theta)^3 J_3(\theta/T)$ function assuming $\theta = \theta_D \simeq 200°$K. Thus the ratio, $\rho_i(\theta/10)/\rho_i(\theta)$, has values of 0·005 for the Grüneisen-Bloch function, 0·015 for the Wilson function, while experimentally it has the values 0·015 in Sb, and 0·046 in Bi (assuming $\theta = \theta_D = 120$ K for bismuth). This at least suggests that interband transitions are important in antimony and perhaps also in bismuth but are modified in bismuth by the smaller number of free electrons which cause an extension of the temperature region over which elastic scattering occurs, i.e. over which $\rho \propto T$.

§ 5. Conclusions

(*a*) For pure bismuth, the heat transported by the lattice waves is very much greater than by the electrons ($\lambda_g \gg \lambda_e$) at temperatures below 50°K, and the lattice thermal conductivity is limited by the presence of grain boundaries and Umklapp processes in much the same way as it is limited in a pure dielectric crystal. No useful information about the minor component, λ_e, can be deduced as yet for the interesting temperature range below 50°K.

(*b*) For pure antimony the two components of conductivity are comparable except at very low or high temperatures. The electronic component, λ_e, behaves very like that in a simple monovalent metal. The lattice component, λ_g, at temperatures above 20°K, appears to be limited by anharmonic interaction between lattice waves but at low temperatures is much smaller than we should expect for a crystalline insulator (or than is observed for bismuth) suggesting that free electrons may seriously scatter the lattice waves.

(*c*) The electrical resistivity of both elements varies as about $T^{2·75}$ below $\theta/10$ and depends linearly on T at high temperatures. For bismuth this linear region seems to extend to considerably lower temperatures than for antimony. Interband scattering may be important in determining the temperature dependence of the electrical resistivity.

Acknowledgments

We are very happy to thank Mr. Gaston Fischer for his considerable help in preparing some of these specimens, Dr. D. K. C. MacDonald for his helpful comments, and Messrs. F. Richardson and J. Broome for providing liquid helium.

References

Barron, T. H. K., 1956, *Nature, Lond.*, **178**, 871.
Berman, R., 1953, *Advanc. Phys.*, **2**, 103.
Casimir, H. B. G., 1938, *Physica*, **5**, 495.
Dugdale, J. S., and MacDonald, D. K. C., 1955, *Phys. Rev.*, **98**, 1751.
Fischer, G., White, G. K., and Woods, S. B., 1957, *Phys. Rev.*, **106**, 480.
Gehlhoff, G., and Neumeier, F., 1913, *Verhand. Deutsch. Physik. Gesell.*, **15**, 876.
Gerritsen, A. N., 1956, *Handb. der Physik*, **19**, 137.
Grüneisen, E., Rausch, K., and Weiss, K., 1950, *Ann. Phys.*, **7**, 1.
Keesom, P. H., and Pearlman, N., 1956, *Handb. der Physik*, **14**, 282.

KLEMENS, P. G., 1956, *Handb. der Physik*, **14**, 198 ; 1957, *Proc. phys. Soc. Lond.* A, **70**, 833.

KONTOROVA, T. A., 1957, *Soviet Physics* (*Technical Physics*), **1**, 1959. (Translation from *J. Tech. Phys. U.S.S.R.* 1956, **26**, 2021 by American Inst. Phys.).

LEIBFRIED, G., and SCHLÖMANN, E., 1954, *Nachr. Gött.*, **11***a*, 71.

MACDONALD, D. K. C., WHITE, G. K., and WOODS, S. B., 1956, *Proc. roy. Soc.* A, **235**, 358.

MOTT, N. F., and JONES, H., 1936, *Theory of the Properties of Metals and Alloys* (Oxford : University Press).

OLSEN, J. L., and ROSENBERG, H. M., 1953, *Advanc. Phys.*, **2**, 28.

POWELL, R. L., and BLANPIED, W. A., 1954, *Nat. Bur. Stand. Circ.* 556, U.S. Govt. Printing Office, Wash., D.C.

RAUSCH, K., 1947, *Ann. Phys.*, **1**, 190.

REDDEMANN, H., 1934, *Ann. Phys.*, **20**, 441.

REITZ, J. F., 1955, *Solid State Physics*, **1**, 1 (Editors : F. Seitz and D. Turnbull) (New York : Academic Press Inc.).

ROSENBERG, H. M., 1955, *Phil. Trans.*, **247**, 441.

SCHUBNIKOW, L., and DE HAAS W. J., 1930, *Leiden Communications* 207 c.

SHALYT, S., 1944, *J. Phys. U.S.S.R.*, **8**, 315.

SHOENBERG, D., 1952, *Phil. Trans.*, **245**, 1.

SONDHEIMER, E. H., 1952, *Proc. phys. Soc. Lond.* A, **65**, 561.

WHITE, G. K., 1956, *Canad. J. Phys.*, **34**, 1328.

WHITE, G. K., and WOODS, S. B., 1955, *Canad. J. Phys.*, **33**, 58 ; 1956, *Phys. Rev.*, **103**, 569 ; 1957 a, *Proc. Int. Conf. on Low Temp. Phys. and Chem., Wisconsin*, Paper 7–5 ; 1957 b, *Proc.* 1956 *Cryog. Eng. Conf.*, p. 120, N.B.S., Boulder, Colorado.

WILSON, A. H., 1938, *Proc. roy. Soc.* A, **167**, 580 ; 1953, *The Theory of Metals*, 2nd Ed. (Cambridge : University Press).

The Polarization of Luminescence in Diamond†

By R. J. Elliott‡, I. G. Matthews§ and E. W. J. Mitchell
Physics Research Laboratory, The University of Reading

[Received January 1, 1958]

Abstract

It is shown that the polarization of luminescence from a cubic crystal, when excited by plane polarized light, may be used to determine the symmetry axes of the luminescent centres. This information is most readily obtained from a specimen which is bounded by (100) faces and by using light travelling normally to the faces. Experiments on a diamond cut in this way are described. The results are for the green luminescence from centres induced by heat treatment after irradiation. These centres appear to have symmetry axes along ⟨110⟩ directions.

§ 1. Introduction

Many of the optical properties of cubic crystals are isotropic, and it is not then possible to obtain any information about the symmetry of the centres which give rise to these properties. The polarization of light emitted by centres excited by plane polarized light is, however, anisotropic. This effect was first reported by Feofilov (1953, 1956) who investigated various centres in CaF_2, LiF, and NaF. In the present note, measurements on diamond will be described, the method used being somewhat different. The optimum crystal directions were chosen on the basis of the theory of the effect, the relevant results of which are summarized, and from the results the axes of the centres are determined.

There are two main luminescent centres in diamonds, the emission being in the blue and the green respectively. The latter centre can be induced in type I diamonds by heat treatment after electron, gamma or pile irradiation. Clark *et al.* (1956) found that the absorption spectrum associated with this centre, when measured at liquid air temperature, consisted of a sharp line at 5035 Å with a fine structure of other lines superimposed on a broad band on the high energy side of the line. The emission spectrum is similar (Dyer and Matthews 1958) except that the structure is on the low energy side of the main emission line at 5032 Å.

In this paper we report measurements on the green emitting centre when stimulated with 3650 Å and 4358 Å mercury radiation. Experiments are continuing both on this and on the blue centre under varying conditions and these will be reported later with a fuller theoretical discussion.

† Communicated by the Authors.
‡ Now at The Clarendon Laboratory, Oxford.
§ Now at A.W.R.E., Aldermaston.

§ 2. Experimental

The apparatus is shown diagrammatically in fig. 1. When using 3650 Å excitation, light from a high pressure mercury lamp passed through a black glass filter (Chance –OX1) which cut out the visible light. In 4358 Å excitation the light from the lamp was dispersed by a f/3 glass prism Littrow spectrograph, the line selected by a slit and passed through three OB10 filters to remove a small amount of scattered green light. A Glan-Thomson prism P was used to polarize the exciting light which was then focused onto the diamond. The green emission

Fig. 1

Optical system. (S, source ; P, Glan-Thomson polarizer ; F_1 and F_2, filters ; L, lens ; D, diamond ; R, rotating polaroid ; and Ph.X, photomultiplier.)

Fig. 2

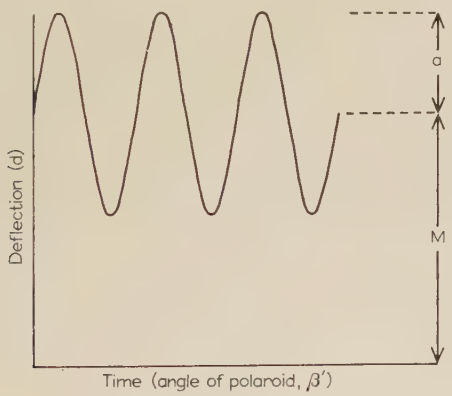

Photomultiplier signal as a function of time.

from the diamond was concentrated by the lens L and passed through two non-luminescent, green transmitting filters (OY4, OGr1). The emitted light was analysed by a continuously rotating polaroid and detected by a 14-stage photomultiplier. From the photomultiplier the output was fed either to a galvanometer or to a Brown recorder.

The light intensity recorded as a function of time (which is proportional to the angle of rotation of the analyser) was of the form shown in fig. 2.

In the experiments to be described the degree of polarization (p)—defined as the amplitude (a) of the oscillation divided by the mean value (M)—has been determined as a function of the angle of the electric vector **E** of the exciting light relative to the crystal axes.

§ 3. Theory

We begin by assuming the simplest forms of the symmetry of the centres in the crystal, namely that each centre has an axis of symmetry. If a typical direction of this axis is, say $\langle \lambda_i, \mu_i, \nu_i \rangle$, there will be 23 other directions which are equivalent in a cubic crystal and there will be equal numbers of centres having these 24 axes. In any particular centre with axis z, the energy levels may be singlets or doublets. For example, s and p_z states would be singlets whereas the $p_x p_y$ state would be a doublet. If the transition involved is an allowed electric dipole transition it may be of two kinds, one corresponding to what are usually called π oscillators, the other to σ oscillators. The first, of which the s–p_z transition is a typical example, has an intensity of absorption proportional to $\cos^2\theta_i$ where θ_i is the angle between the axis of symmetry Z_i and the **E** vector of the exciting light. The second has intensity proportional to $\sin^2\theta_i$ and the s–p_x, p_y transition is a typical case. The intensity of absorption in the crystal is obtained by summing $\cos^2\theta_i$, or $\sin^2\theta_i$ over all the equivalent directions. This sum is independent of the direction of **E** and the absorption is isotropic.

The absorption of the centre in diamond was observed to be isotropic and we therefore conclude that the absorption is dipolar in character. Also, although it is not possible to find the number of centres accurately, rough estimates of the number of vacancies and interstitials produced in the irradiation indicate that the f-value of the transition is of the order of 10^{-1}. We therefore rule out magnetic dipole and conclude that the transition is allowed electric dipole.

If the light is emitted by the same π oscillator in which absorption took place the intensity of emitted light with **E** vector making an angle θ_i' with axis Z_i is proportional to $\cos^2\theta_i \cos^2\theta_i'$. If the direction cosines of the **E** vector of the exciting light are (l, m, n) the intensity emitted with **E** vector (l', m', n') by the crystal is

$$I = I_0 \sum_i (l\lambda_i + m\mu_i + n\nu_i)^2 (l'\lambda_i + m'\mu_i + n'\nu_i)^2. \quad . \quad . \quad . \quad (1)$$

where I_0 depends on the experimental conditions and the properties of the centres (f-value and luminescent efficiency). This may be written

$$I = \tfrac{1}{3} I_0 \{ \sum_{lmn} l^2 l'^2 + [\sum_i \lambda_i^2 \mu_i^2][1 + 2(\sum_{lmn} ll')^2 - 5 \sum_{lmn} l^2 l'^2] \}, \quad . \quad (2)$$

where the sums are over the three principal directions. For σ oscillators the expression is very similar,

$$I = \tfrac{1}{3} I_0 \{ 1 + \sum_{lmn} l^2 l'^2 + [\sum_i \lambda_i^2 \mu_i^2][1 + 2(\sum_{lmn} ll')^2 - 5 \sum_{lmn} l^2 l'^2] \}. \quad . \quad (3)$$

$(\lambda_i^2\mu_i^2+\mu_i^2\nu_i^2+\nu_i^2\lambda_i^2)$ is constant for the equivalent directions in a cubic crystal and its value characterizes the polarization of the luminescence. It varies from 0 for ⟨100⟩ centres to $\frac{1}{3}$ for ⟨111⟩. For intermediate values there are an infinity of directions of the axes which give the same result. However, if the centre is of atomic size it is likely to have symmetry axes which are related to the atomic arrangement in the crystal, and are therefore in directions of high symmetry. For this reason centres with ⟨110⟩ axes are also studied for which $\sum_i \lambda_i^2\mu_i^2=\frac{1}{4}$. (⟨211⟩ centres give the same value but are unlikely to occur in the diamond structure.)

Many variations of the formulae are possible if more than two energy levels are involved in the process, and the system can make transitions between separate excited levels before fluorescing, or if the centres can change their symmetry axes when excited into high energy vibrational states. In this note, however, we shall simply test the applicability of the simple theory.

§ 4. Formulae for Experimental Conditions

In the experiment a rectangular block is used and the light enters and leaves the crystal perpendicular to two faces which may be parallel or at right angles. A direction normal to another face which is perpendicular to the light paths is chosen and the direction of the **E** vectors (l, m, n), (l', m', n') are measured as angles β, β' from this direction. Equations (2) and (3) may then be written in the form

$$I=M(\beta)+2A(\beta)\cos 2\beta'+2B(\beta)\sin 2\beta'. \quad . \quad . \quad . \quad (4)$$

In the experiment we cannot determine the intensity of light emitted having **E** at angle β'—we can only use an analyser with its easy direction along β' so that a fraction $\cos^2\theta_p$ of emitted light having **E** at any angle θ_p from the easy direction is also transmitted. Thus for any collection of dipole oscillators the deflection (d) cannot go to zero, the maximum value of p being 0·5 which would be obtained, for example, with a single dipole oscillator.

It is convenient to express the deflection (d) corresponding to the photomultiplier current as

$$d=M(\beta)+a(\beta)\cos 2\,[\beta'-\epsilon(\beta)], \quad . \quad . \quad . \quad . \quad . \quad (5)$$

where $M(\beta)$, $a(\beta)$ and $\epsilon(\beta)$ are the mean, amplitude and phase of the oscillatory trace in fig. 2. The amplitude is related to the constants A and B by $a(\beta)=(A^2+B^2)^{1/2}$ and the phase by $\tan^{-1} 2\epsilon(\beta)=B/A$.

For rectangular crystals cut in a general direction the expressions for M, A and B are complicated and because the values of $\sum_i \lambda_i^2\mu_i^2$ are not very different for the ⟨111⟩ and ⟨110⟩ centres it is sometimes difficult to distinguish these two centres.

Fig. 3

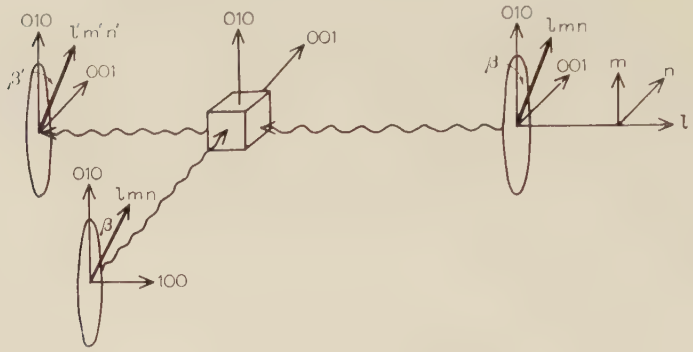

Definitions of directions.

Fig. 4

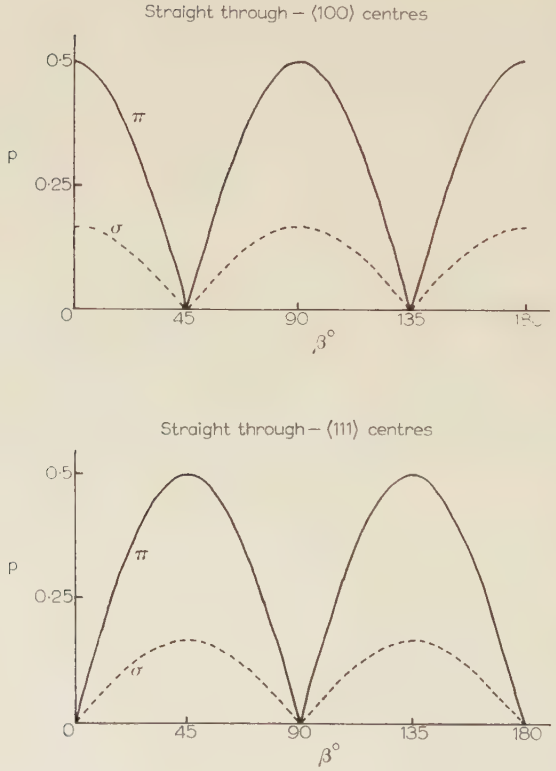

Theoretical curves for the variation of p with β for $\langle 100 \rangle$ and $\langle 111 \rangle$ centres, viewing parallel to the incident light.

Values of the Parameters a, M and ϵ for Different Conditions

Type of Experiment	Centre	$a_\sigma(=a_\pi)$	$\tan 2\epsilon_\sigma$ $(=\tan 2\epsilon_\pi)$	M_π	p_π	M_σ	p_σ
Straight through	100	$(I_0 \cos 2\beta)/12$	0	$I_0/6$	$\frac{1}{2}\cos 2\beta$	$I_0/2$	$\frac{1}{6}\cos 2\beta$
	110	$I_0(\frac{1}{4}\cos^2 2\beta + \sin^2 2\beta)^{1/2}/24$	$2\tan 2\beta$	$I_0/8$	$\frac{1}{3}(\frac{1}{4}\cos^2 2\beta + \sin^2 2\beta)^{1/2}$	$11\ I_0\ 24$	$\frac{1}{11}(\frac{1}{4}\cos^2 2\beta - \sin^2 2\beta)^{1/2}$
	111	$(I_0 \sin 2\beta)/18$	∞	$I_0/9$	$\frac{1}{2}\sin 2\beta$	$4\ I_0/9$	$\frac{1}{8}\sin 2\beta$
Perpendicular	100	$I_0(1+\cos 2\beta)/24$	0	$I_0(1+\cos 2\beta)/12$	$\frac{1}{2}$	$I_0(5+\cos 2\beta)/12$	$\frac{\frac{1}{2}(1+\cos 2\beta)}{(5+\cos 2\beta)}$
	110	$I_0(1+\cos 2\beta)/96$	0	$I_0(5+\cos 2\beta)/48$	$\frac{\frac{1}{2}(1+\cos 2\beta)}{(5+\cos 2\beta)}$	$I_0(21+\cos 2\beta)/48$	$\frac{\frac{1}{6}(1+\cos 2\beta)}{(21+\cos 2\beta)}$
	111	0	0	$I_0/9$	0	$4\ I_0/9$	0

The simplest expression for d and the maximum distinction between $\langle 100 \rangle$, $\langle 110 \rangle$ and $\langle 111 \rangle$ centres is obtained when the specimen has (100) faces. The angles β and β' are then defined as shown in fig. 3 and from eqns. (2) and (3) we obtain the values shown in the table. Figures 4, 5 and 6 show the variation of ρ with β for σ and π oscillators under

Fig. 5

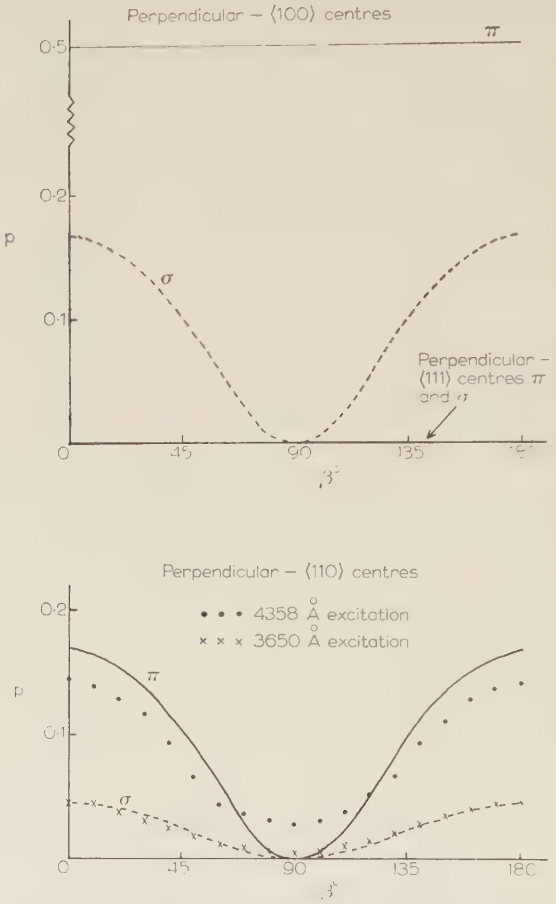

Comparison of experimental results with the theoretical curves for the variation of ρ with β for $\langle 100 \rangle$, $\langle 110 \rangle$ and $\langle 111 \rangle$ centres, viewing perpendicular to the incident light.

various conditions. It will be seen that the shapes of the curves are the same in the two cases, but that the values of ρ are less for the σ oscillators owing to a constant being added to M. This depolarization arises because, when viewed along the z-axis the σ oscillators emit circularly

polarized light, which leads to a constant contribution to the intensity transmitted by the rotating analyser.

§ 5. Results and Discussion

Dr. J. F. H. Custers of the Diamond Research Laboratory, Johannesburg, kindly prepared for us a specimen in the form of a cube bounded, within 2°, by (100) faces. This crystal was given successive pile irradiation and heat treatment (800°c) until a sufficiently strong 5032 Å system was present.

The crystal was birefringent along one direction but measurements were made for the other two straight through positions and the two right

Fig. 6

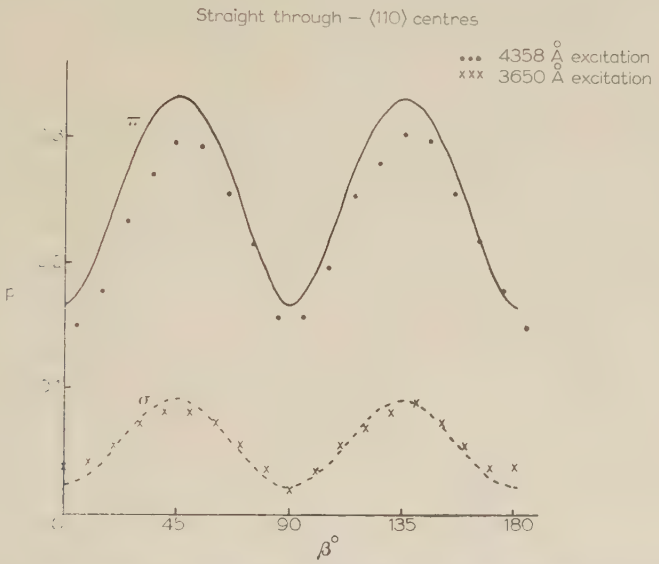

Comparison of experimental results with the theoretical curves for the variation of p with β for ⟨110⟩ centres, viewing parallel to the incident light.

angle positions not involving the birefringent direction. Because of the low conversion efficiency it was necessary to use a high pressure mercury lamp for the source. While the lamp was sufficiently stable to obtain reasonably accurate values of a/M for different values of β, we were not able to obtain experimentally reliable values of a and M separately.

Experiments were carried out using 4358, 4047 and 3650 Å excitation. The results for 4358 and 3650 are shown in figs. 5 and 6. Excitation with 4047 Å gave values of p equal, within the experimental error of about $\pm 0{\cdot}005$, to those obtained when using 4358 Å—a result which was also found in another green emitting crystal whose faces were not cut in simple directions.

The experimental results in figs. 5 and 6 show a maximum value of p at $\beta = 45°$ in the straight through and at $\beta = 0$ in the perpendicular conditions. In the former case this eliminates $\langle 100 \rangle$ centres for which the maximum would be expected at $\beta = 0$. It is clear that for 4358 Å excitation the results can best be described by using π oscillators in centres having $\langle 110 \rangle$ axes.

We have discussed first the results for 4358 Å excitation because they give the highest values of p. It is then necessary to consider how p could be reduced to account for the results using 3650 Å excitation. The opposite approach is not possible because there do not seem to be any processes which would allow the degree of polarization from a given set of oscillators to be increased.

Although the results for 3650 Å excitation lie on the curves predicted for σ oscillators about $\langle 110 \rangle$ axes there are two points which indicate that this is not the correct explanation. First, one of us (I. G. M.) has found that the fluorescence spectra obtained with the two excitation wavelengths are the same. Thus the emission must involve the same energy levels in the two cases, and we have concluded above that for 4358 Å excitation these energy levels are associated with π oscillators. Moreover, measurements on the other green emitting crystal which was referred to earlier, show that changing the excitation from 4358 Å to 3650 Å can change the shape—as well as the scale—of the curves. We think, therefore, that some other process is present which gives a depolarization when the excitation wavelength is 3650 Å.

The depolarization may arise because the centre is excited into a higher excited level than that from which emission takes place. Such a level would have to have a small transition probability for excitation from the ground state since its absorption lines are not observed. In fact, the absorption at 3650 Å, as measured by Clark *et al.* (1956), is small and it was only the high intensity of illumination available at 3650 Å which made this a convenient source in preliminary experiments. The excitation might even be into the conduction band, as a result of which electrons could migrate from one centre to another and tend to destroy the polarization.

If on the other hand the excitation occurs into the excited electronic state which has a minimum energy of 2·46 ev (5032 Å), it does so to a state where the crystal has 0·93 ev of vibrational energy. Such excessive excitation might allow the centre to change its axes, thus giving less polarization.

Concerning the atomic nature of the centre Clark *et al.* (1956) have suggested that it is formed when a product of damage—vacancy or interstitial carbon atom—migrates to some other imperfection which might be an impurity atom. The simplest double defect having $\langle 110 \rangle$ axes is an interstitial carbon atom anchored to an interstitial impurity. Combinations such as vacancy/interstitial impurity, vacancy/substitutional impurity, or interstitial carbon substitutional impurity would be expected

to exhibit strong ⟨111⟩ directional properties. The next simplest combination having ⟨110⟩ would be a vacancy anchored to a substitutional impurity in a next nearest neighbour position.

Further experiments are in progress to enable measurements of the three parameters M, a and ϵ to be made separately and to determine the cause of the depolarization with 3650 Å excitation. The former seems to be entirely a problem of the stability of a source of the required intensity. Some gain should also be obtained by cooling the specimen to liquid nitrogen temperature, where a higher fluorescence efficiency is obtained (e.g. Dyer and Matthews 1957).

§ 6. Conclusion

The green emitting centre induced in a specially cut diamond by heat treatment after irradiation has been shown to have symmetry axes along ⟨110⟩.

Acknowledgments

We wish to thank Professor Ditchburn for his interest, Dr. C. D. Clark for valuable help with the experiments during the later stages and also Dr. J. F. H. Custers of the Diamond Research Laboratory, Johannesburg for his interest in the problem and for providing us with a suitably cut crystal. One of us (I. G. M.) wishes to acknowledge the receipt of a maintenance grant from Industrial Distributors (1946) Ltd. who also financed the research.

References

Clark, C. D., Ditchburn, R. W., and Dyer, H. B., 1956, *Proc. roy. Soc.* A, **237,** 75.

Dyer, H. B., and Matthews, I. G., 1957, *Proc. roy. Soc.* A, **243,** 320; 1958, *Ibid.* (in the press).

Feofilov, P., 1953, *Dokl. Akad. Nauk. S.S.S.R.*, **92,** No. 3, 545; 1956, *J. de Phys. et Rad.* (Proceedings of Paris Luminescence Conference, May 1956).

On a Feature of Galactic Radio Emission†

By Harriet Tunmer
Cavendish Laboratory, Cambridge

[Received January 9, 1958]

Abstract

Observations of the intensity distribution of radio emission have shown a bright belt approximately normal to the galactic plane and passing through the anti-centre. An explanation is suggested in terms of the highly anisotropic radiation from relativistic electrons moving in the magnetic field of the local spiral arm. This suggestion avoids the supposition that the sun is in a special position in the galaxy.

§ 1. Introduction

The observed distribution of radio brightness over the sky has been interpreted in terms of symmetrical models of the galaxy by a number of authors including Hanbury Brown and Hazard (1953) and Baldwin (1955 a). The latter has proposed a model whose main components are (i) a spherical halo about the galaxy, (ii) a disc-like distribution of sources concentrated towards the galactic plane and its centre (Westerhout and Oort 1951), and (iii) an isotropic distribution of extra-galactic sources.

Other less symmetrical features of the background radiation, which cannot be explained by the above model have been noted. The most important of these is a belt of emission from directions approximating to a great circle through the galactic poles and the plane at $l = 0^\circ$, and $l = 150^\circ$. It appears on a number of surveys, including among the most recent Baldwin (1955 b), Piddington and Trent (1956), Blythe (1957). A diagram indicating the position of this feature is shown in fig. 1, and cross sections showing the angular variation of intensity at two points in the belt are given in fig. 2; the latter curves were obtained by Blythe (1957) on 38 Mc/s. The intensity of the belt exceeds the isotropic component due to extra-galactic sources and the feature is therefore likely to be of galactic origin; it could be explained by an emitting disc, orientated normal to the galactic plane and containing the sun near its centre. If similar objects of the same brightness occurred elsewhere in the galaxy they would, however, be readily detectable individually, and would contribute the major part of the total galactic emission. No such objects have been observed, and it is the purpose of this paper to suggest an alternative explanation which avoids the assumption of any marked asymmetry of the galaxy. It is also an alternative to the proposal that there is a perturbing galaxy in collision with our own (Johnson 1957).

† Communicated by M. Ryle, F.R.S.

Fig. 1

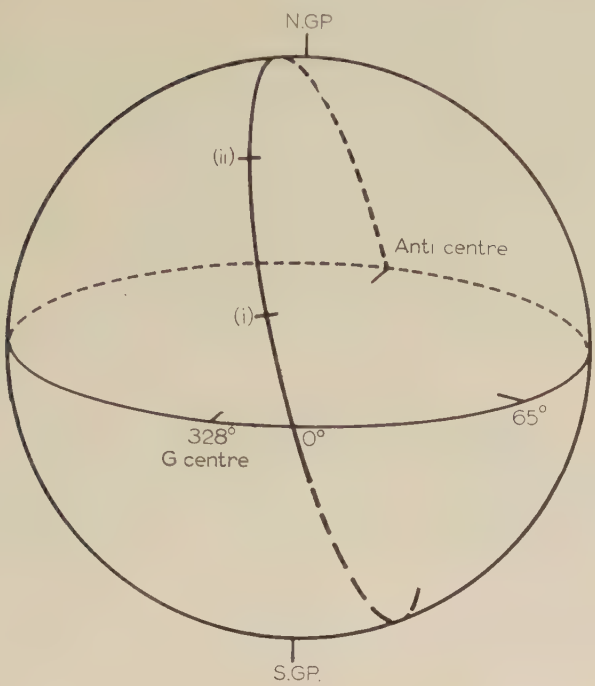

The broken line on the celestial sphere shows the belt's approximate position relative to the sun S, the galactic centre C and the galactic plane. (i) and (ii) mark the positions where cross sections have been plotted in fig. 2.

Fig. 2

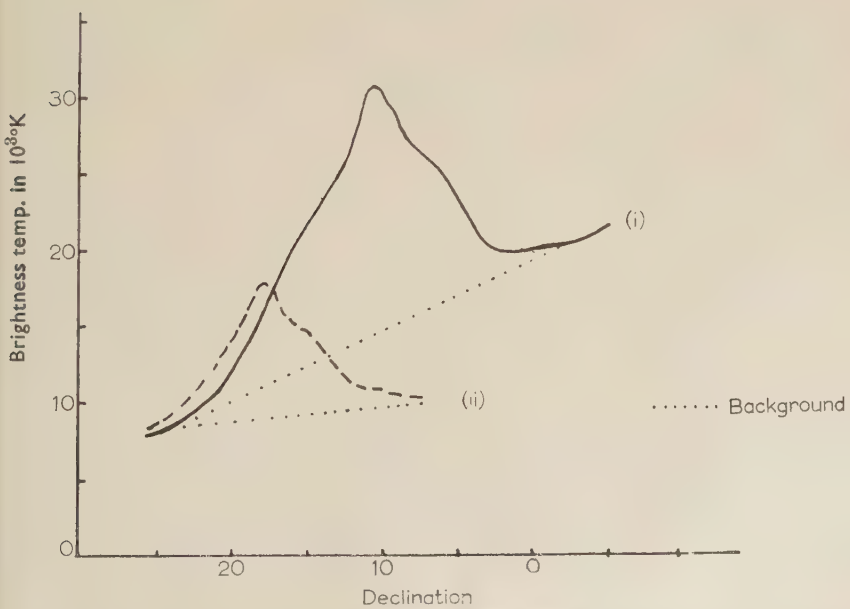

Two cross sections of the belt at galactic latitudes (i) 28° and (ii) 70°. At this longitude a distribution in declination is effectively the distribution across the belt.

The plane of the apparent emitting disc is almost perpendicular to the mean direction of the local spiral arm in the neighbourhood of the sun. It is shown in § 2 that the intensity is not uniform around this disc; the variation shows a reasonable similarity to the cross sectional shape of the local arm as revealed by observations of the 21 cm line of neutral hydrogen. This similarity, therefore, suggests that the belt may be due to a source of emission situated within this local arm.

The application of the synchrotron mechanism of radio emission (Shklovsky 1952) to relativistic electrons moving in a general magnetic field associated with the local spiral arm appears to present a possible explanation of the feature. It is shown in § 3 that the belt might arise from the anisotropic radio emission which would be expected under such conditions.

§ 2. The Local Spiral Arm

Observations of the 21 cm emission at different latitudes in the plane passing through the centre and anti-centre, normal to the galactic plane (Heeschen and Lilley 1954) have shown that the cross section of the local

Fig. 3

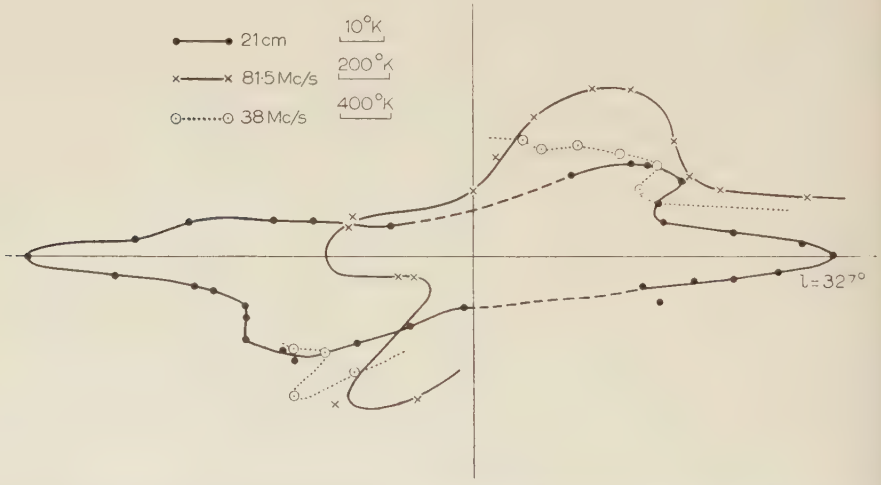

The distribution in galactic latitude of the maximum brightness temperature of the belt is compared to the cross section of the local arm as observed by Heeschen and Lilly (1954) at 21 cm.

arm is not symmetrical; it shows a marked flattening which does not coincide with the galactic plane but is inclined at about 20° to it. These observations are plotted in polar coordinates in fig. 3, together with a similar plot of the variation of the maximum intensity of the belt as derived from the surveys at 38 Mc/s and 81·5 Mc/s. The latter sets of

points do not correspond exactly to the plane of the 21 cm observations, since the belt makes a small angle to the plane through the centre and anti-centre.

The similarity between the curves suggests that the belt has its origin in the local arm and this possibility will now be examined. The existence within the arm of fast electrons having energies of at least 10^9 ev must be assumed†. The question of their origin is not yet answered with certainty. Following one suggestion (Fermi 1949 and 1954, Kaplan 1956), it will be assumed that they appear with the cosmic rays in regions where there are dense clouds in random turbulent motion. Near the sun, however, they are in the presence of an ordered magnetic field along the spiral arm for which there is quite independent evidence (Hiltner 1951, Davis and Greenstein 1951), the electrons would here spiral smoothly with a radius of curvature of the order of 2×10^{-7} pc. Their lifetime is limited by nuclear collisions to roughly 10^7 years but for this time they are effectively tied to the lines of force. This field, according to Fermi and Chandrasekhar (1953), is of the order of 6×10^{-6} gauss and is regular in direction to within 5° over distances up to 1 kpc. The regions where turbulent clouds exist and where the electrons are supposed to be accelerated are presumably further away than this. It will be supposed that such regions are confined to the inner parts of the galaxy entirely, in which case the electrons leave the inner turbulent region, follow the smooth field along the spiral arm and are eventually lost in the halo.

§ 3. The Suggested Mechanism

The acceleration of fast electrons in regions of turbulent cloud motion will presumably give rise to an isotropic distribution of electron velocities. If such particles now diffuse outwards along the ordered magnetic field associated with the spiral arm, those having initial velocities nearly parallel to the field will move quickly into the outer parts of the galaxy, while those whose initial velocities are nearly perpendicular to the field will move comparatively slowly. At any point along the spiral arm there will, therefore, be many more electrons per unit volume having motions across the magnetic field than those with motions along it.

Since the radio emission from a relativistic electron moving in a magnetic field is confined to directions very near the instantaneous velocity vector, the emission per unit volume will be stronger in directions perpendicular to the magnetic field than in directions along it. It can be shown then if L is the distance through which the electrons have drifted in the ordered field and T is their lifetime, then the intensity of the radio emission has a maximum at an angle $\cos^{-1}(L/cT)$ to the magnetic field, and that the radiation is restricted to an angular width of approximately L/cT radians.

† This value is the average of the energies calculated as those chiefly responsible for the Cambridge Survey frequencies of 38 Mc/s and 81·5 Mc/s, assuming a magnetic field of 6×10^{-6} gauss.

If $L = 1$ kpc and $T = 10^7$ years, the radiation is emitted at an angle of 89° 59′ to the field with a half-width of 1′. A uniform field would therefore give rise to an extremely narrow disc of emission practically normal to the field direction. The actual configuration of the magnetic field of the spiral arm may be compared to a rough skein of wool, each strand representing a line of force; the variation of emission from the whole cross section of the spiral arm will then correspond to the variation in the direction of the magnetic field. Fermi and Chandrasekhar's value for the latter is of the same order as the observed width of the belt.

In order to account for the observed brightness of the belt, it must be supposed that the number density of fast electrons is about 20 times that in the halo (Baldwin 1955 a).

If the halo is supplied by the drift of electrons from the inner part of the galaxy along the spiral arms, the ratio of the volume of the halo and the spiral arms would lead to a ratio of this order of magnitude.

In addition to the radio emission from the local spiral arm, the mechanism suggested would also produce emission which would be detectable from regions in other spiral arms where the line of sight was perpendicular to the arm. The large increase in intensity observed at low latitudes within 10° of the galactic centre and anti-centre may be explained in this way; the latter feature is particularly difficult to explain by any other mechanisms.

It is also possible that some of the anomalies between the distribution of radio and optical brightness in certain external galaxies might be explained; a spiral galaxy would exhibit an additional component of radio emission in the form of a strip perpendicular to the major axis.

§ 4. Discussion

It has been shown how this belt, an otherwise anomalous feature of galactic radio emission, may be due an isotropic distribution of the fast electron velocities near the sun, and how this distribution might arise. No special position need be assumed for the sun because a similar belt would be observed wherever the sun were placed within the spiral arm. The brightness and its variation with latitude are consistent with other data on the local arm. On the other hand, three major objections may be raised. (i) No similar anisotropy has been observed in the cosmic ray flux at the earth; (ii) the direction of the local spiral arm does not coincide with the axis of the belt; (iii) although synchrotron radiation is completely polarized, Thomson (1957) found less than 1% polarization in the belt.

As for the first objection, one would expect cosmic rays observed at the earth to have been affected by the extremely local fields of the solar system. The emitting electrons are outside this region. These fields are sufficient to make the cosmic ray flux isotropic if they are of the order of 10^{-5} gauss (Richtmyer and Teller 1949). At energies of 10^{17} ev, however, it is interesting to note that a slight minimum has been observed as the earth faces inward along the spiral arm (Cranshaw and Galbraith 1954).

The second objection is that the plane of the belt is normal to longitude 70°, whereas from 21 cm observations Westerhout (1957) has deduced that the Orion arm is directed towards longitude 65°. This discrepancy and the finite width of the belt would readily be explained if the direction of the magnetic field were supposed to show variations of the order of 5° as shown in fig. 4. Since the radiation is emitted within a very small angle perpendicular to the direction of the local magnetic field, those regions which contribute to the received radiation lie on a curve such as C in fig. 4; the angular width of the belt would therefore be of the same order as the deviations in the direction of the field.

Fig. 4

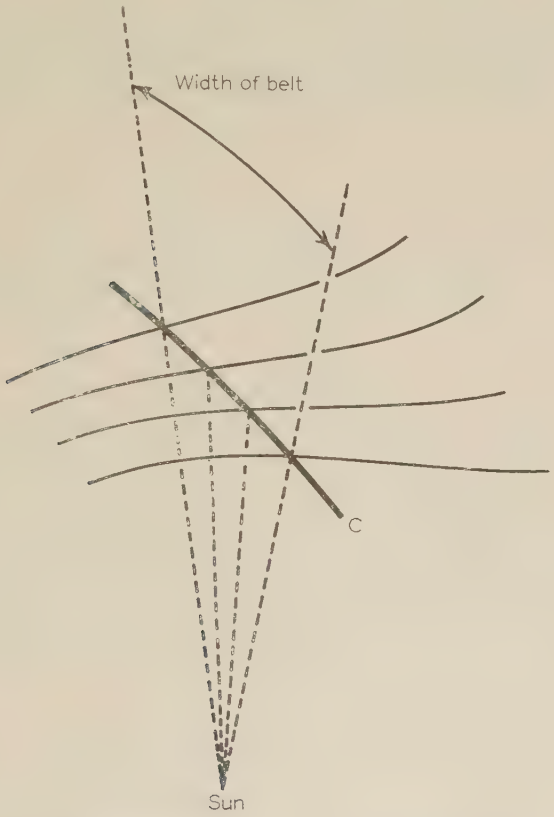

Diagram to illustrate a possible type of local magnetic field. The source elements lie along the curve C, the locus of points at which the line of sight is normal to the lines of force.

If this interpretation of the angular width of the belt is correct, the absence of appreciable polarization may be explained in terms of the Faraday rotation of the electric vector caused by the small longitudinal component of the field in the medium between the emitting element and

the earth. The emission from each element undergoes a rotation of its plane of polarization whose magnitude increases progressively with the distance of the element, since for simple fields of the type shown, the sign of the longitudinal component of magnetic field is constant. If the angle of rotation induced between the nearest and the most remote elements is appreciably greater than π, the resulting polarization may be small. For an electron density of 0·1 cm^3 within the spiral arm (Westerhout and Oort 1951) and the observed angular width of the belt of 5°, corresponding to an average longitudinal component of the field of 10^{-7} gauss, the angle of rotation for the frequency used by Thomson (160 Mc/s) is of the order of 0·03 radians per parsec.

It is therefore possible that for emitting elements extending over a depth of 100–150 parsec, the resultant polarization will be greatly reduced. If this interpretation is correct, observations at higher frequencies, or with sufficient angular resolving power to observe only part of the belt, might be successful in detecting an appreciable polarization.

Acknowledgments

This work was carried out at the Mullard Radio Astronomy Observatory, Cambridge. The author would like to thank Mr. Ryle for much patient and valuable discussion, the Canadian Federation of University Women for their Travelling Fellowship (1956) and Girton College for a Tucker–Price Studentship.

References

Baldwin, J. E., 1955 a, *Mon. Not. R. astr. Soc.*, **115**, 690 ; 1955 b, *Ibid.*, **115**. 684.
Blythe, J. H., 1957, *Mon. Not. R. astr. Soc.*, **117**, 652.
Cranshaw, T. E., and Galbraith, W., 1954, *Phil. Mag.*, **45** 1109.
Davis, L., and Greenstein, J. L., 1951, *Astrophys. J.*, **114**, 206.
Fermi, E., 1949, *Phys. Rev.*, **75**, 1169 ; 1954, *Astrophys. J.*, **119**, 1.
Fermi, E., and Chandrasekhar, S., 1953, *Astrophys. J.*, **118**, 113.
Hanbury Brown, R., and Hazard, C., 1953, *Phil. Mag.*, **44**, 939.
Heeschen, D. S., and Lilly, A. E., 1954, *Harvard Observatory Reports*, 396.
Hiltner, W. A., 1951, *Astrophys. J.*, **114**, 241.
Johnson, H. M., 1957, *Publ. astro. Soc. Pacif.*, **69**, 130.
Kaplan, S. A., 1956, *J. exp. theor. Phys.*, **2**, 203.
Piddington, J. H., and Trent, G. H., 1956, *Astro. J. Pacif.*, **9**, 481.
Richtmyer, R. D., and Teller, E., 1949, *Phys. Rev.*, **75**, 1729.
Shklovsky, I. S., 1952, *Astro. J., Moscow*, **29**, 418.
Thomson, J. H., 1957, *Nature, Lond.*, **180**, 495.
Westerhout, G., 1957, *Bull. astro. Netherlds*, **13**, 201.
Westerhout, G., and Oort, J. H., 1951, *Bull. astro. Netherlds*, **11**, 323.

Observations on Extensive Air Showers
V. The Size Spectrum of Showers containing 3×10^6 3×10^8 Particles†

By T. E. Cranshaw, J. de Beer‡, W. Galbraith and N. A. Porter
Atomic Energy Research Establishment, Harwell

[Received January 7, 1958]

Abstract

A lattice arrangement of G.M. counters has been used to measure the size spectrum of showers containing 3×10^6–3×10^8 particles. In this region, a power law distribution is found,

$$J(\geqslant N) = 9{\cdot}5 \times 10^{-5}(10^6/N)^{1{\cdot}88 \pm 0{\cdot}15} \text{ m}^{-2} \text{ hr}^{-1} \text{ ster}^{-1}.$$

An independent method of measuring the number of particles in the showers gave good agreement with these figures.

§ 1. Introduction

We have used the apparatus described in I (Cranshaw and Galbraith 1957) to derive the size spectrum of air showers in the region 3×10^6–3×10^8 particles. The method consists in determining the size spectrum in terms of the number of units of the array which are triggered, and calculating with the aid of the density distribution measured in III (Cranshaw, Galbraith and Porter 1957) the corresponding size spectrum in numbers of particles. Finally an independent measurement of the mean number of particles in the shower triggering a given number of units was made, and this measurement is found to agree satisfactorily with the values calculated from the spectrum. This agreement gives confidence in the correctness of the assumptions in III. In particular, the number of particles in showers can be determined by density measurements at about 100–200 m, and the use of the Nishimura and Kamata curve.

§ 2. Experimental Data

For the analysis, we wish to know the rate of showers which would discharge given numbers of units on an infinite lattice array with the spacing of our experimental array. For this purpose, we used the punched cards showing the units struck on the array. In order to minimize edge effects, an area inside the array was marked out as shown in fig. 1. For $\geqslant 3$ fold, $\geqslant 5$ fold or $\geqslant 8$ fold showers, showers were accepted if the centroid of the units struck lay inside the smaller area. It is assumed that on the average the centroid of the units struck coincides with the core of the

† Communicated by the Authors.
‡ On leave from the University of Potchefstrom, South Africa.

shower. For large showers, the whole of the array was accepted and visual estimates of the core of the shower were made. When a large part of the shower lies off the array, it is difficult to estimate how many units would be struck on an infinite array. Nevertheless, independent counts by different observers agreed well on the numbers of showers triggering $\geqslant 20$ and $\geqslant 40$ units. Above 60 units, the uncertainty is large, but not larger than the statistical errors. The numbers of showers counted range from 400 for $\geqslant 3$ fold showers to 6 for $\geqslant 60$ fold showers.

Fig. 1

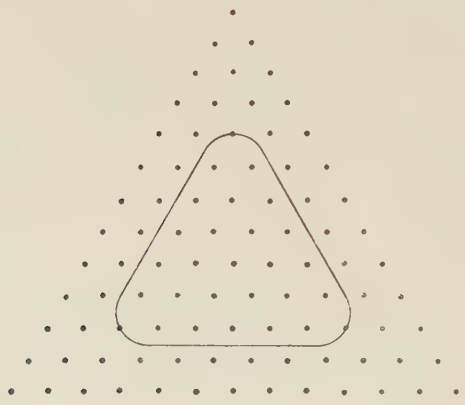

• GM units

§ 3. Determination of Size Spectrum

To convert the size spectrum in numbers of units to the spectrum in number of particles, we first calculate the probabilities $P(N, f)$ that a shower containing N particles will trigger f units. We calculate these quantities for the case of an infinite array with the spacing of our lattice, i.e. we ignore edge effects.

For this calculation, we need to know the probabilities p_i for each of the units to be triggered. If the position of the axis on the lattice is known, then the distances r_i to all the units are known, and we can use the density distribution function given in III to calculate the density at the unit for a given N, and hence the probability of triggering. To obtain the value of N in III we have assumed the validity of the Nishimura and Kamata distribution for distances less than 50 metres, and therefore for the time being, we regard N as a nominal value, and not a measured value.

We have used two methods to calculate $P(N,f)$ from the p_i. First, the value of $P(N,f)$ is the coefficient of t^f in the expansion of

$$\pi_i(p_i+q_i)^t$$

where $q_i = 1-p_i$, and i runs over all units for which p_i is not negligible. For three points on the lattice, namely on one of the lattice points, at the

centre of one of the triangular cells and at the centre of one of the sides of the cells, there is sufficient symmetry to allow computation of the coefficients up to $f = 8$, and taking into consideration the fifty units nearest to the axis. We find that the values of $P(N,f)$ vary significantly with the position of the axis only when P is very small. We have to bear in mind that in the integrals for which $P(N,f)$ is required, the values of P corresponding to small values of N are weighted heavily. However, the values of P do not vary by more than 15% for $f = 3$ and by smaller amounts for $f > 3$, and we are justified in taking the mean values of $P(N,f)$. This is confirmed by the measurements described later. Second, for $f > 8$, we have considered only showers whose axes fall on a lattice point, and used a Monte Carlo method to determine the numbers of units triggered by showers of different N. From this data, we can determine $P(N,f)$.

From these values, we can also determine $P(N, \geqslant f)$ the probability that a shower containing N particles should trigger at least f units.

We assume for simplicity a spectrum of the form

$$J(N)\,dN = kN^{-\gamma-1}\,dN.$$

Then the rate per unit area of showers triggering at least f units is

$$R(\geqslant f) = \int_0^\infty J(N)\,dN.P(N, \geqslant f)$$

or

$$R(\geqslant f) = k\int_{-\infty}^{\infty} \exp(-w\gamma)P(w, \geqslant f)\,dw, \quad \text{where } w = \ln N.$$

If we take a value γ_0, known nearly to satisfy the data and put $\gamma = \gamma_0 + \delta_\gamma$, we may write

$$R(\geqslant f) = k\left\{\int_{-\infty}^{\infty} \exp(-w\gamma_0)P(w, \geqslant f)\,dw - \delta_\gamma\int_{-\infty}^{\infty} w\exp(-w\gamma)P(w, \geqslant f)\,dw + 0(\delta_\gamma)^2\right\}.$$

Both these integrals can be evaluated, and the different values of f from the experimental observations give simultaneous equations which can be solved by a least squares method for k and δ_γ. We then calculate γ from $\gamma = \gamma_0 + \delta_\gamma$.

The spectrum calculated in this way refers to the number of showers striking the ground. It will be shown later (paper VI) that the solid angle for our apparatus is 0·5 radians. We can then calculate the spectrum per unit solid angle, and obtain

$$J(\geqslant N) = \int_N^\infty J(N)\,dN = 9{\cdot}5 \times 10^{-5}(10^6/N)^{1{\cdot}88\pm0{\cdot}15}\,\mathrm{m^{-2}\,hr^{-1}\,ster^{-1}}.$$

It is of interest to see how showers of different sizes contribute to the events which go into the various categories, i.e. the resolving power of the apparatus. In fig. 2 we have drawn dashed curves which show the resolution for the different categories. It will be seen that the resolution improves as the number of units struck increases. The resolution curves

are markedly asymmetrical, and in table 1 we give values of the mean of N, and N_{10}, for which 10% of the showers contain fewer particles than N_{10}.

The points marked on fig. 2 show the rates at which showers of different sizes are recorded. These are plotted at values of N given by

$$9{\cdot}5\times10^{-5}(10^6/N)^{1{\cdot}88}=\int_0^\infty J(N)P(N,\geqslant f)\,dN.$$

Fig. 2

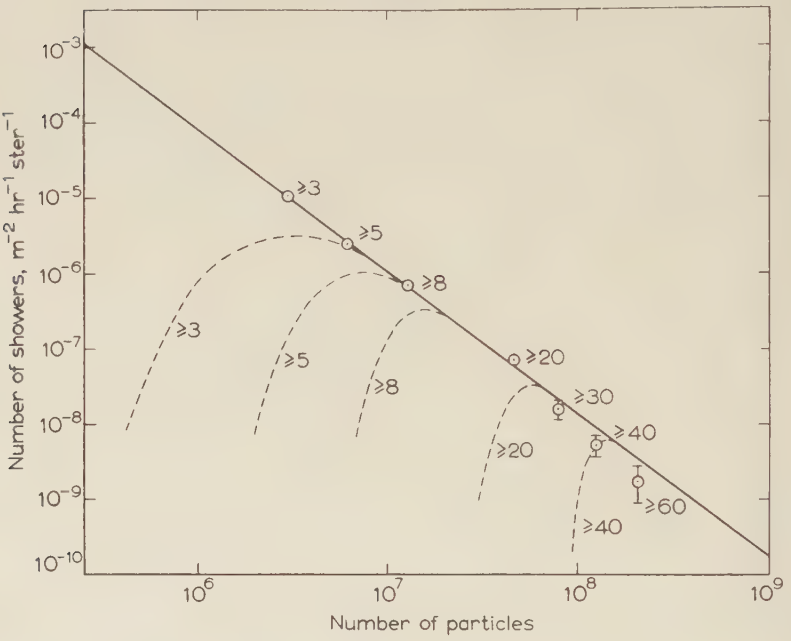

Table 1

	⩾3	⩾5	⩾8	⩾20	⩾40
$\bar{N}$	$5{\cdot}5\times10^6$	$1{\cdot}2\times10^7$	$2{\cdot}7\times10^7$	$1{\cdot}0\times10^8$	$2{\cdot}8\times10^8$
N_{median}	$3{\cdot}9\times10^6$	$9{\cdot}5\times10^6$	$1{\cdot}8\times10^7$	$6{\cdot}8\times10^7$	$1{\cdot}7\times10^8$
N_{10}	$1{\cdot}7\times10^6$	$4{\cdot}7\times10^6$	$1{\cdot}0\times10^7$	$4{\cdot}5\times10^7$	$1{\cdot}2\times10^8$
$\bar{N}_{\text{measured}}$	$5{\cdot}3\times10^6$	$1{\cdot}1\times10^7$	$2{\cdot}2\times10^7$	$4{\cdot}6\times10^7$	—

This is the value of N at which an ideal apparatus, i.e. one with infinite resolving power would count showers at the same rate as the practical apparatus. The agreement of the ordinate with the value given by the line shows that the analysis is satisfactory, and that the assumption of a power law spectrum adequately accounts for the observations.

§ 4. The Measurement of Numbers of Particles

The average number of particles in showers belonging to a particular size group has also been determined in the following way:

Let showers with N, $N+dN$ particles be recorded in this group by the array at a rate $f(N)dN$ per unit area. The average number of particles in this size group is then given by

$$N = \frac{\int_0^\infty \int_0^\infty 2\pi r\, dr \rho(r, N) f(N)\, dN}{\int_0^\infty f(N)\, dN}$$

$$= \frac{1}{P} \int_0^\infty \int_0^\infty 2\pi r\, dr \rho(r, N) f(N)\, dN \quad . \quad . \quad . \quad . \quad . \quad (1)$$

where P is the rate of detected showers in this size group and $\rho(r, N)$ is the density of particles.

The rate at which i detectors, each having an area S, will discharge in coincidence with showers in this group, is

$$R_i = \int_0^\infty \int_0^\infty f(N)\, dN \,.\, 2\pi r\, dr \{1 - \exp[-\rho(r, N)S]\}^i. \quad . \quad . \quad (2)$$

Using the identity

$$y = \sum_1^\infty \frac{1}{i} (1 - e^{-y})^i$$

eqn. (1) may be written

$$S\bar{N}P = \sum_{i=1}^{\infty} \left\{ \frac{1}{i} \int_0^\infty \int_0^\infty f(N)\, dN \,.\, 2\pi r\, dr [1 - \exp\{-\rho(r, N)S\}]^i \right\}$$

$$= \sum_{i=1}^{\infty} \frac{1}{i} R_i.$$

Therefore

$$\bar{N} = \frac{1}{SP} \left(\sum_{i=1}^{\infty} \frac{1}{i} R_i \right). \quad . \quad . \quad . \quad . \quad . \quad . \quad . \quad (3)$$

For each size group $\bar{N}$ has been determined by recording R_i from six G.M. counters, area 20 cm². The figures obtained are in the fourth row in table 1, where they can be compared with $\bar{N}$ obtained by using the equation

$$\bar{N}(\geqslant f) = \frac{\int_0^\infty J(N) P(N, \geqslant f) N\, dN}{\int_0^\infty J(N) P(N, \geqslant f)\, dN}.$$

It should be noted that in this measurement, apart from the requirement that the sum (3) should converge, no assumption has been made about the radial distribution of the showers. However, we have assumed that $f(N)$ is independent of position on the array. This is equivalent to the assumption that the $P(N,f)$ are independent of position as discussed

in § 3. If $f(N)$ varies with position, R_i will be a function of position. To test this point, seven counters were placed at the points marked 1–7 in fig. 3, inside a cell near the centre of the array. Thus R_1 which contributes most to the value of $\bar{N}$ was determined for each position. The values found are given in table 2, and are seen not to vary significantly.

Later, the counters were all moved to the position marked 1 and the values for R_i obtained are given in table 3. It can be seen that the convergence is satisfactory.

Fig. 3

The errors in this method of determination can be estimated by the following considerations. The method consists in sampling the showers at different distances from the core. At large distances, the number of samples is large, and the density well determined. Moreover, the contribution to the total number of particles in the shower from large distances is small, so that the error introduced into the total is small. At short distances on the other hand, the number of samples is small, the density large, and not well determined by the six small counters, and the contribution to the total by particles from this region may be large. Thus for the $\geqslant 3$ fold showers, the measurement of density becomes poor inside 12 metres from the core. This region is sampled about 15 times during the experiment, and contains about 12% of the particles. The contribution to the error from this region is estimated to be about 8%, and the total error on the number of particles should be about 10%. Similarly we find for $\geqslant 8$ fold showers an error of about 20%. For $\geqslant 20$ fold showers, the region less than about 80 metres from the core triggers all the counters on nearly every occasion. This region contains more than half the particles

in the shower. For these showers the method gives a low value for the number of particles, with a very large error.

A further under-estimate of the number of particles in $\geqslant 20$ fold showers arises, since more than 5% of the showers falling near the boundary of the array discharge at least one of the small units but are not recorded as $\geqslant 20$ fold showers.

Table 2

Counter position	1	2	3	4	5	6	7
Number of counts	31	29	29	28	23	29	30

Table 3

Size group	R_1	R_2	R_3	R_4	R_5	R_6	$\sum \frac{1}{i} R_i$
$\geqslant 3$	95·2	27·9	18·0	14·8	13·1	11·5	123·5
$\geqslant 5$	44·3	16·4	11·5	8·2	8·2	6·6	61·2
$\geqslant 8$	21·3	9·8	6·6	4·9	3·3	3·3	30·9
$\geqslant 20$	4·2	2·6	2·2	1·9	1·7	1·1	7·2

§ 5. Conclusion

We have measured the size spectrum of air showers containing between 10^6 and 10^8 particles. We find

$$J(\geqslant N) = 9{\cdot}5 \times 10^{-5}(10^6/N)^{1{\cdot}88\pm0{\cdot}15}\ \mathrm{m^{-2}\,hr^{-1}\,ster^{-1}}.$$

This result may be compared with the M.I.T. experiment (Clark *et al.* 1957) who find

$$J(\geqslant N) = 8{\cdot}2 \times 10^{-5}(10^6/N)^{1{\cdot}85\pm0{\cdot}15}\ \mathrm{m^{-2}\,hr^{-1}\,ster^{-1}}.$$

An independent measurement of the number of particles in the showers gives good agreement with these figures.

Acknowledgments

We wish to express our thanks to Mr. K. W. Morton and Mr. J. E. Hailstone for assistance with the Monte Carlo Calculation, to Mrs. S. Norris for carrying out the numerical computation, and to Mr. A. G. Parham and Mr. C. Sherwood for running the apparatus.

References

Clark, G., Earl, J., Kraushaar, W., Linsley, J., Rossi, B., and Scherb, F., 1957, *Nature, Lond.*, **180**, 406.

Cranshaw, T. E., and Galbraith, W., 1957, *Phil. Mag.*, **2**, 797.

Cranshaw, T. E., Galbraith, W., and Porter, N. A., 1957, *Phil. Mag.*, **2**, 891.

Plastic Deformation of Nickel Single Crystals at Low Temperatures†

By Peter Haasen
Institute for the Study of Metals, University of Chicago, U.S.A., and Max-Planck-Institut fuer Metallforschung, Stuttgart, Germany

[Received January 1, 1958]

Abstract

Single crystals of nickel (purities 99·98% and 99·4%) have been deformed in tension at various temperatures between 4·2°K and 300°K. Shear stress–shear strain relations have been determined as well as the reversible change of flow stress with temperature. The work-hardening parameters obtained are discussed in terms of dislocation theory that has been developed mainly on the basis of data on Al and Cu. From the temperature dependence of the stress at the beginning of dynamical recovery the activation energy of cross-slip is estimated to be slightly lower than that of copper, implying a somewhat higher stacking fault energy.

The advantages of the temperature change method for an investigation of the flow stress are pointed out following a theoretical analysis of the relation between this method and that of the work-hardening parameters. The present results on nickel confirm this relation.

Metallographic and x-ray evidence has been obtained in favour of deformation twinning in nickel at 4·2°K and 20°K although no drop in load has been observed of the kind found in copper. Serrations in the recorded load-extension curves indicate discontinuous flow at the lowest temperatures.

§ 1. Introduction

An understanding of the plasticity of metals with the help of dislocation theory seems to be possible so far only in relatively simple cases, such as single crystals of close-packed hexagonal and face-centred cubic metals. For the latter, the situation at low temperatures is particularly promising since, for example, three different mechanisms of work-hardening manifest themselves in separate stages of the stress–strain curve, as measured in a constant strain rate tensile test, of a single crystal (fig. 1). Following the Stuttgart school (Diehl 1956 a, Seeger *et al.* 1957) the three stages can be characterized as follows: Stage I will be called the region of *easy glide* (Andrade and Henderson 1951). Here a small rate of work-hardening suggests that most of the dislocations produced during deformation leave the crystal through the surface. Stage II, the *rapid hardening* range, is thought to be characterized by the formation of piled-up groups of dislocations behind Lomer–Cottrell dislocations. At high stresses, some of the slip dislocations become able to by-pass these obstacles

† Communicated by the Author.

('cross-slip'). This process of *dynamical recovery* reduces the rate of work-hardening and leads to stage III of the stress–strain curve.

Most of the earlier work on plastic deformation of face-centred cubic single crystals was done with aluminium at room temperature where, unfortunately, stage III sets in immediately (after a very short stage I). At 78°K, however, Al has been shown (Staubwasser 1954, Cottrell and Stokes 1955, Jaoul 1957) to exhibit stress–strain curves of the type drawn in fig. 1†. This prototype has been established mainly by tensile tests of copper crystals at 300°K and below (Diehl 1956a, Blewitt 1953, Blewitt *et al.* 1955, Adams and Cottrell 1955, Rebstock 1957, Berner 1957, Andrade and Aboav 1957). Other experimental evidence, especially electron-microscopic observations of slip lines (Diehl *et al.* 1955, Mader

Fig. 1

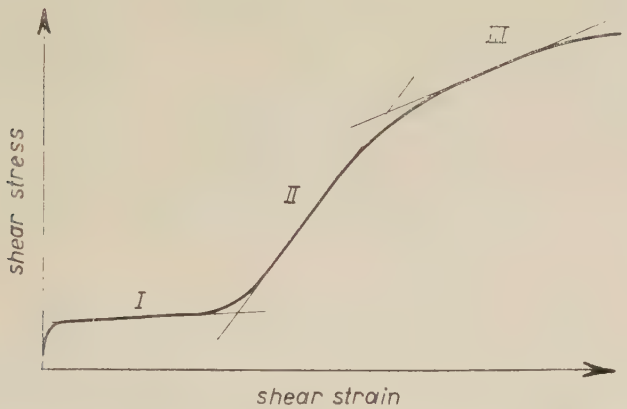

Schematic shear stress–shear strain curve of face-centred cubic single crystal at low temperatures.

1957), has helped to connect certain dislocation processes with the various stages of the stress–strain curve, as indicated above. There is, however, a great need for experimental data on work-hardening 'parameters' — characterizing quantitatively each of the three stages — obtained from a single set of crystals, at different temperatures. It was thought that a third face-centred cubic metal such as nickel would offer the necessary check on theories developed on the basis of work on Cu and Al. As will be seen below, the extent of the three stages changes strikingly with temperature between 300°K and 20°K, even for a high melting point metal such as nickel.

The measured values of the parameters are given in § 3, and in § 5 some of the measurements, especially on dynamical recovery, are evaluated in terms of existing dislocation theory. In addition to the temperature

† There are also some published data on the first two stages of work-hardening of Al single crystals at 4·2°K (Sosin and Koehler 1956, Noggle and Koehler 1957).

variation it is now well known from work on Al (e.g. Staubwasser 1954, Lange and Lücke 1952, 1953, Davis *et al.* 1957) and Cu (Diehl 1956a, Rosi 1954, Paterson 1955) that the *shear* stress *shear* strain curve still depends on the orientation of the crystal with respect to the tensile direction. For this reason crystals of one orientation were investigated at different temperatures as well as different orientations at a given temperature.

The influence of crystal orientation makes it difficult to evaluate previous data by Andrade and Henderson (1951) on work-hardening of Ni. These authors measured stress–strain curves of four crystals at 90°, 300°, 508° and 833°K by a stepwise loading technique (99·9% Ni, unknown orientation).

In addition to the type of analysis of work-hardening described above, Cottrell and co-workers (Cottrell and Stokes 1955, Adams and Cottrell 1955) have introduced a method of separating the flow stress of a cold-worked crystal into two contributions, one due to the dislocation structure and another due to the dislocation mobility. They measured the reversible change in flow stress $\Delta\tau$ connected with a change in temperature $(T_1 - T_2)$ at a given strain. $\Delta\tau$ determines the change in dislocation mobility, or dislocation friction, with temperature in a given dislocation structure. We will give our results on $\Delta\tau(T_2)$ for nickel in § 4. In § 5 we will discuss the relation between the two methods of analysis of work-hardening and their results.

In recent papers Blewitt (1953), Blewitt *et al.* (1955, 1957) established evidence for discontinuous slip and deformation twinning in copper single crystals at 4°K and 78°K under very high stresses. We have searched for such a phenomenon in Ni and Cu at 20°K (and in one example, using Blewitt's equipment, also at 4°K). The results of these tests are given in § 6.

§ 2. Experimental Procedures

2.1. *Specimen Preparation*

Single crystals of nickel were grown from the melt under high vacuum in pure Alumina crucibles by the Bridgman technique. Most of the crystals were of Johnson Matthey J.M. 890 nickel, nominal purity 99·999%. Spectroscopic analysis at the Chicago Institute before and after crystal fabrication indicated a purity greater than 99·98%. A gas analysis by vacuum fusion after different heat treatments of the crystals showed about 10^{-5}% N_2, 5×10^{-5}% H_2 and 10^{-3}% O_2. A micro-carbon analysis gave less than 10^{-3}% C for vacuum annealed crystals (about 3×10^{-2}% C for the hydrogen pre-annealed crystals). Some crystals, marked 'c' in front of the number, were of commercial purity, 99·4% Ni, with Co and Fe as major impurities.

The dimensions of the as-grown single crystal wires were as follows: diameter 0·088 in. and maximum length 8 in. After growth most of the crystals adhered to the crucible walls by a thin blue layer of what is believed

to be a mixed Ni–Al oxide. The best way of removing the crucibles was with the help of a micro-sandblasting device, using Al_2O_3 powder. The thin jet cuts the brittle crucible into small pieces which fall off without damaging the soft nickel crystal. Following this the crystals were cleaned in HNO_3 and were cut into 2·8 in. long pieces by means of an acid saw as described by Maddin (1950). In this way a number of equi-oriented specimens grown under the same conditions could be investigated.

After preparation the crystals were usually annealed *in vacuo* for 12 hours at 900°C. The mechanical behaviour of some as-grown crystals and of some crystals that were annealed for 12 hours in wet or dry hydrogen before the vacuum anneal was compared with that of vacuum annealed crystals of the same orientation. As will be seen in § 3, the as-grown crystals showed a higher critical shear stress τ_0, and the hydrogen pre-annealed ones a lower τ_0 than the standard vacuum annealed crystals.

Fig. 2

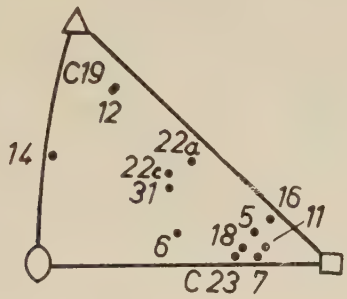

Stereographic plot of the orientation of the tensile axes of nickel single crystals.

After annealing, the x-ray photographs showed sharp Laue spots. The orientations of the wire axes were determined by a simple rotating crystal method (Schmid and Boas 1935); they are plotted in the stereographic unit triangle in fig. 2. The crystals were subsequently soldered, using a micro-flame, into steel grips, the ball-shaped ends of which fitted into the holders (L in fig. 3) of the tensile machine. At first crystals to be tested at low stresses were soft soldered. Later a special low melting silver solder was used with little effect on the critical shear stress. A more complex holding device employing a piece of piano wire for better initial alignment was also tried and did not have much effect on the critical shear stress. Finally, the gripped crystals were chemically polished.

2.2. *Method of Deformation*

The crystals were strained in a Tinius Olsen tensile testing machine (employing the ranges 100, 150, 200, 1000 lb.) which had been adapted for use at temperatures down to 20°K. The low temperature unit is drawn in fig. 3. In this arrangement the crystal is pulled between the stainless steel rod J and the base N which is kept at a fixed distance from the top

Fig. 3

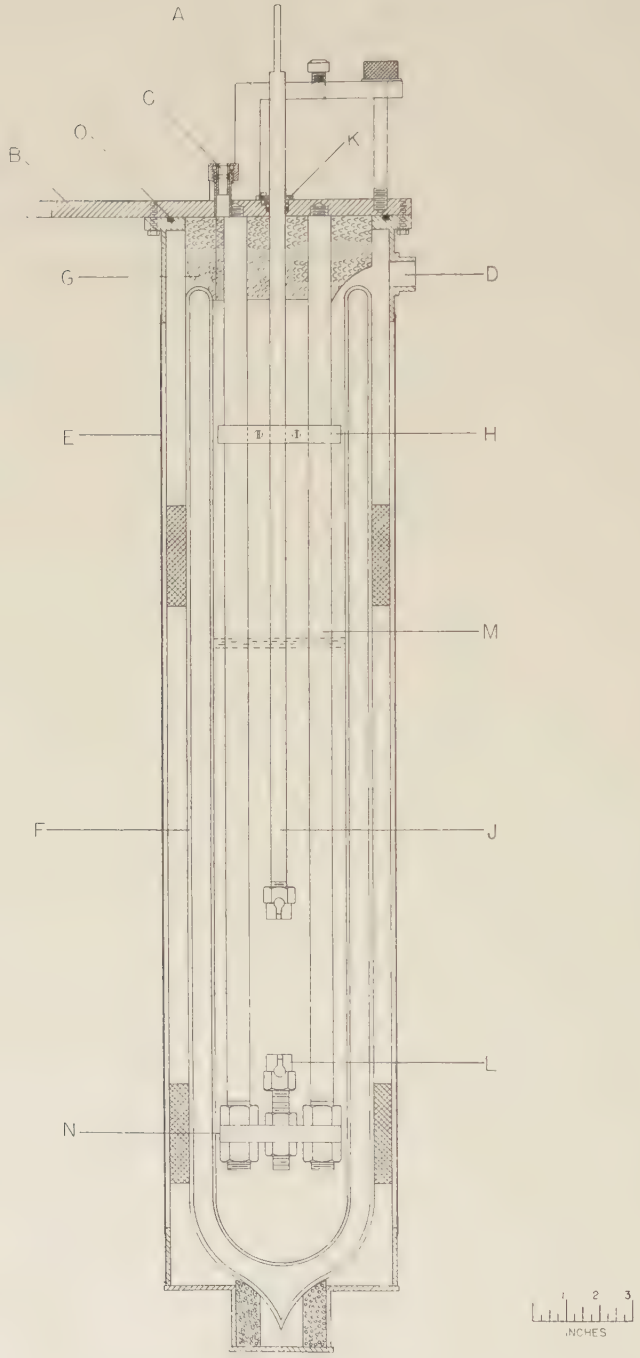

Low temperature extensometer unit (described in the text).

plate B by four stainless steel rods M. The pull rod J is connected to the pendulum system of the machine, and the top plate B to the moving cross-head, by means of the clamps A. A Dewar flask F surrounds the assembly. It is fixed to the top plate B by a brass case E having slot windows. The case can be made gas-tight for the tests under liquid hydrogen by means of Teflon O-ring seals O, C and K and by connecting it to an exhaust line at D. A piece of styrofoam G and an outer N_2 gas jet prevent the moving seal K from freezing after liquid hydrogen is transferred into the Dewar through C. A filling of 6 litres of liquid hydrogen was sufficient for an hour's run. Further tests were made using liquid nitrogen (78°K), a solid CO_2-trichlorethylene mixture ($\sim$200°K), and at room temperature.

The gauge length of the tensile specimen measured about 2 in., and the cross-head speed was kept constant at 0·05 in./min giving a strain rate between 10^{-4} and 10^{-5} sec depending somewhat on the load range because of the softness of the machine. Strain was measured by a linear transformer between B and J, fig. 3, and was continually recorded against load. The strain measurement has been checked by microscopic observation of the distance of marks on the crystal before and after deformation.

§ 3. Stress–Strain Curves and Work-Hardening Parameters

From the recorded load–extension curves shear stress–shear strain curves were computed by using the well-known relations (Schmid and Boas 1935). The initial orientation determines the position of the tensile axis in the dodecahedral plane through [111] and [100] in the stereographic triangle where double slip sets in. (Not much overshooting has been observed (Osswald 1933).) From thereon the vonGöler–Sachs (1927) method for double glide has been used to compute shear stress and shear strain. It gives a considerably higher work-hardening rate than the application of the single slip formula which is here unjustified†. Typical stress–strain curves of nickel at different temperatures and for different orientations are given in figs. 4 to 10. The appearance of some of the curves is somewhat complicated by the temperature changes introduced to determine the reversible change of flow stress. Fortunately, after a few percent strain past the point of the temperature change the work-hardening parameters settled down to the values characteristic of the new temperature – except during stage I (discussed below). The parameters defined in fig. 11 have been obtained from the stress–strain curves. The results will be discussed together below in terms of certain *common* parameters evaluated from *all* crystals. In this way the variation with temperature and orientation can be best recognized and separated from the individual scatter between the crystals‡.

† Apparently, the curves given by Andrade and Henderson (1951) and Andrade and Aboav (1957) have been calculated for single slip throughout.

‡ Also, due to the temperature changes, not all the parameters could be taken from every crystal.

Fig. 4

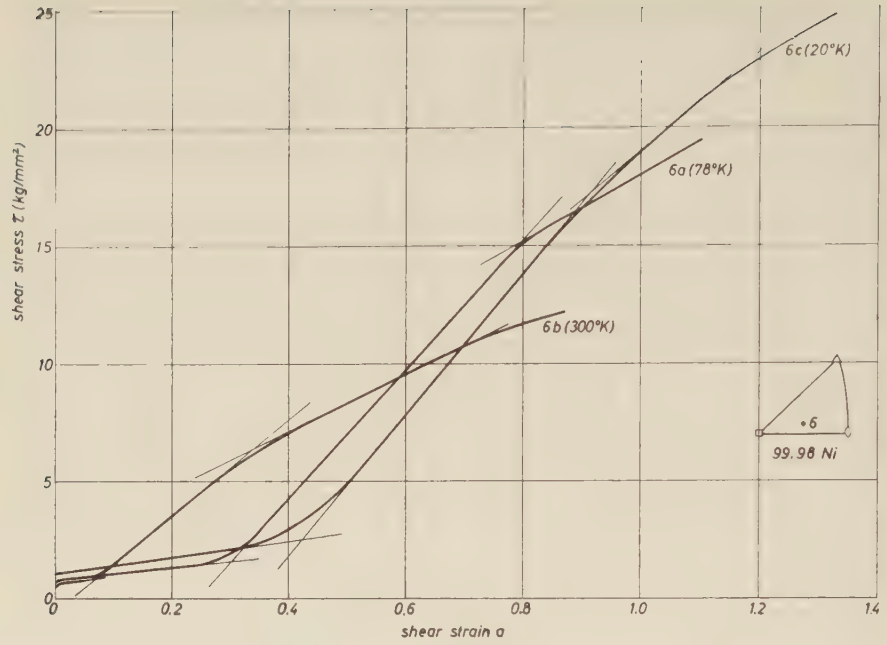

Shear stress–shear strain curves of high purity nickel crystal 6.

Fig. 5

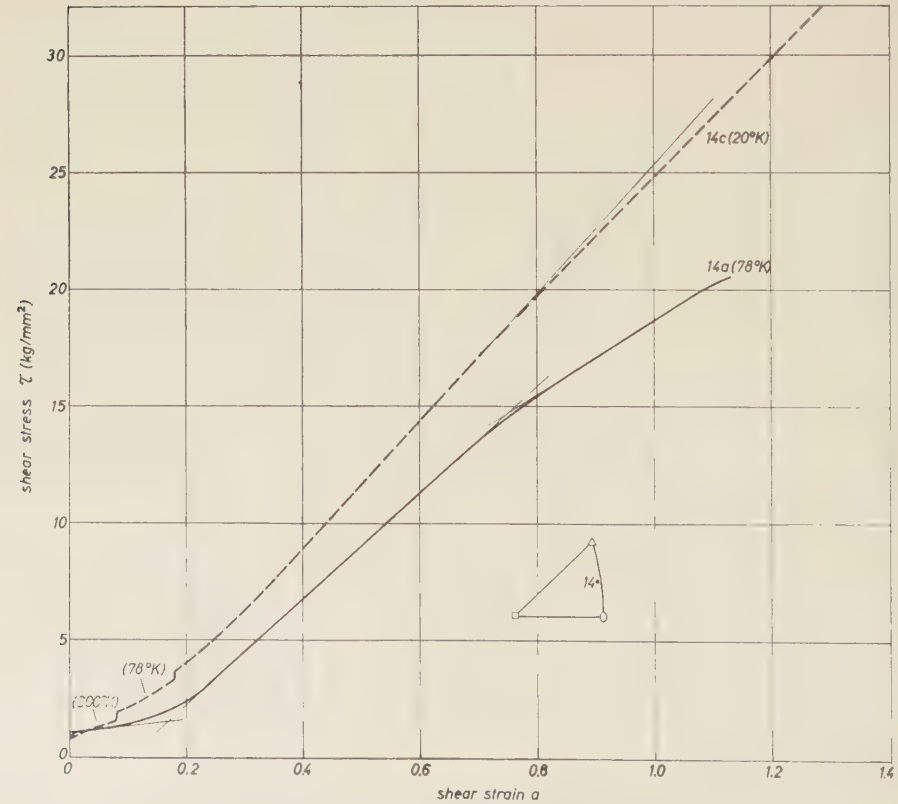

Shear stress–shear strain curves of high purity nickel crystal 14.

Fig. 6

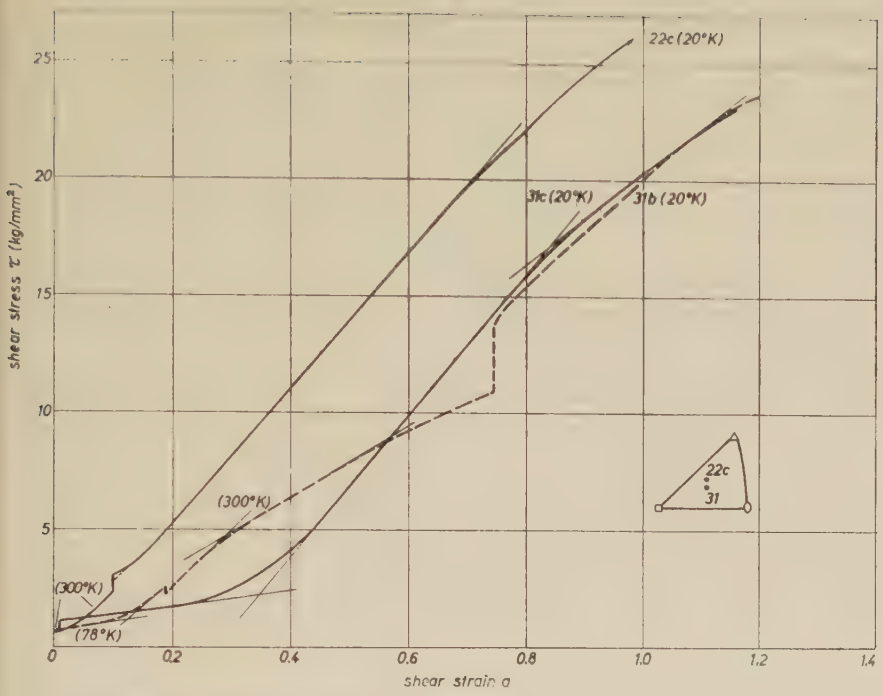

Shear stress–shear strain curves of high purity nickel crystals 22c and 31.

Fig. 7

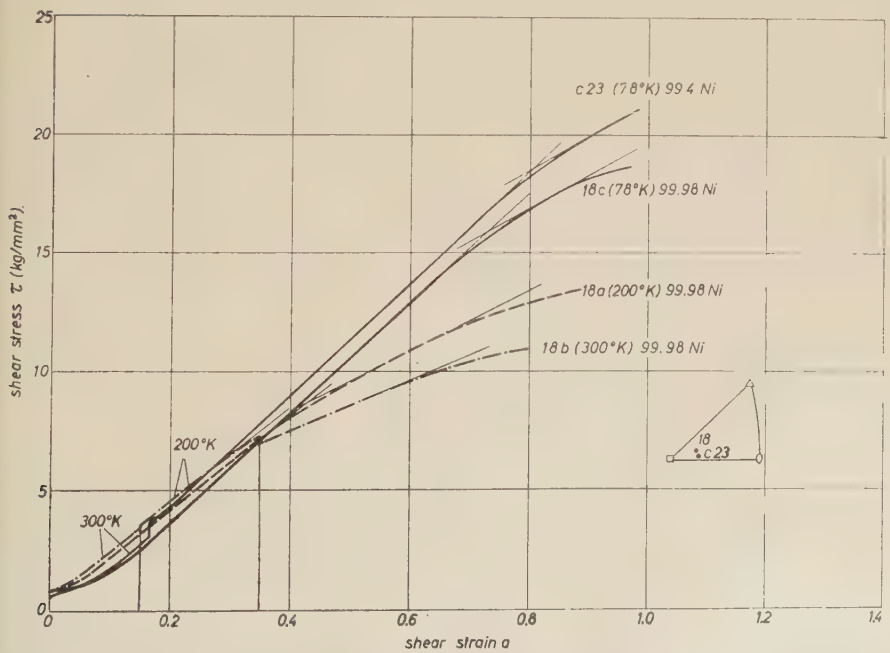

Shear stress–shear strain curves of high purity nickel crystal 18 and of commercial nickel crystal c23.

Fig. 8

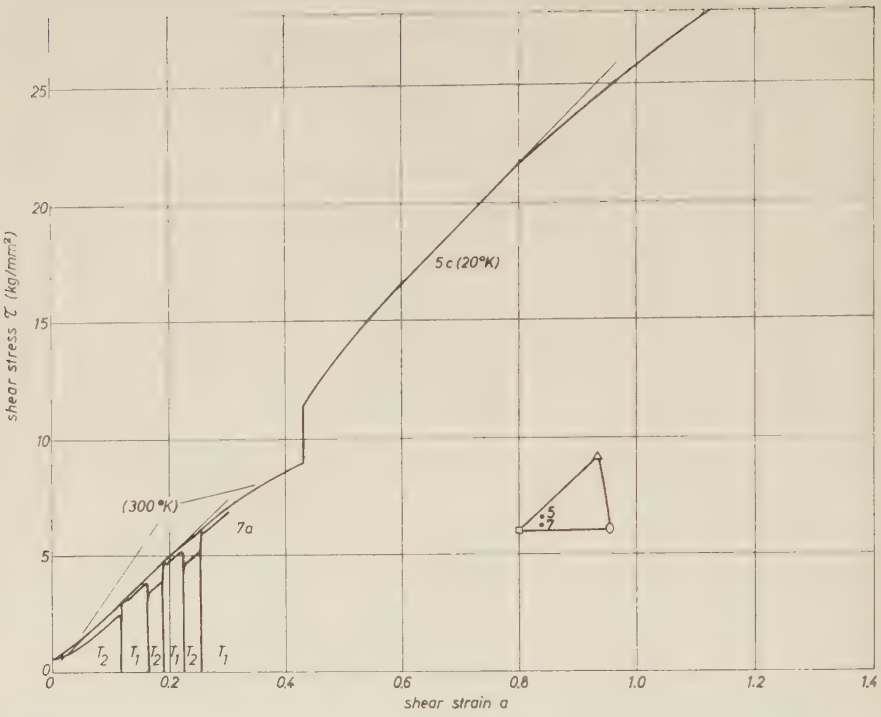

Shear stress–shear strain curves of high purity nickel crystals 5 and 7.

Fig. 9

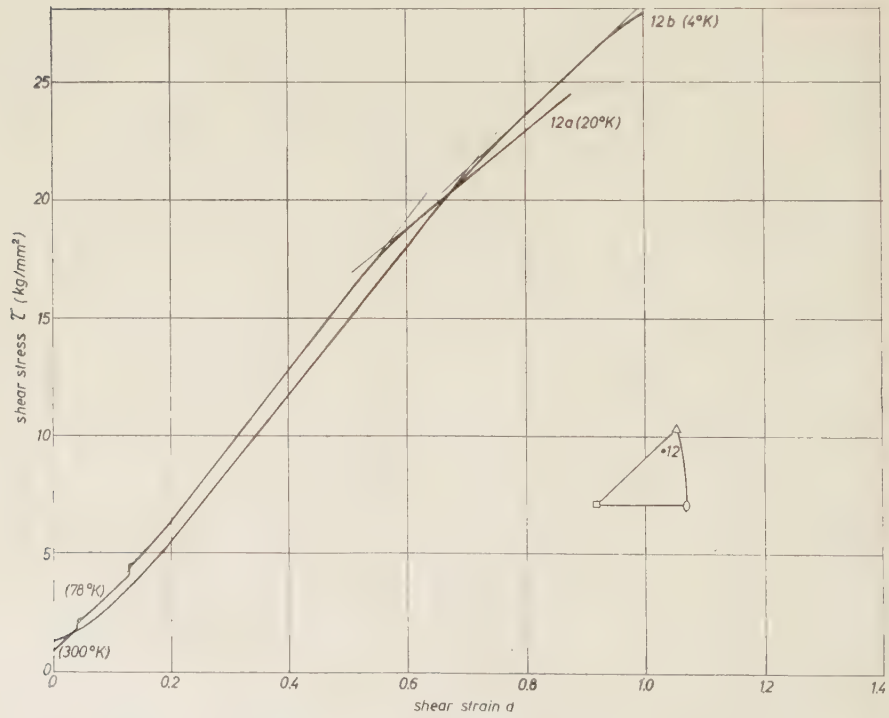

Shear stress–shear strain curves of high purity nickel crystal 12.

Fig. 10

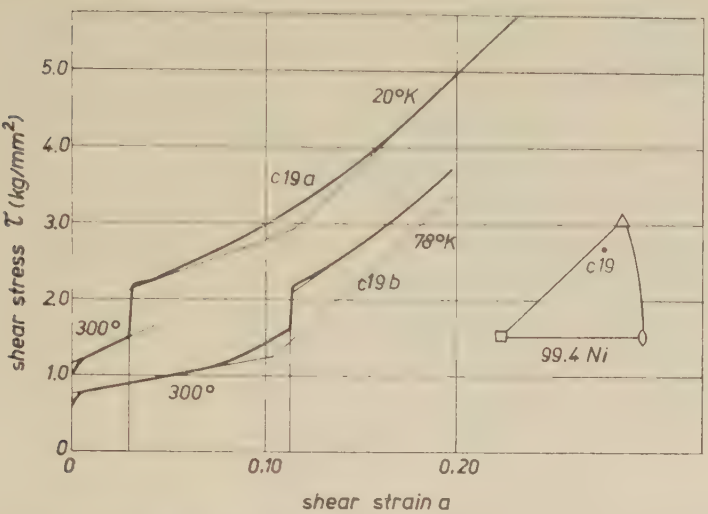

Shear stress–shear strain curves of commercial nickel crystal c19.

Fig. 11

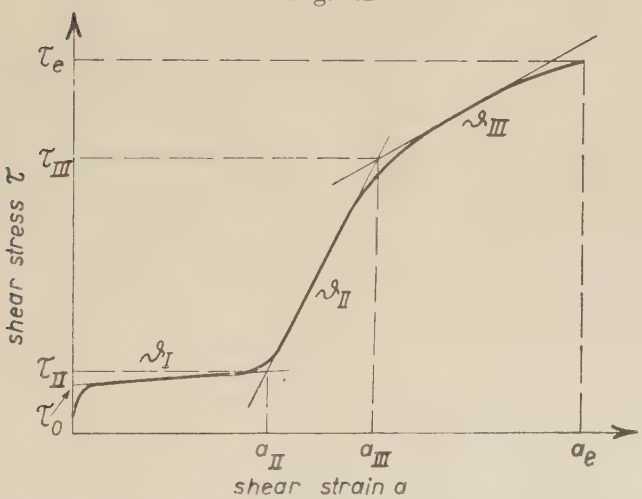

Definition of the work-hardening parameters.

3.1. *The Critical Shear Stress* τ_0

This is defined by the intersection of the extrapolated linear easy glide region with the stress axis. Table 1 gives the measured values. An increase of τ_0 at lower temperatures is evident, but no orientation dependence (see also Diehl 1956 a), within the considerable scatter of this quantity. A better way to determine the temperature variation of τ_0 for one crystal is by studying temperature changes during stage I,

after a few per cent strain. The results described in § 4 indicate a value of $\Delta\tau_0 = 150\,\mathrm{g/mm^2}$ between 78°K and 300°K, and $\Delta\tau_0 = 350\,\mathrm{g/mm^2}$ between 20°K and 300°K. This is consistent with the average values from table 1:

$$\tau_0 = 600\text{–}850\,\mathrm{g/mm^2} \text{ at } 300^\circ\mathrm{K},$$
$$\tau_0 = 750\text{–}850\,\mathrm{g/mm^2} \text{ at } 78^\circ\mathrm{K},$$
$$\tau_0 = 900\text{–}1100\,\mathrm{g/mm^2} \text{ at } 20^\circ\mathrm{K}.$$

Special attention is called to the hydrogen pre-annealed crystals 5a and 7b which have critical shear stresses about $230\,\mathrm{g/mm^2}$ lower than the standard vacuum annealed crystals. As-grown crystals (5b, 7c and c 19a) show up to 50% higher τ_0 values than the vacuum annealed crystals. No particular difference is visible between 99·4 and 99·98 nickel regarding τ_0 at 300°K.

Table 1. τ_0 (kg/mm²)

Crystal No.	Remarks	Parameter Values at Temperature			
		20°K	78°K	200°K	300°K
6		1·10	0·80		0·65
14	*mishandled		*(1·05)		0·85 0·85
31			0·75		0·65
22a		0·90			
22c					0·60
18			0·85	0·85	0·75
7a					0·57
7b	pre-annealed in H_2				0·33
7c	as grown				0·75
11					?
5a	pre-annealed in H_2				0·47
5b	as grown				1·05
5c					0·70
16		1·05			
12	4·2°K : 1·15				0·80
c23					0·60
c19 a	as grown				1·15
c19 b					0·75

Andrade and Henderson (1951) give $\tau_0 = 1040\,\mathrm{g/mm^2}$ at 300°K, $\tau_0 = 1360\,\mathrm{g/mm^2}$ at 93°K for their 99·9 nickel. Osswald (1933) measured an average $\tau_0 = 580\,\mathrm{g/mm^2}$ on four 99·7% nickel crystals at room temperature.

3.2. *The Work-Hardening Rate ϑ_I during Easy Glide*

This has been compiled in table 2. There seems to be a slight decrease of ϑ_I on changing the temperature from 300°K to 78°K and 20°K within the uncertainty of the scatter to which ϑ_I is particularly susceptible

due to growth conditions (Diehl 1956 b). ϑ_I increases strongly (from 3 to 12 kg/mm²) for unfavourable orientations where other slip systems come into play early. As will be shown below, the extent of stage I in such cases is very small so that ϑ_I might be influenced by the transition into stage II. The relatively small ϑ_I of the hydrogen pre-annealed and commercially pure nickel crystals, especially the unfavourably oriented crystal c 19, should be noted. We do not know the reason for the abnormal easy glide parameters of the crystals pre-annealed in hydrogen instead of vacuum (see also Cupp and Chalmers 1954). Hydrogen was shown not to be responsible for the yield phenomenon observed (Haasen and Kelly 1957).

Table 2. ϑ_I (kg/mm²)

Crystal No.	Remarks	Parameter Values at Temperature			
		20°K	78°K	200°K	300°K
6		3·25	2·75		4·0
14			3·0		7·5
31		3·6	5·5 4·5		
22a		6·2			
22c					10·0
18			5·0	7·5	
7a					12·0
7b	pre-annealed in H_2				7·9
7c	as grown				8·5
11					11·5 11·0
5a	pre-annealed in H_2				7·3
5b	as grown				
5c					
16					
12	4·2°K : 12·5				
c23					8·5
c19b					5·0

3.3. *The Extent of Easy Glide* a_{II} (*Table* 3)

This is strongly temperature dependent as already noted by Andrade and Henderson (1951). In our crystals a_{II} increases from 7% at 300°K to 42% at 20°K for a favourable orientation. For unfavourable orientations a_{II} is much smaller and varies less with temperature. Commercial nickel shows a different behaviour. Here a_{II} is relatively large even for the unfavourably oriented crystal c 19 (fig. 10) and seems to be independent of temperature.

Figure 12 summarizes $a_{II}(T)$ values for pure and commercial nickel. When easy glide begins at a higher temperature T_2 and continues at a lower temperature T_1 the large a_{II} associated with T_1 is obtained only if the glide at T_2 had not yet touched the transition into stage II (compare crystal 12 a (fig. 9), 14 c (fig. 5), 22 c (fig. 6) with 31 b (fig. 6), c 19 a (fig. 10)). Thus once rapid hardening had started at one temperature the crystal was

never able to continue easy glide at any other temperature. This behaviour differs from that at the transition from stage II into stage III where crystals pulled into stage III at a higher temperature came back into

Table 3. a_{II}

Crystal No.	Remarks	Parameter Values at Temperature			
		20°K	78°K	200°K	300°K
6		0·42	0·30		0·075
14			0·17		
31		0·35	0·13 (0·10)		
22a		0·15			
22c					0·035
18			0·095	0·05	
7a					0·05
7b	pre-annealed in H_2				0·075
7c	as grown				0·055
11					?
5a	pre-annealed in H_2				0·045
5b	as grown				(0·025)
5c					(0·05)
16		(0·05)			
12	4·2°K : 0·11				
c23					0·08
c19[b]					0·10
a	as grown	0·11			

Fig. 12

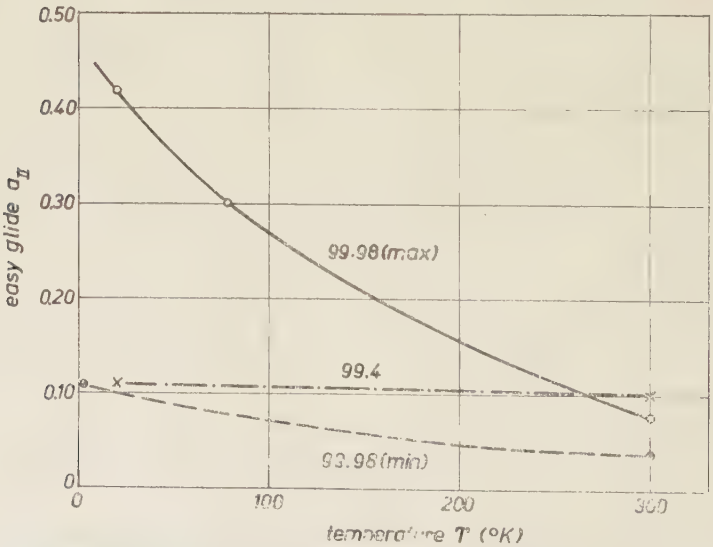

Extent of easy glide a_{II} *vs* temperature for nickel crystals of different purity oriented favourably (max) or unfavourably (min) for single slip.

stage II at a lower temperature. This difference is in agreement with the dislocation mechanisms believed to be operating in stages I and II (see § 5).

3.4. *The Stress at the Setting-in of Rapid Hardening,* τ_{II} (*Table* 4)

This follows from ϑ_I, τ_0 and a_{II} according to $\vartheta_I \approx (\tau_{II} - \tau_0)/a_{II}$. The increase of τ_{II} by a factor of 2·5 connected with a change in temperature from 300°K to 20°K for a favourable† orientation reflects the increase of a_{II} under the same conditions since ϑ_I and τ_0 are less temperature dependent. τ_{II} seems to be smaller for unfavourable orientations† at 20°K and 78°K. At 300°K, however, τ_{II} is somewhat larger for the unfavourable orientations‡. Therefore the effect of temperature on τ_{II} is reduced for these orientations as it is on a_{II}. If one considers τ_{II} and ϑ_I as primary quantities responsible for the extent a_{II} of easy glide then the temperature dependence of a_{II} is largely due to that of τ_{II} while the orientation dependence of a_{II} is mainly that of ϑ_I.

Table 4. τ_{II} (kg/mm²)

Crystal No.	Remarks	Parameter Values at Temperature			
		20°K	78°K	200°K	300°K
6		2·5	1·6		0·95
14			1·55		
31		2·3	1·3		
22a		1·8			
22c					0·95
18			1·3	1·25	
7a					1·15
7b	pre-annealed in H_2				0·90
7c	as grown				1·25
11					?
5a	pre-annealed in H_2				0·80
5b	as grown				($\leqslant$1·35)
5c					($\leqslant$1·5)
16		1·95			
12	4·2°K : 2·5				
c23					1·3
c19		(2·9) as grown			1·25

† We continue to call unfavourable orientations those near the [111]–[100] boundary of the stereographic triangle, favourable those far from it which allow considerable single slip to occur in the crystal.

‡ It has been proposed by Rosi (1954) and Garstone, Honeycombe and Greetham (1956) that $(\tau_{II}-\tau_0)$ or τ_{II}/τ_0 is a more or less orientation-independent constant quantity determining the beginning of stage II similarly to Schmid's law for τ_0. This does not hold for our crystals (neither did it in Diehl's investigation of Cu). Also, τ_{II} varies more strongly with temperature than does τ_0.

3.5. *The Slope of the Rapid Hardening Range*, ϑ_{II}

This is shown in table 5 and fig. 13. It shows a stronger temperature dependence than expected from the measurements on copper made by Blewitt (1953), Blewitt *et al.* (1955), Berner (1957) and Andrade and Aboav (1957). The dependence on orientation lies within the scatter between individual crystals. No difference between 99·98 and 99·4 nickel has been found. Taking weighted averages from table 5 and fig. 13 we consider as best values for ϑ_{II}: at 20°K, 28 kg/mm²; at 78°K, 25 kg/mm²; at 300°K, 21 kg/mm². Osswald (1933) observed for a 99·7% Ni at room temperature a value $\vartheta_{II} = 26$ kg/mm².

3.6. *The Stress at the Beginning of Dynamical Recovery*, τ_{III}

This is a very informative parameter of work-hardening. The measured† values in table 6 show that τ_{III} increases strongly at lower temperatures. No orientation dependence can be recognized. For the commercial nickel crystal c 23 τ_{III} is 20% larger than for the pure nickel crystal 18 of the same orientation. As will be discussed below, theoretical calculations predict a relation of the form $\log \tau_{III} = A - BT$ between the stress at the beginning of stage III and the temperature T of deformation. A logarithmic plot of τ_{III} against temperature does indeed give a straight line (fig. 14) with the constants being $B = 4{\cdot}4 \times 10^{-3}$, $A = 2{\cdot}98$ when τ_{III} is measured in kg/mm² and T in °K. We have also plotted τ_{III} for Cu from the data of Blewitt *et al.* (1955) (crystals nos. 304 and 305) and Berner (1957). Again the logarithmic relation holds well, the constants being $B = 4{\cdot}1 \times 10^{-3}$ and $A = 2{\cdot}48$ (Blewitt), $B = 4{\cdot}4 \times 10^{-3}$ and $A = 2{\cdot}72$ (Berner). We will use these results in § 5 to estimate the activation energy of cross-slip in Ni relative to that of Cu.

3.7. *The Work-Hardening Rate during Stage III*, ϑ_{III} (*Table* 7)

This depends on temperature in much the same manner as ϑ_{II}, the ratio $\vartheta_{III}/\vartheta_{II}$ being constant, about 0·60 for 78°K, 200°K and 300°K; there is not much dependence upon orientation. However, ϑ_{III} ϑ_{II} increases to about 0·75 at 20°K (and 4°K) with considerable scatter from crystal to crystal. The linear character of stage III is by no means as pronounced as that of stage I and stage II. The work-hardening rate drops below ϑ_{III} at the end of the stress–strain curve so that ϑ_{III} has in some cases the meaning of a tangent which intersects the stage II line at τ_{III} as defined above.

† Since stage III is not always linear τ_{III} has been defined as the stress on the stage II line where the measured curve departs by 200 g mm². τ_{III} so defined agrees with the stress at the intersection of the stage II and stage III straight lines where the latter is well developed.

Fig. 13

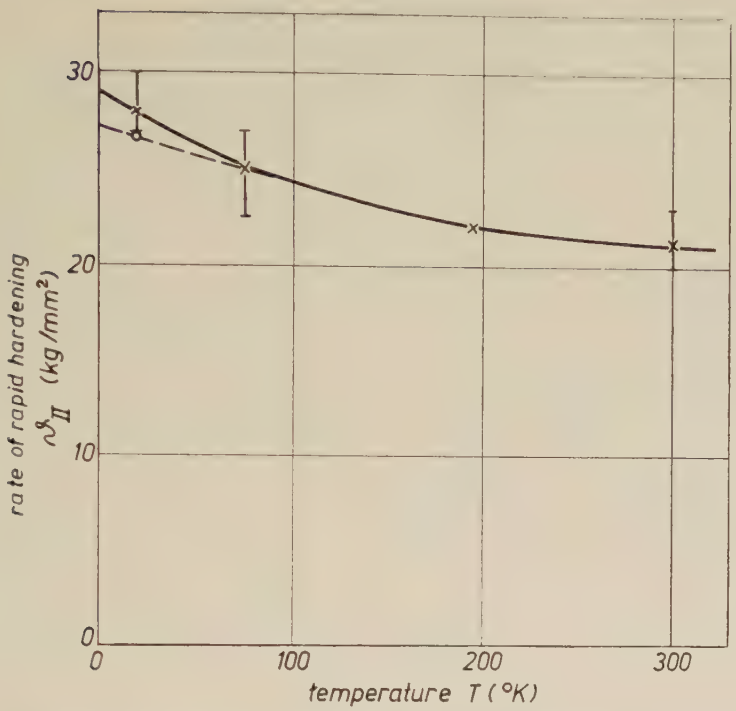

Rate ϑ_{II} of rapid hardening *vs* temperature. The crosses mark measured best values, the circle at 20°K the value expected from temperature change experiments (§ 5).

Fig. 14

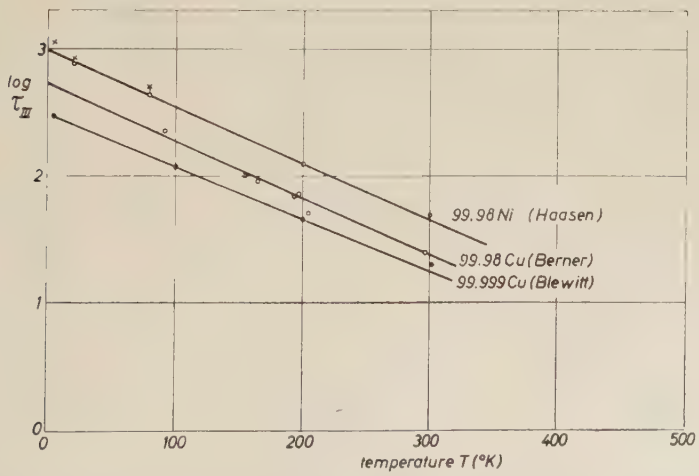

Stress τ_{III} at the beginning of dynamical recovery, measured (in kg/mm²) on nickel and copper (Blewitt *et al.* 1955, Berner 1957), plotted logarithmically *vs* temperature. (The crosses mark averages from table 6 including the high values.)

Table 5. ϑ_{II} (kg/mm²)

Crystal No.	Remarks	Parameter Values at Temperature			
		20°K	78°K	200°K	300°K
6		30·0	27·5		20·5
14		27·5	22·5		
31		30·0	22·0		23·0
22a		(28·0)			
22c		28·5			22·5
18			23·0	20·3 20·0	19·5
7a			22·0		22·0
7b	pre-annealed in H_2				(24·0)
7c	as grown		24·0		20·0
11			26·0 27·5		
5a	pre-annealed in H_2	26·5			
5b	as grown	29·5			21·5
5c		26·0			23·5
16		27·0			20·0
12	4·2°K : 31·5	32·0	25·5		22·0
c23			24·0		21·5
c19			?		

Table 6. τ_{III} (kg/mm²)

Crystal No.	Remarks	Parameter Values at Temperature			
		20°K	78°K	200°K	300°K
6		17·0	15·2		6·2
14		19·7	14·7		
31		17·0	(16·0)		4·9
22a		17·7			
22c		20·3			
18			15·4	8·7 7·6	
7a			?		
7b	pre-annealed in H_2		?		
7c	as grown		?		
11			(13·3)		
5a	pre-annealed in H_2	20·7			
5b	as grown	21·0	12·7		
5c		(22·0)			5·5
16		?			
12	4·2°K : 21·2	18·1			
c23			18·5		
c19			?		

Table 7. ϑ_{III} (kg/mm²)

Crystal No.	Remarks	Parameter Values at Temperature			
		20°K	78°K	200°K	300°K
6		21·0	14·0		12·0
14		26·0	16·0		
31		19·0	12·0		
22a		18·5			
22c		24·0			
18			14·0	12·5	11·0
7a			?		
7b	pre-annealed in H_2		?		
7c	as grown		?		
11			17·0		
5a	pre-annealed in H_2	23·5			
5b		19·5			
5c		21·5			
16		?			
12	4·2°K : 23·0	20·5			
c23			(15·0)		
c19					

Table 8. a_{III} (a_e)

Crystal No.	Remarks	Parameter Values at Temperature			
		20°K	78°K	200°K	300°K
6		0·92 (1·32)	0·80 (1·10)		0·33 (0·86)
14		0·80 (1·28)	0·75 (1·12)		
31		—(1·20)			
		0·84 (1·15)	0·72 (1·08)		0·30 (—)
22a		0·68 (0·97)			
22c		0·72 (0·98)			
18			0·70 (0·96)	0·42 (0·88)	— (0·80)
				0·35 (—)	
7a					
7b					
7c					
11			0·54 (0·90)		
5a	pre-annealed in H_2	0·74 (0·98)			
5b	as grown	0·67 (0·85)	0·40 (—)		
5c		0·81 (1·12)			0·22 (—)
16					
12	4·2°K : 0·71 (1·04)	0·57 (0·88)			
c23			0·80 (0·98)		
c19					

3.8. *The Strains at the Beginning and the End of Stage III, a_{III} and a_e Respectively*

These are given in table 8. They depend considerably on the deformation–temperature history of the crystal. Of particular importance for these quantities is the extent of easy glide a_{II} as determined by the orientation of the crystal and the temperature during the stage I deformation. We have seen (§ 3.3) that a_{II} increases strongly at low temperatures, and for favourable orientations. The orientation dependence of a_{III} and a_e is essentially that of a_{II} (see the preceding sections) and is therefore determined by the variation of ϑ_1 with orientation. Concerning the temperature influence on a_{III} and a_e a contribution besides that of a_{II} comes from $\tau_{III}(T)$. The extent of stage II as measured by $(a_{III}-a_{II})$ is about 50 to 60% for low temperatures and about 20% at 300°K for this reason. Altogether, a_{III} increases by a factor of three at low temperatures for a favourable orientation. The extent of stage III, (a_e-a_{III}), is about $40\% \pm 10\%$ at all temperatures investigated. Therefore the strain at fracture, a_e, increases from about 85% at 300°K to 130% at 20°K.

3.9. *The Stress at Fracture, τ_e*

This is given in table 9. It is independent of orientation within the scatter. Its temperature dependence is predominantly that of τ_{III} although $(\tau_e-\tau_{III})$ increases somewhat between 78°K and 20°K. The stress at fracture at 20°K is about $G/400$, where G is the shear modulus.

Table 9. τ_e (kg/mm²)

Crystal No.	Remarks	Parameter Values at Temperature			
		20°K	78°K	200°K	300°K
6		24·6	19·5		12·2
14		31·8	20·4		
31		23·7 23·0	20·8		
22a		23·0			
22c		26·0			
18			18·7	13·5	11·1
7a					
7b					
7c					
11			18·8		
5a	pre-annealed in H_2	25·5			
5b	as grown	24·5			
5c		28·0			
16					
12	4·2°K : 27·8	24·3			
c23			21·0		
c19					

§ 4. The Reversible Change of Flow Stress with Temperature

The advantage of employing the method of temperature changes during deformation has already been indicated above. It enables one to determine the change of flow stress with temperature *in a given cold-worked state*. The experimental procedure is that one deforms a crystal at a temperature T_1 up to a stress $\tau(T_1)$, unloads, changes to T_2 and resumes deformation at T_2 which starts now at a stress $\tau(T_2)$. $(\tau(T_1)-\tau(T_2))$ can thus be determined as a function of the temperature T_2 and the work-hardening (measured by $\tau(T_2)$†), T_1 being fixed at a low temperature. Typical examples of the change in the flow stress $(\tau_1-\tau_2)$ of nickel with temperature are shown in the stress–strain curves of figs. 5, 6, 7, 8, 9, 10. In order to rationalize the results of such experiments Cottrell and Stokes (1955) and Adams and Cottrell (1955) in previous investigations on Al and Cu have plotted the flow stress ratio $\tau(T_2)/\tau(T_1)=1-(\tau(T_1)-\tau(T_2))/\tau(T_1)$ as a function of T_2 for temperature changes made at large strains $(T_1<T_2)$. In this way they take advantage of two observations: (i) that τ_2/τ_1 becomes independent of the strain a for $a\geqslant 10$-15%, which is in stage III at the temperatures T_2 they used, and (ii) that the stress ratios can be determined by stepwise temperature changes according to the relation $\tau_2/\tau_1=(\tau_2/\tau_3)(\tau_3/\tau_1)$. Since they found that the cold-worked state produced at the low temperature was unstable at high temperatures for large strains ("work-softening") Cottrell and his co-workers used only the high-to-low temperature transitions.

In the present work it was found useful (see also Seeger *et al.* 1957) to evaluate the data by a plot of $(\tau_1-\tau_2)$ against τ_2 which gives the linear relation

$$\tau_1-\tau_2=a_{12}+b_{12}\tau_2$$

already at relatively small strains, i.e. in stage II (not, however, during easy glide). This relation turns into Cottrell's $\tau_2/\tau_1=$ constant for large stresses $\tau_2\gg a_{12}$ where $\tau_2/\tau_1=1/(b_{12}+1)$. Figures 15 to 18 show the results for $(\tau_1-\tau_2)$ as a function of τ_2 on nickel for the temperatures T_1 and T_2 noted‡. The most detailed results, those on the temperature changes between 78° and 300°K (fig. 15), give an idea that the linear relation holds within reasonable limits for different crystals and different orientations. It appears that in this way the scatter is averaged out better than by determining individual ratios of τ_2/τ_1 at large τ_2. One can see that commercially pure nickel crystals show an anomalously large change in flow stress with temperature during easy glide (figs. 7 and 10). Even for pure nickel the $(\tau_1-\tau_2)$ values determined during easy glide lie consistently above the line obtained from stages II and III. The constant value of $(\tau_1-\tau_2)$ for small τ_2 fits with the one determined from the temperature dependence

† τ_2 denotes $\tau(T_2)$ in this section.

‡ We have always subtracted the transient yield phenomenon according to Haasen and Kelly (1957) in the determination of $(\tau_1-\tau_2)$, i.e. we have used the lower yield stress at the new temperature. This was not consistently done so by Adams and Cottrell (1955) and Rebstock (1957).

of the critical shear stress (§ 3). We should point out that temperature changes in both directions lead to about the same change in flow stress, and that no actual drop in load has been observed at 300°K after deformation at a lower temperature, as occurred in Cu and Al.

Fig. 15

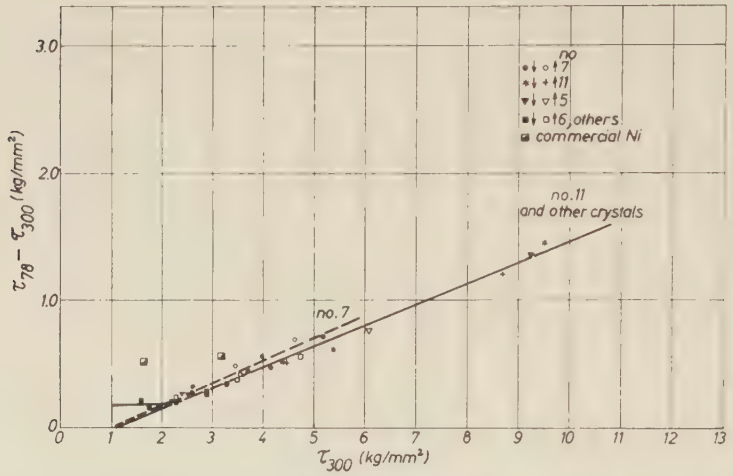

Change in flow stress after a temperature change between 78°K and 300°K, measured at different values of the room temperature flow stress τ_{300}. (The arrows give the direction of the temperature change.)

Fig. 16

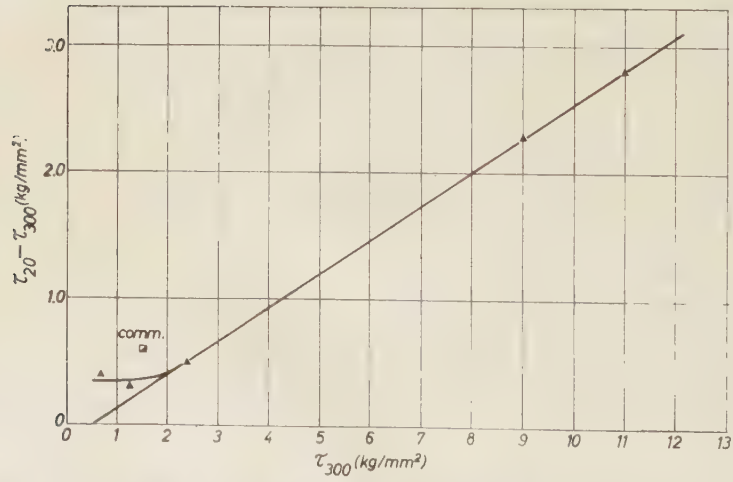

Change in flow stress after a temperature change between 20°K and 300°K measured at different values of the room temperature flow stress τ_{300} on 99·98 nickel and 99·4 nickel (marked comm.).

From figs. 15 to 18 we get for the changes between the temperatures of liquid hydrogen (H), nitrogen (N), dry ice in trichlorethylene (I) and room temperature (R) the values $b_{RH}=0{\cdot}27$, $b_{NH}=0{\cdot}065$, $b_{RN}=0{\cdot}167$ or

Fig. 17

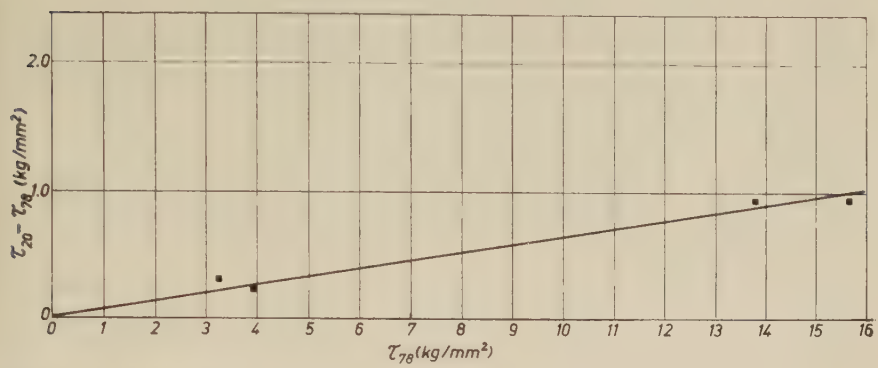

Change in flow stress after a temperature change between 20°K and 78°K measured at different values of the flow stress at 78°K, τ_{78}.

Fig. 18

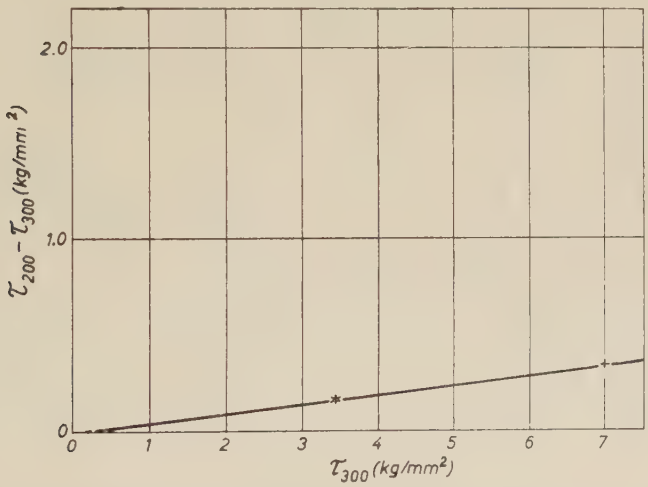

Change in flow stress after a temperature change between 200°K and 300°K measured at different values of the room temperature flow stress τ_{300}.

0·18 and $b_{RI}=0{\cdot}05$. From these b's the ratios $\tau_I/\tau_H=1/(b_{TH}+1)$ were calculated. For the transition between 20° and 300°K the flow stress ratio could also be obtained from

$$\tau_{300}/\tau_{20}=(\tau_{300}/\tau_{78})(\tau_{78}/\tau_{20})=0{\cdot}805 \text{ or } 0{\cdot}796$$

compared with $\tau_{300}/\tau_{20}=0{\cdot}788$ by direct transition.

$$\tau_{200}/\tau_{20}=(\tau_{200}/\tau_{300})(\tau_{300}/\tau_{20})=0{\cdot}827$$

was obtained only via the transition to room temperature. The flow stress at T_2 relative to that at $T_1 = 20$ °K has been plotted against temperature T_2 in fig. 19. For comparison τ_T/τ_{20} for Cu and Al are also given in fig. 19. Values of τ_T/τ_{90} for Cu with T between 473 °K and 90°K, measured by Adams and Cottrell (1955), were referred to 20 °K according to $\tau_T/\tau_{20} = (\tau_T/\tau_{90})(\tau_{90}/\tau_{20})$ with $\tau_{90}/\tau_{20} = 0{\cdot}978$ taken from our own measurements on Cu crystals. For Al the data of Cottrell and Stokes (1955) between 78°K and 423 °K were combined with those of Basinski (1957) on polycrystalline, solution-treated 24S Al between 20 °K and 80°K. They fit together surprisingly well. Comparing the three face-centred cubic metals in fig. 19, the curve of nickel is intermediate between those of Cu and Al and on the whole more similar in shape to that of Al although the change in slope occurs at a somewhat higher temperature (190°K for Ni, 120°K for Al).

Fig. 19

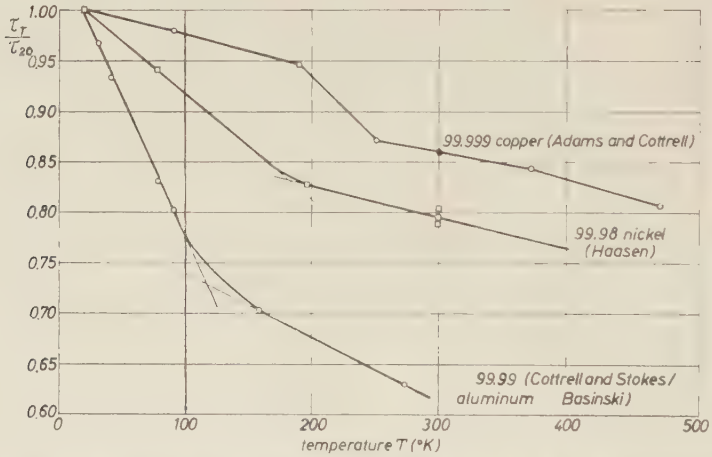

Ratio of the flow stresses at temperature T and at 20°K *vs* temperature T for nickel, copper (Adams and Cottrell 1955), and aluminium (Cottrell and Stokes 1955, Basinski 1957). (The *average* values of Adams and Cottrell's measurements on Cu have been referred to 20°K as stated in the text. τ_{300}/τ_{20} is taken from our own measurements on copper.)

§ 5. Discussion

It is now generally agreed that work-hardening in face-centred cubic crystals is caused by two types of dislocation processes. In the first process, the dislocations spreading slip along the main glide planes cut other dislocations which do not lie in this plane. The production of *jogs* in this process and the movement of such jogs in screw dislocations by the creation of point defects require extra work to be done by the applied stress. In the second process dislocations are stopped in the crystal by reactions with dislocations of other slip systems leading to the formation of *Lomer–Cottrell dislocations*. More dislocations are piled up behind these

obstacles, and the elastic stress fields arising from these groups work-harden the crystal. In the following discussion these two contributions to the flow stress will be called (cf. Seeger *et al.* 1957) τ_S ('Schneidprozesse', dislocation cutting) and τ_G (the elastic interaction of dislocations is proportional to a shear modulus G). We will now discuss our measurements on work-hardening and flow stress during stages I and II in terms of these dislocation processes (§ 5.1). Stage III, the 'dynamical recovery' region (Diehl *et al.* 1955, Seeger *et al.* 1957), will be dealt with separately in § 5.2. We will base this discussion on recent reviews of the present state of the dislocation theory of work-hardening (Seeger *et al.* 1957, Seeger 1957) which was developed mainly on the basis of experiments on Al and Cu. The measurements on Ni support and extend these conclusions in many respects. In § 5.1 we will stress in particular the *relation* between the two methods of analysis of work-hardening used (§§ 3 and 4) which became evident during this work. The result of this discussion makes the temperature change method appear even more useful and attractive. In § 5.2 an evaluation of the data on the setting-in stress of stage III as a function of temperature leads to an estimate of the stacking fault energy of Ni relative to that of Cu.

5.1. *Stages I and II*

During stage I the crystal slides essentially on one set of slip planes. This means that only few Lomer–Cottrell dislocations are formed and the τ_G contribution is small. The long slip lines (Diehl *et al.* 1955, Mader 1957) and the dependence of stage I on the specimen diameter (in the order of magnitude of 1 mm) (Rebstock 1957) show that many dislocations leave the crystal through the surface. Accordingly, the rate of work-hardening is low as it is in close-packed hexagonal crystals. This 'laminar' flow is very sensitive to disturbances introduced by inhomogeneity of the deformation, growth defects of the crystal, and also the interference of other slip systems which is likely to occur at this stage if the orientation is unfavourable (near the boundaries of the stereographic triangle (Haasen and Leibfried 1952, Haasen 1953)). Accordingly, the work-hardening rate, ϑ_I, during easy glide depends strongly on orientation in our measurements on nickel crystals as well as those on copper.

The temperature dependence of the flow stress in this first stage is about that of the critical shear stress which has been treated quantitatively by Seeger (1955): the contribution of the dislocation cutting processes depends on temperature in the form

$$\left.\begin{aligned} &\tau_S(T) = \frac{U - kT\log(\dot{\epsilon}_0/\dot{\epsilon})}{v} \quad \text{for} \quad T \leqslant T_0 = \frac{U}{k\log(\dot{\epsilon}_0/\dot{\epsilon})} \\ &\tau_S(T) = 0 \qquad \text{for} \qquad T \geqslant T_0 \end{aligned}\right\} \tag{1}$$

where U is the activation energy of the process (jog formation or creation of vacancies and interstitials), $v = bdl$, b = strength of the dislocation.

d = diameter of the intersected dislocation or of a point defect, l = spacing of the dislocation forest or distance between jogs, $\dot{\varepsilon}$ = strain rate. The flow stress contribution τ_G of the elastic interaction of dislocations in the crystal depends on temperature only as the shear modulus: $\tau_G = \alpha b G \sqrt{N}$ where N is the dislocation density (cm^{-2}), α a constant of order of magnitude 1/10 (Seeger 1957).

One thus obtains a critical shear stress $\tau_0 = \tau_S + \tau_G$ which decreases linearly with increasing temperature at low temperatures and is about constant at higher temperatures. Our results on $\tau_0(T)$ by direct measurement on different crystals or—more reliably—by temperature change during stage I agree with such a general behaviour, the main rise in τ_0 for nickel being below 100°K. A quantitative analysis of τ_0 in terms of eqn. (1), as in the case of copper (Seeger 1955), faces serious difficulties: in order to separate τ_G one has to know the temperature dependence of the shear modulus of *as-grown* nickel crystals. This depends sensitively on crystal perfection, due to the ferromagnetic ΔE-effect, even below room temperature. It is believed that the large scatter we observed in the critical shear stress just reflects different elastic moduli. After some percent deformation the ΔE-effect almost disappears and a unique temperature dependence of the moduli may be determined (see p. 410). Thus the method of temperature changes after some deformation, as described below, seems to be more reliable for an analysis of $\tau_S(T)$ than the direct measurement of the critical shear stress, in the case of nickel crystals. It should be noted, though, that the measurements of Andrade and Henderson (1951) not only show higher absolute values of τ_0 but also a 30% increase in τ_0 going from 300°K to 90°K while ours exhibit only a 10% change in the same temperature range.

The stress τ_{II} where rapid hardening starts is thought to be identical with the critical shear stress of certain secondary glide systems (Seeger 1957), the dislocations of which efficiently block the path of dislocations of the main slip system. From eqn. (1) it follows that the temperature dependence of τ_{II} is stronger than that of τ_0 since v^{-1}, i.e. the density of the dislocation forest, is larger as seen from the secondary systems (many dislocations of the main system cutting) than seen from the main system (fewer dislocations of the secondary systems intersecting), see also Barrett (1952). This strong temperature dependence of τ_{II} explains the strong rise of a_{II} at lower temperatures.

After the stress τ_{II} is reached the secondary slip systems continually interfere (Rebstock 1957) with slip on the main system which carries the deformation according to the law of maximum shear stress. No break in the shear stress shear strain curve could be observed when the tensile axis reached the symmetric position where the conjugate slip system takes over (Osswald 1953). During stage II the length of the active slip lines has been observed (Rebstock 1957) to decrease with increasing strain which is consistent with the idea of a formation of more and more Lomer–Cottrell dislocations. The groups of dislocations piled up at these

obstacles make the τ_G contribution to work-hardening gain in importance. τ_S is, however, also rising with deformation as $\varepsilon^{\frac{1}{2}}$ increases. It will be shown now that the temperature dependence of ϑ_{II}, the rate of rapid hardening, and of τ_2/τ_1, the reversible change in flow stress, is largely due to $\tau_S(T)$. Furthermore, both these quantities give identically the same information on τ_S.

We start from our empirical result that during stage II (and III) the flow stress before and after a change in temperature (between the temperatures T_1 and T_2) depends on work-hardening (as measured by τ_2) in the form

$$\tau_1 - \tau_2 = a + b\tau_2. \qquad (2)$$

The flow stress at any temperature is composed of the two contributions

$$\tau = \tau_S + \tau_G \qquad (3)$$

where for a given dislocated state of the crystal the definition of τ_G implies

$$\frac{\tau_{G_1}}{\tau_{G_2}} = \frac{G_1}{G_2}. \qquad (4)$$

Accordingly (2) turns into

$$\tau_1 - \tau_2 = \tau_{S_1} - \tau_{S_2}\frac{G_1}{G_2} + \tau_2\left(\frac{G_1}{G_2} - 1\right). \qquad (5)$$

Now τ_S also depends on work-hardening (measured by τ). According to the experiment, eqn. (2), this dependence is not stronger than linear (we will see below that it is found by measurement to be not less than linear either). Our assumption is therefore

$$\tau_S = \alpha + \beta\tau. \qquad (6)$$

From (5) and (6) it follows

$$\tau_1 - \tau_2 = \frac{\alpha_1 - \alpha_2(G_1/G_2)}{1-\beta_1} + \tau_2\frac{(1-\beta_2)G_1/G_2 - (1-\beta_1)}{1-\beta_1}. \qquad (7)$$

Comparison with (2) gives $\alpha = \tau_S(\tau = 0)$ and $\beta = d\tau_S/d\tau$ in terms of the measured quantities a and b if $G(T)$ is known. Following Cottrell and Stokes (1955,) Adams and Cottrell (1955) we have defined in § 4 a flow stress ratio for large deformations

$$\frac{\tau_2}{\tau_1} = \frac{1}{b+1}.$$

By means of (7) this turns into

$$\frac{\tau_2}{\tau_1} = \frac{1-\beta_1}{1-\beta_2}\frac{G_2}{G_1}. \qquad (8)$$

Cottrell *et al.* also discuss a corrected flow stress ratio $M \equiv \tau_2 G_1/\tau_1 G_2$ which means

$$M = \frac{1-\beta_1}{1-\beta_2} = \frac{1-(d\tau_S/d\tau)_1}{1-(d\tau_S/d\tau)_2}. \qquad (9)$$

The deviation of M from 1 in the measurements on Al and Cu shows that $d\tau_S/d\tau > 0$ (see (6)). It should be noted that the corrected flow stress

ratio as a function of temperature (T_2) does not directly give the temperature dependence of τ_S. From Seeger's expression (1) it follows

$$M \quad \frac{\tau_2}{\tau_1}\frac{G_1}{G_2} = \frac{1+\tau_{S_1}(d\log v/d\tau)_1}{1+\tau_{S_2}(d\log v/d\tau)_2}. \qquad (10)$$

In a plot of M against T_2 rapid changes of $\tau_\zeta(T_2)$ will show up, so that the corresponding critical temperatures T_0 can be determined in this way. However, in order to determine $\tau_\zeta(T)$ itself it is necessary to know $d\log v/d\tau$.

On the basis of this interpretation of the flow stress ratio we also understand the temperature dependence of the rate of work-hardening since the relation

$$\frac{\tau_2}{\tau_1}\frac{\vartheta_1}{\vartheta_2} = 1, \quad \vartheta \equiv \frac{d\tau}{da} \qquad (11)$$

is valid for any work-hardened state in stage II (and III) where flow stresses and work-hardening rates are measured at two temperatures T_1 and T_2.

To prove (11) we derive from (3)

$$\frac{d\tau}{da} = \frac{d\tau_G}{da} + \frac{d\tau_S}{da}$$

and from (6)

$$\frac{d\tau}{da} = \frac{d\tau_G}{da}\frac{1}{1-\beta}.$$

By definition (4) is again

$$\left(\frac{d\tau_G}{da}\right)_1 \Big/ \left(\frac{d\tau_G}{da}\right)_2 = G_1/G_2.$$

Thus with (8) one gets (11). To sum up we have shown that measurements of the flow stress ratio and work-hardening rates as a function of temperature yield the same information on $\tau_\zeta(T)$ if $G(T)$ is known†. The flow stress ratio is, however, much simpler to determine than the tangent of the flow stress-strain curves. If $G(T)$ is not known one cannot eliminate its effect on the flow stress ratio with the help of $\vartheta_{II}(T)$. On the contrary eqn. (11) offers a valuable cross check of the measurements by these two methods. In the case of our data on nickel $\tau_T/\tau_{20}(\vartheta_{II}(20\,°\text{K})/\vartheta_{II}(T)) = \text{constant} = 1{\cdot}05$ for $T = 78°$, $200°$ and $300\,°$K‡. As far as $\vartheta_{III}/\vartheta_{II} = \text{constant}$ independent of temperature (which is true for $78°$, $200°$, $300\,°$K for nickel) the relation (11)

† Preliminary dynamic measurements at Stuttgart on the temperature dependence of the elastic moduli of some of our nickel crystals *after deformation* indicate temperature coefficients $(dG/dT)/G \approx 4{\cdot}2 \cdot 10^{-4}$ °K between 200°K and 300°K and $(dG/dT)/G = 2{\cdot}5\times10^{-4}/°\text{K}$ near 150°K. The corrected flow stress ratio $M = \tau_2 G_1/(\tau_1 G_2)$ (fig. 19) and the corrected rapid hardening rate ϑ_{II}/G (fig. 13) thus become *temperature independent* between about 200°K and 300°K while the respective rise with decreasing temperature below this range is diminished by $2{\cdot}5\times10^{-4}/°\text{K}$.

‡ The τ_2 τ_1 data for Al (Cottrell and Stokes 1955) and Cu (Adams and Cottrell 1955) and the scarce values on $\vartheta_{II}(T)$ available in the literature (Staubwasser 1954, Sosin and Koehler 1956, Noggle and Koehler 1957 and Berner 1957) indicate that (11) also holds for these metals.

also holds during stage III. We have, however, pointed out already in § 3 that $\vartheta_{III}/\vartheta_{II}$ is abnormally high for $T = 20°K$ so that (11) fails here also. We think that the discontinuities of flow to be discussed in § 6 are responsible for the high ϑ_{III} at 20 K and may be also for a 5% too high a value of ϑ_{II} at 20°K causing the slight deviation from (11) in stage II (see fig. 13).

The validity of the relation (11) and therefore (6) essentially shows that the contributions to flow stress of the dislocation cutting process, τ_S, and of the elastic interaction of dislocations, τ_G, are proportional to each other. This fundamental law has already been anticipated by Cottrell and Stokes (1955), and Seeger (1955).

According to the measurements, eqn. (2) and the equations derived from it do not hold for stage I where presumably τ_S has a major share of the flow stress and is not proportional to τ_G. The anomalously large change in flow stress for commercial nickel during stage I could mean that the dislocation forest is different from that of high purity nickel. There is also the possibility that typical alloy hardening effects come into play here like the necessity to destroy non-random distributions of the component atoms at the beginning of slip.

5.2. *Stage III*

It has been shown in § 3 that the work-hardening rate decreases at higher deformation as a consequence of what has been called 'dynamical recovery'. The resulting stage III is approximately linear and extends over about 40% strain in the case of nickel. This stage sets in at a critical stress τ_{III}, the strong temperature dependence of which will now be analysed in terms of a dislocation model proposed by Diehl *et al.* (1955). These authors ascribe dynamical recovery to the escape of screw dislocations from the main slip planes by means of thermally activated and stress-aided cross-slip†. This assumption is supported by the observation of cross-slip lines with the electron microscope at the beginning of stage III (Diehl *et al.* 1955, Mader 1957)‡. The screw dislocations mobilized in this way from piled-up groups can promote strain and diminish the flow stress thus leading to a reduced rate of work-hardening.

Figure 20 illustrates the critical step of the cross-slip process. An extended dislocation in the main slip plane (111), width $2\eta_0$, recombines

† In 1954, Leibfried and Haasen concluded that thermally activated cross-slip is responsible for the gross temperature dependence of the stress–strain curve of face-centred cubic crystals. The specific process considered at that time was the formation of slip lamellae, out of a work-hardened slip plane, at high temperatures and large strains.

‡ *Note added in proof.*—Dr. S. Mader, Stuttgart, has investigated recently one of our nickel crystals of orientation No. 6 by the electron-microscopic techniques he has developed for copper. He found essentially *no* cross-slip at $\tau = 4{\cdot}1$ kg/mm² which is *below* our $\tau_{III} = 5{\cdot}5$ kg/mm² at 300°K.

over a certain length $2l_0$ and separates again into partial dislocations in the cross-slip plane $(11\bar{1})$ where it is now free to move. The activation energy for this process has been calculated by Schoeck and Seeger (1955). For a stress of the magnitude of the critical shear stress τ_0 acting in the corss-slip plane the activation energy E_0 turns out to be about 1 ev for aluminium, 10 ev for copper. The difference is caused by the respective widths of the stacking faults in dislocations in these metals which are determined mainly by stacking fault energies γ of 200 erg/cm² for Al, 40 erg/cm² for Cu. We will try now to estimate E_0 and accordingly γ for nickel from our measurements on stage III.

Fig. 20

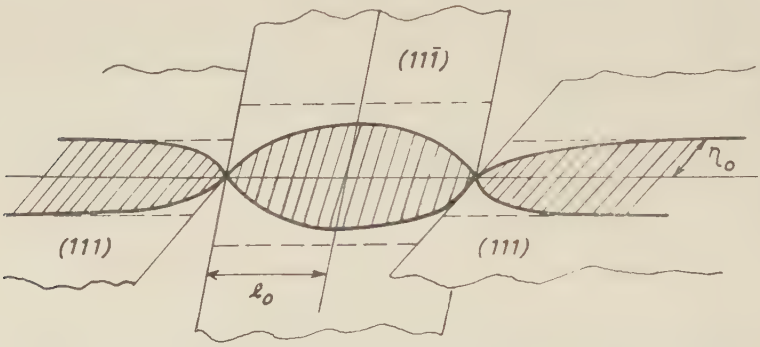

Cross-slip of extended screw dislocation (Schoeck and Seeger 1955).

For this purpose we make use of the stress dependence of the activation energy for cross-slip also calculated by Schoeck and Seeger (1955). It is obvious from the magnitude of E_0 particularly for Cu that at normal temperatures the applied stress has to contribute a sizeable part of the work to bring together the partial dislocations. The activation energy for cross-slip is lowered by the stress τ according to

$$E = E_0 - c \log (\tau/\tau_0) \quad . \quad . \quad . \quad . \quad . \quad . \quad (12)$$

where $c = 0{\cdot}35$ ev for Al, $3{\cdot}2$ ev for Cu per order of magnitude change in stress in the interesting stress range $(10^{-3}G)$ (Schoeck and Seeger 1955). Here τ is the applied stress *times* n, the number of dislocations in a piled-up group, i.e. τ is the stress acting on the leading dislocation of the pile-up. There is considerable experimental evidence (Seeger 1957) suggesting that n is a constant, about 20 to 30, during stages II and III of work-hardening. Given the stress and the temperature the rate ν of cross-slip is expected to follow from

$$\nu = \nu_\infty \exp(-E(\tau)/kT). \quad . \quad . \quad . \quad . \quad . \quad . \quad (13)$$

It is now assumed that the beginning of stage III is characterized by this rate ν reaching a certain value ν_{III} which is constant for different temperatures and metals. Then the temperature dependence of the corresponding stress τ_{III} follows from (12) and (13) as

$$\log \tau_{III} = \left(\frac{E_0}{c} + \log \frac{\tau_0}{n}\right) - \frac{kT}{c} \log \frac{\nu_\infty}{\nu_{III}}. \quad . \quad . \quad . \quad (14)$$

We have already shown in § 3, particularly fig. 14, that the stresses τ_{III} we have found for nickel as well as those measured on copper by Blewitt *et al.* (1955) and Berner (1957) depend on the temperature in the form† $\log \tau_{III} = A - BT$. We are now able to estimate E_0(Ni) and c(Ni) from the measured constants A and B, § 3.6, when we eliminate the parameters $\log n$ and $\log (\nu_\infty/\nu_{III})$ in (14) by means of the corresponding measurements on Cu. It seems reasonable to assume that these parameters are about equal for the two metals at the beginning of their respective stages III. For τ_0 we have chosen the low temperature critical shear stress as a representative stress level at which we can compare the activation energies E_0 of the two metals ($\tau_0 = 1000$ g/mm² for Ni, $\tau_0 = 250$ g/mm² for Cu (Blewitt), $\tau_0 = 200$ g/mm² for Cu (Berner)). The result of the analysis of the beginning of dynamical recovery, as pictured in fig. 14, in terms of the theory of thermally activated cross-slip, expressed by eqn. (14), is $c(\text{Ni}) = 0{\cdot}92c(\text{Cu, Blewitt})$, or $c(\text{Ni}) \sim c(\text{Cu, Berner})$ and $E_0(\text{Ni}) = 0{\cdot}81E_0(\text{Cu, Blewitt})$ or $E_0(\text{Ni}) = 0{\cdot}82E_0(\text{Cu, Berner})$.

These activation energies E_0 for cross-slip are (like the widths of the stacking faults) proportional to $G\gamma$ where G, the shear modulus, is 80% larger for nickel than for copper (at 300° K). From this and from the measured E_0's we derive a stacking fault energy for nickel of the magnitude

$$\gamma_{\text{Ni}} = \frac{E_0(\text{Cu})G(\text{Ni})}{E_0(\text{Ni})G(\text{Cu})}\,\gamma_{\text{Cu}} = 2{\cdot}2\,\gamma_{\text{Cu}},$$

i.e. $\gamma_{\text{Ni}} = 90$ erg cm‡. This still relatively small stacking fault energy and the strong elastic repulsion of the partial dislocations place nickel with copper in the group of metals with widely extended dislocations as distinct from aluminium with its narrow stacking faults§.

There are some other theoretical and experimental published data concerning the stacking fault energy of nickel. In terms of electronic

† We have been unable to confirm the relation $\tau^2_{III}T$ = constant in the case of nickel. Such a temperature dependence of τ_{III} has been proposed by Friedel (1955) considering a breakdown of Lomer–Cottrell dislocations at high stresses. This mechanism did not account for the data on copper either.

‡ We have tried to determine γ directly from the stress τ^0_{III} extrapolated to $T = 0$ where the partial dislocations must be brought together without any thermal activation. In the pertaining relation (Seeger 1957)

$$\tau^0_{III} = 2G(0{\cdot}056 - \gamma/Gb)/n,$$

however, the second term in the brackets is small compared to the first. Thus, γ cannot be obtained accurately from this equation (which yields reasonable values for n).

§ For Al single crystals only a few values of τ_{III} have been published (Staubwasser 1954, Sosin and Koehler 1956, Jaoul 1957) which were measured at temperatures low enough to give a well-developed stage II. Evaluation of these data along the lines of this section yields

$$\frac{c(\text{Al})}{c(\text{Cu})} \approx \frac{E_0(\text{Al})}{E_0(\text{Cu})} \lesssim 0{\cdot}4.$$

Therefore γ for Al is much higher than for Cu, as has been expected. The difference between the calculated (Schoeck and Seeger 1955) and observed ratios of $c(\text{Al})/c(\text{Cu})$ and $E_0(\text{Al})/E_0(\text{Cu})$ is attributed to the rather high values of τ_{III} used at room temperature where stage II is barely existent for Al.

structure there is no reason why nickel, situated between cobalt ($\gamma = 10$ erg/cm^2) and copper ($\gamma = 40$ erg/cm^2) in the periodic table, should have a high stacking fault energy, as Seeger (1955) has pointed out. The overlap of 3d electrons of neighboured atoms is small at the end of the third long period, and so is the difference in energy between the stacking orders ABCABC and ABABAB of close-packed planes. Actually, a hexagonal phase of Ni has been obtained by condensation from the vapour at low temperatures (Reimer 1957). Since the energy of a twin boundary and the stacking fault energy are closely related to each other in the face-centred cubic lattice, the large frequency of twins in Ni after recrystallization also suggests a low γ.

A more direct observation of stacking faults in nickel results from an analysis of shifts of Debye–Scherrer lines after filing (Paterson analysis). Smallman and Westmacott (1957) determine the stacking fault probability of nickel to be about half of that for copper, indicating $\gamma_{Ni} \gtrsim \gamma_{Cu}$. Christian and Spreadborough (1956) conclude from line shifts and the change of electrical resistivity with deformation that nickel belongs in a class with copper regarding its stacking fault energy. Seeger (1955) interprets older data on the plastic properties of nickel to yield $\gamma_{Ni} = 80$ erg/cm^2, in good agreement with our estimate.

The stacking fault energy discussed above is an important parameter in the theory of the critical shear stress and, in general, of the dislocation cutting process. This becomes more complex than indicated by (1) in the case of low stacking fault energy metals (Seeger 1955) and will not be treated here in detail.

§ 6. Discontinuous Slip and Mechanical Twinning

At large stresses, reached during deformation at low temperatures, Blewitt and co-workers (1957) found two types of irregularities in the stress–strain curves of copper single crystals. Type A, fig. 21 (*a*), shows up in the stress-strain curves, at 4·2 °K, of crystals whose initial orientation is in the [100] corner of the stereographic triangle. Type B, fig. 21 (*b*), is observed on crystals with orientation in the [111] corner, deformed at 4·2 °K. By means of a special x-ray technique (Sherrill *et al.* 1957) and by surface investigation after etching the big load drops in the B curves could be attributed to the formation of deformation twins, on {111} planes with ⟨112⟩ as shear direction. These twins spread across the specimen in the form of a Lüders band while the load fluctuates about the low value (2–3–4 in fig. 21 (*b*)). The serrations in A curves could be shown to belong to localized avalanches of slip. At 78 °K this discontinuous slip did not occur in crystals of any orientation while twinning has still been observed, near [111], starting from a neck in the specimen. In the meantime discontinuous slip also has been observed during low temperature deformation of many other polycrystalline metals (Basinski 1957, Wessel 1957).

Fig. 21 (*a*)

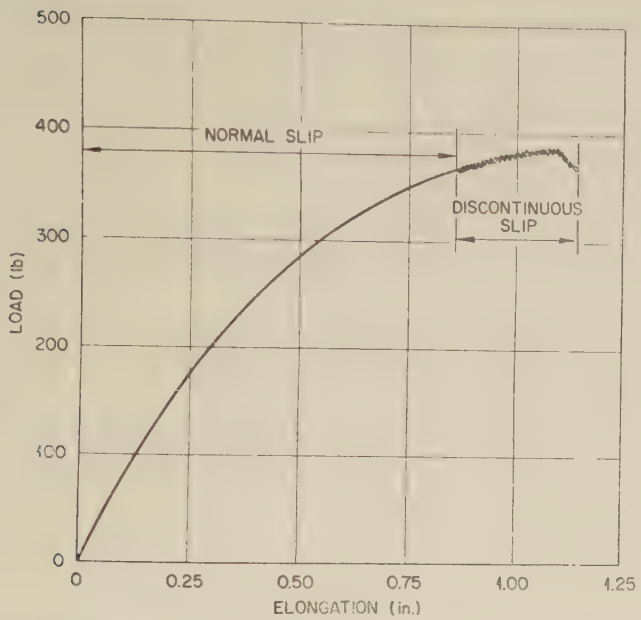

Discontinuous slip in copper single crystal at 4·2°K according to Blewitt *et al.* (1957).

Fig. 21 (*b*)

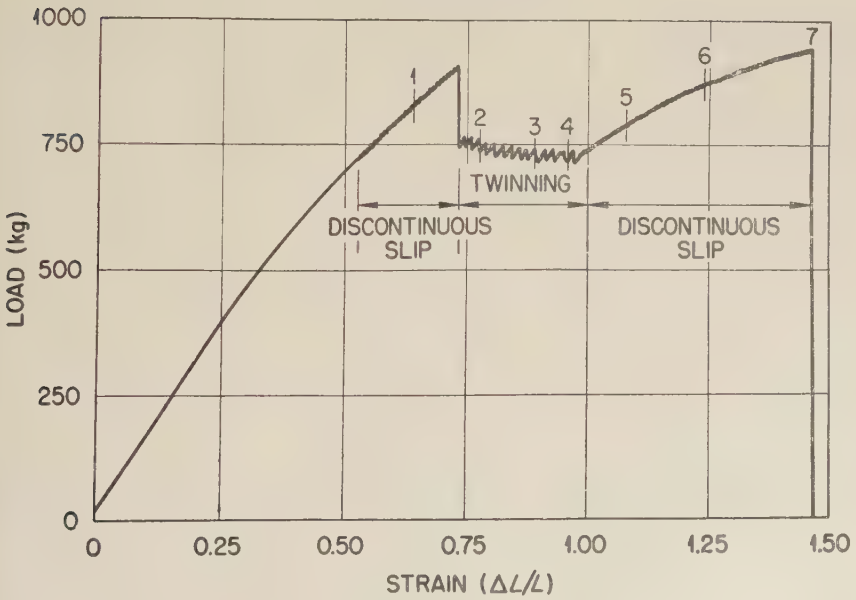

Discontinuous slip and twinning in copper single crystal at 4·2°K according to Blewitt *et al.* (1957).

It should be noted that Blewitt *et al.* (1957) found the twin plane to be identical with the main slip plane in most of the cases although twinning also has been observed on the conjugate slip plane, especially after neutron irradiation. By irradiation the flow stress level can be raised considerably so that a smaller amount of normal slip precedes twinning.

In a note added in proof to Blewitt's paper it is stated that Au and Ag† have been observed to twin in a similar fashion to Cu at 4·2°K and 78°K. No evidence of twinning has been found, however, in the cases of Al and Pb, deformed at 4·2 K. Such a difference in behaviour would just have been expected if twins were generated out of stacking faults in dislocations, and if the stacking fault energy determined the stress necessary to nucleate a twin. Actually, the stacking fault ribbon in an extended dislocation in the (111) plane can be considered a mono-atomic twin layer of finite width. If the stress is large enough to pull away one of the partial dislocations against the attraction of the surface energy of the stacking fault the latter can spread and, by means of a spiral mechanism, grow into a macroscopic twin. It seemed, therefore, worth while to look for mechanical twinning in nickel since the magnitude of the necessary stress might give one more clue for the stacking fault energy of nickel relative to that of copper and aluminium.

Rather unexpectedly no load drop of the kind of fig. 21 (*b*), indicating the formation of twins, could ever be observed with these nickel crystals, at temperatures of 4·2°, 20°, 78°, 200° and 300°K, even for orientations favourable for twinning according to Blewitt *et al.* (1957). The stress level in nickel was up to a factor of two higher than in copper. Since we were able to reproduce twinning in Cu in some test runs, our soft machine was not the reason for the failure to induce macroscopic twinning in Ni. Furthermore, two nickel crystals were pulled in Blewitt's hard machine at 4·2°K. Figure 22, Pl. 12 shows part of the chart of one of these runs (crystal no. 12b), indicating discontinuous flow in nickel at 4·2°K but no twinning load drops. Our machine did not record the small serrations but one could often see them directly on the pull-rod at 20°K.

Metallographic investigation of the nickel specimens deformed at 4·2° and at 20°K, however, frequently showed sharp bands near the necked down region (fig. 23 (*a*), Pl. 13) which were clearly different from the irregular low temperature slip lines present after heavy deformation. Polishing or etching did remove the slip lines but not the sharp bands (fig. 23 (*b*), Pl. 13). X-ray investigation, using Blewitt's and other oscillating techniques with monochromatic radiation, proved much more difficult in Ni than in Cu due to the stronger distortion of the nickel lattice. In one case only (crystal 12a) a reflection of a (111) twin could be identified, with (111), [$\bar{1}$10] as the main slip system. The twin plane in this case is identical with the 'unpredicted' slip plane (Cahn 1951) which comes into action at the [010]–[011] boundary of the stereographic triangle. The sharp bands visible on this crystal also had the orientation of the

† See also the recent investigation of Suzuki and Barrett (1958).

'unpredicted' slip plane while other crystals deformed at 20°K showed 'twin' bands parallel to the conjugate slip plane $(\bar{1}1\bar{1})$.

We have to conclude that in nickel it takes the stress concentration of a neck in the specimen to induce what appear to be twins, even at 20°K, while copper shows twinning clearly at 78°K. Thus, either the stacking fault energy γ of nickel is considerably higher than that of copper, or, if we rely on our estimate of a rather low γ from the dynamical recovery data (§ 5), we are left to assume that other factors besides γ also determine the formation of mechanical twins in face-centred cubic crystals†. We think that the large work-hardening capacity and the corresponding high dislocation density of deformed Ni impede the formation of macroscopic twin lamellae (see also Suzuki and Barrett 1958). Discontinuous slip on the other hand seems to be necessarily connected with the high stress level reached in low temperature deformation where at the head of only a few piled-up dislocations the theoretical shear strength is reached and new dislocations are generated freely (Seeger 1957, Haasen 1958).

Acknowledgments

The author would like to express his deep gratitude to the members of the Institute for the Study of Metals, University of Chicago, and especially to its Directors, Professor C. S. Smith and Professor E. A. Long, for their help and encouragement during the experiments. He wishes to acknowledge in particular the assistance of Professor C. S. Barrett and Dr. L. Castelitz in the x-ray work, of Professor L. Meyer in the liquid hydrogen experiments, of Mr. K. K. Ikeuye in growing the single crystals, and of Mrs. B. Nielsen in the metallographic work. Mr. W. Rosenkrantz has helped in calculations. The excellent work of the Central machine shop is very much appreciated.

The experiments using liquid helium were made possible by a kind invitation of the Solid State Division of Oak Ridge National Laboratory. During this work the author enjoyed in particular the cooperation of Dr. T. H. Blewitt and Dr. T. S. Noggle.

The evaluation of the data was carried out at Stuttgart. Here the author is indebted to Professor W. Köster and Professor U. Dehlinger for support and encouragement, and Dr. J. Diehl and Dr. A. Seeger for valuable discussions. They and Dr. T. B. Massalski, Birmingham, have kindly commented on the manuscript.

References

Adams, M. A., and Cottrell, A. H., 1955, *Phil. Mag.*, **46**, 1187.
Andrade, E. N. da C., and Aboav, D. A., 1957, *Proc. roy. Soc.* A, **240**, 304.
Andrade, E. N. da C., and Henderson, C., 1951, *Phil. Trans. roy. Soc.*, **244**, 177.
Barrett, C. S., 1952, *Structure of Metals* (New York : McGraw-Hill), p. 370.

† We could not produce deformation twins in annealed α-brass crystals, at 78°K and at 20°K. In 70 : 30 brass γ is particularly low (Smallman and Westmacott 1957, Christian and Spreadborough 1956).

Basinski, Z. S., 1957, *Proc. roy. Soc.* A, **240,** 229.
Berner, R., 1957, *Diploma Thesis*, Stuttgart, to be published.
Blewitt, T. H., 1953, *Phys. Rev.*, **91,** 1115.
Blewitt, T. H., Coltmann, R. R., and Redman, J. K., 1955, *Report Bristol Conference on Defects in Crystalline Solids* (London: Physical Society), p. 369; 1957, *J. appl. Phys.*, **28,** 651.
Cahn, R. W., 1951, *J. Inst. Met.*, **79,** 129.
Christian, J. W., and Spreadborough, J., 1956, *Phil. Mag.*, **1,** 1069.
Cottrell, A. H., and Stokes, R. J., 1955, *Proc. roy. Soc.* A, **233,** 17.
Cupp, C. R., and Chalmers, B., 1954, *Acta Met.*, **2,** 803.
Davis, R. S., Fleischer, R. L., Livingstone, J. D., and Chalmers, B., 1957, *Trans. Amer. Inst. Min. Metall. Engrs*, **209,** 136.
Diehl, J., 1956 a, *Z. Metallk.*, **47, 331**; 1956 b, *Ibid.*, **47,** 411.
Diehl, J., Mader, S., and Seeger, A., 1955, *Z. Metallk.*, **46,** 650.
Friedel, J., 1955, *Phil. Mag.*, **46,** 1169.
Garstone, J., Honeycombe, R. W. K., and Greetham, G., 1956, *Acta Met.*, **4,** 485.
Haasen, P., 1953, *Z. Phys.*, **136,** 26; 1958, *J. Metals* (in the press).
Haasen, P., and Kelly, A., 1957, *Acta Met.*, **5,** 192.
Haasen, P., and Leibfried, G., 1952, *Z. Phys.*, **131,** 538.
Jaoul, B., 1957, *J. Mech. Phys. Sol.*, **5,** 95.
Lange, H., and Lücke, K., 1952, *Z. Metallk.*, **43,** 55; 1953, *Z. Metallk.*, **44,** 183.
Leibfried, G., and Haasen, P., 1954, *Z. Phys.*, **137,** 67.
Maddin, R., 1950, *Rev. sci. Instrum.*, **21,** 881.
Mader, S., 1957, *Z. Phys.*, **149,** 73.
Noggle, T. S., and Koehler, J. S., 1957, *J. appl. Phys.*, **28,** 53.
Osswald, E., 1933, *Z. Phys.*, **83,** 55.
Paterson, M. S., 1955, *Acta Met.*, **3,** 491.
Rebstock, H., 1957, *Z. Metallk.*, **48,** 206.
Reimer, L., 1957, *Phys. Verh.*, **8,** 48; see also Masing G., 1950, *Lehrbuch der allg. Metallkunde* (Berlin: Springer), p. 476.
Rosi, F. D., 1954, *Trans. Amer. Inst. Min. Metall. Engrs*, **200,** 1009.
Schmid, E., and Boas, W., 1935, *Kristallplastizität* (Berlin: Springer).
Schoeck, G., and Seeger, A., 1955, *Report Bristol Conference on Defects in Crystalline Solids* (London: Physical Society), p. 340.
Seeger, A., 1955, *Phil. Mag.*, **46,** 1194; 1957, *Report Lake Placid Conference on Dislocations and Mechanical Properties of Crystals* (New York: J. Wiley), p. 243.
Seeger, A., Diehl, J., Mader, S., and Rebstock, H., 1957, *Phil. Mag.*, **2,** 323.
Sherrill, F. A., Wittels, M. C., and Blewitt, T. H., 1957, *J. appl. Phys.*, **28,** 526.
Smallman, R. E., and Westmacott, K. H., 1957, *Phil. Mag.*, **2,** 669.
Sosin, A., and Koehler, J. S., 1956, *Phys. Rev.*, **101,** 972.
Staubwasser, W., 1954, *Thesis*, Göttingen and *Acta Met.*, **6,** 156.
Suzuki, H., and Barrett, C. S., 1958, *Acta Met.* (in the press).
vonGöler, K. F., and Sachs, G., 1927, *Z. Phys.*, **41,** 103.
Wessel, E. T., 1957, *Trans. Amer. Soc. Metals*, **49,** 149.

CORRESPONDENCE

Etching Patterns in High Purity Zinc

By F. C. Frank
University of Bristol, H. H. Wills Physics Laboratory, Bristol, 8

and Thad Vreeland, Jr.
Division of Engineering, California Institute of Technology,
Pasadena, California, U.S.A.

[Received January 29, 1958]

Servi (1958) has observed certain ridges on an otherwise smooth surface produced by the action of a special etching agent on zinc. He interprets these ridges as showing the course of dislocation lines pre-existing in the specimen, suggesting that accumulated solute near the dislocation lines has made the metal more etch resistant. No other interpretation seems probable, but Servi confesses to being unable to interpret certain features in his second picture, which appears to show a ' Frank–Read source ' in operation. These features, he says, are the central ' dip ' in the curve joining the two spiral centres, and two ' dots ' (we should say rather ' dashes ') near to it. He is in fact wrong to say that the first of these features is unexpected on the assumption that this is a ' Frank–Read source '. The conditions of motion of dislocation lines in this case are evidently such that a forward-facing ' vee ' in the line persists, instead of rapidly filling in (this implies strong frictional hindrance to the motion of these dislocation lines) : ' vees ' will then be produced at the place corresponding to Servi's dip in every operation of the source except the first. The ' dots ' or ' dashes ', however, remain to be explained. It is first necessary to point out that on any interpretation the etching process has made gaps in lines which must in reality have been continuous. The best we can therefore do is to fill in these gaps in the way which gives the simplest acceptable interpretation of what is seen. Figure 1, traced from Servi's fig. 1 (*b*), shows the visible lines of the pattern we have to complete. The first which occurred to us was that there were really two ' Frank–Read sources ' close together, as shown in fig. 2 (*a*). The other two fixed points of the sources would then be at the upper ends of the two dashes, which would represent the only visible portions of a short length of dislocation line in the form of a letter ω. This is the interpretation which requires the least length of gap, but the objection to it is that each source should have a re-entrant ' vee ' for itself—there should be three ' dips ' instead of one (fig. 2 (*b*)). The interpretation indicated in fig. 3 is free from this objection, and we can see no other unobjectional interpretation of comparable simplicity. In this, two dislocations emerge from each

Fig. 1

Fig. 2

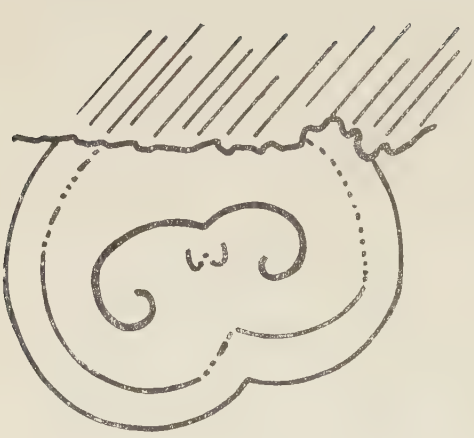

(*a*)

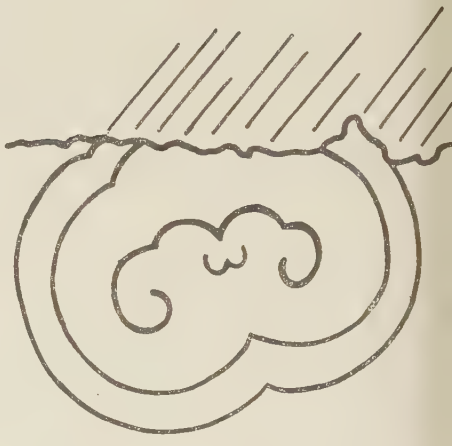

(*b*)

Fig. 3

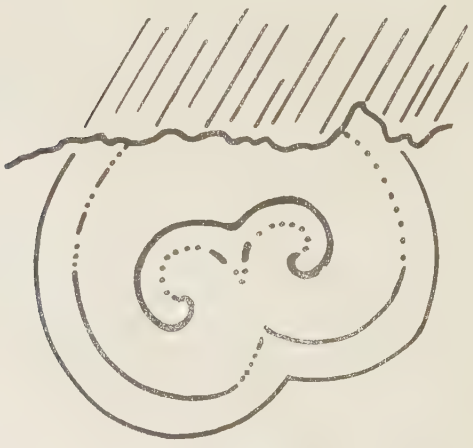

centre. All the gaps are in the second member of the pair. This may be explained by supposing that it collected less impurity because the first had swept the ground ahead of it. The strong frictional drag indicated by the configuration of the dislocation lines is attributable to interaction with the solute. Then the frictional force on the second would be less than that on the first, explaining the unequal spacing between the two spirals. We think this is rather more likely than the other possibility, that the two dislocations are a pair of partials in a very widely extended dislocation. A possibility not to be excluded on the evidence is that the broken and continuous lines, respectively, of fig. 3, show two successive positions of the same dislocation lines, at each of which they have rested long enough for some segregation of solute to occur: so that only one dislocation line emerges from each centre.

REFERENCE

SERVI, I. S., 1958, *Phil. Mag.*, **3**, 63.

Evidence for the Trapping of Interstitial Atoms in Irradiated Tungsten

By M. W. THOMPSON
Metallurgy Division, A.E.R.E., Harwell

[Received December 16, 1957]

THE residual resistance of tungsten specimens has been measured at 4°K after reactor irradiation at −196°C. Exposure in the BEPO reactor at Harwell ($\sim 10^{12}$ n/cm^2/sec) for six days doubled the residual resistivity from its original value of 0·06 micro ohm cm. It has been reported elsewhere (Kinchin and Thompson 1958) that the recovery of such an increase occurs in two main stages of roughly equal magnitude: one centred at −80°C with an associated activation energy of 0·48 ev and one at 320°C with 1·7 ev. Slight recovery, however, occurs over the whole range of observation from −196 to 450°C. On the limited evidence of this work it was suggested that the recovery in the −80°C stage is due to interstitials becoming mobile and that in the 320°C stage to the migration of single vacancies. Recovery in the intermediate range and at temperatures above 320°C was attributed to the release of trapped defects and to the migration of vacancy clusters.

The experiment to be discussed below has provided evidence for the trapping of interstitials. A tungsten specimen was irradiated for 1 hour which caused an increase in residual resistance of 0·91% (±0·01%). Annealing periods of 30 minutes at −40, 100, 200 and 350°C respectively produced the recovery curve shown in the diagram. The specimen was heated to 1500°C which restored its resistance to the pre-irradiation value, it was then irradiated for 12 hours which caused a resistance increase of

8·81%. Annealing was carried out as before and this recovery curve is also shown in the diagram. The most obvious difference between these results and those reported previously is the absence of any large change in resistance after annealing at −40°C. It is also clear that although increasing the irradiation time to 12 hours causes more recovery at 100°C and 200°C there is still very little change at −40°C.

These results may be explained by postulating the existence of several types of trap to which interstitial atoms could become attached (Lomer and Cottrell 1955). Such traps could presumably take the form of substitutional impurity atoms whose size is less than that of the tungsten atom. A rough lower limit to the concentration of traps may therefore be taken as the concentration of impurity atoms: this quantity may be deduced from the spectroscopic analysis and the residual resistivity to be about 10^{-4}. Now after a 1 hour irradiation the observed increase in resistivity indicates a concentration of displaced atoms of the order 10^{-6}.

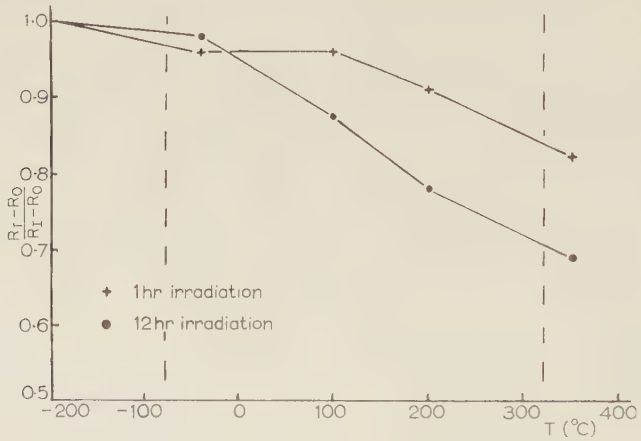

$(R_T-R_0)/(R_I-R_0)$ versus annealing temperature. R_T=residual resistances after annealing at temperature T. R_0=residual resistance before irradiation. R_I=residual resistance immediately after irradiation. Dashed lines indicate the position of principal recovery stages observed after 6 day irradiations.

It is clear therefore that there are insufficient interstitials to fill all the traps. Under these conditions mobile interstitials will have a far greater chance of becoming trapped than of annihilating vacancies or of migrating out of the lattice. The slight recovery observed at low temperatures may be understood by supposing that interstitials released from post-irradiation positions by thermal excitation are immobilized again by the plentiful supply of traps and that such a process only causes small resistivity changes. The recovery observed at 100 and 200°C after the 12 hour irradiation may be explained by assuming that in this case there are insufficient deep traps to hold all the interstitials and that when migrating at these temperatures they will start to annihilate vacancies or will migrate out of the lattice, either process giving rise to larger changes in resistance.

The following question now arises: is the previous conclusion that interstitials are immobile in the lattice until −80°C correct, or are they mobile and become trapped at the irradiation temperature? In either case the mechanism of changing traps, proposed above, will explain the experimental results provided that the 'frozen in' interstitial is regarded as being a special type of trapped interstitial. However, if the former answer is correct then the amount of recovery at −40°C should reach a limiting value for long irradiations which produce sufficient interstitials to occupy all the traps. On the other hand if the interstitials are immobile at −196°C then their number should continue to increase until the concentration of defects is high enough to cause instantaneous recovery of further damage. For practical irradiation times in BEPO the recovery at −40°C would not show saturation in this case. Further experiments are proceeding in which recovery after longer irradiations will be studied.

Acknowledgments

My thanks are due to Dr. A. H. Cottrell for his guidance in this work and to Miss M. J. Stubbs who carried out the resistance measurements.

References

Kinchin, G. H., and Thompson, M. W., 1958, *J. Nuclear Energy*, February.
Lomer, W. M., and Cottrell, A. H., 1955, *Phil. Mag.*, **46**, 711.

REVIEWS OF BOOKS

Ferroelectricity in Crystals. By Helen D. Megaw. (London : Methuen and Co. Ltd.) [Pp. xi+220.] 27*s.* 6*d.*

Ferroelectricity is a branch of physics that has developed very rapidly in recent years. Until 1935 only one ferroelectric was known ; now many are known, and more are being discovered at an increasing rate. The volume of literature is so large that it is hard to keep up with it, and anyone starting work on the subject must find it very difficult to get an adequate picture of its present state. A general review of the subject was therefore badly needed, and it could hardly have been better done than in this book. It is surprising how much information has been put into 200 small pages. Little of importance seems to have been omitted, though naturally for a fuller development of some subjects the reader must refer to the original papers. This conciseness, without loss of clarity, has been obtained by careful arrangement and the author's sound judgment of what are the most significant facts in published work. As might be expected from Dr. Megaw's own interests emphasis has been placed on the crystal structure of the substances described, but this is quite right since an understanding of the nature of ferroelectrics must ultimately depend on a detailed knowledge of their atomic structure. Naturally the greater part of the book is devoted to experimental work, since in this subject theory has lagged far behind experiment : but three chapters of the book are devoted to theories of ferroelectricity, with an assessment of their merits.

It is to be hoped that this book will have the success it deserves, and that it will be possible to bring out second and subsequent editions at not too long intervals. A. F. D.

Constantes Sélectionnées : Diamagnétisme et Paramagnétisme, Relaxation Paramagnétique. By G. Foex, C. J. Gorter and L. J. Smits. (Paris : Masson & Cie.) [Pp. 325.] 8,800 *fr.* (clothbound) ; 9,700 *fr.* (stiff covers).

Apart from a brief section on paramagnetic relaxation (by Gorter and Smits), the tables deal mainly with susceptibility and provide a nice example of the well known distinction between the physicist, who makes accurate measurements on materials of unknown purity, and the chemist, who makes measurements of unknown accuracy of pure materials. The lack of cooperation between physicists and chemists is illustrated by the great rarity of entries in heavy type (indicating great reliability) or asterisks (indicating agreement between two or more authors to better than 1%). Probably the main value of tables such as these lies not so much in the numerical data they provide but in the bibliography ; here the bibliography is admirably organized, but is somewhat incomplete in the field most familiar to the reviewer. D. S.

Viscous Fluid Flow. II—Turbulent Flow. By Shih-I Pai. (Princeton, U.S.A. : D. Van Nostrand Co., Inc.) [Pp. 277]. 48*s.*

This book is an attempt to provide a survey of what is known about turbulent flow, presumably for American engineering students of the subject at post-graduate level. It is comprehensive so far as titles of chapters are concerned, but the treatment of the different aspects of turbulence is rather scrappy and superficial. The author has a bias towards those parts of the subject that lend themselves to mathematical description, and this leads him into making a curious and misleading selection of material. The more physical aspects are presented poorly, or left out altogether. This is not a book that the present reviewer would recommend. G. K. B.

[*The Editors do not hold themselves responsible for the views expressed by their correspondents.*]

Fig. 1

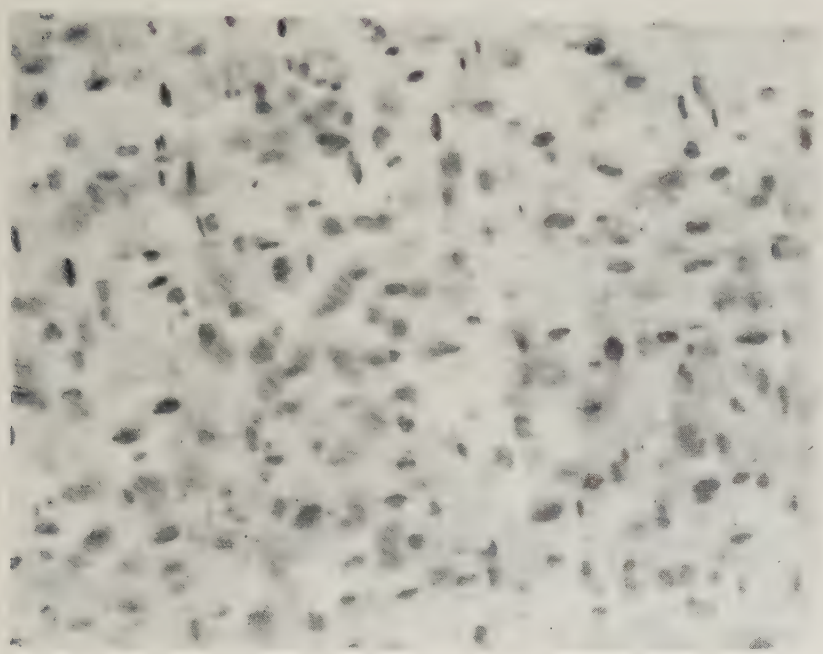

Platelets of gold produced by exposing and heating a silver chloride crystal containing 0·05 mol% aurous chloride. (×875.)

Fig. 2

Particles of gold with associated systems of decorated prismatic dislocations in a silver chloride crystal. The photomicrograph is taken in a (111) plane. (×875.)

Fig. 3

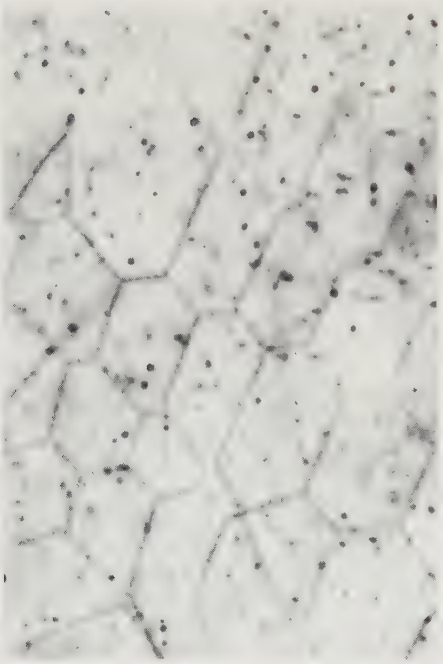

Hexagonal network within a silver chloride crystal. (×875.)

Fig. 7

Dislocations interacting with imperfections in a recrystallized silver chloride crystal. (×875.)

Fig. 4

The dislocations of tilt sub-boundaries and three dimensional networks within a well annealed silver chloride crystal. (×875.)

Fig. 5

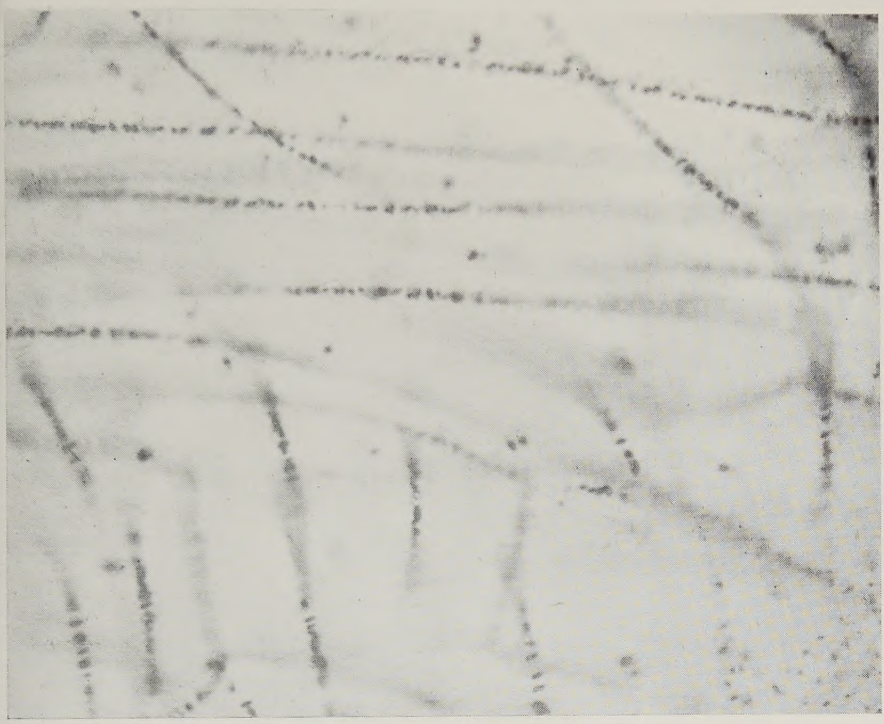

Dislocations introduced by straining a recrystallized silver chloride crystal. (×875.)

Fig. 6

Dislocations in a silver chloride crystal strained after recrystallization. (×875.)

Fig. 22

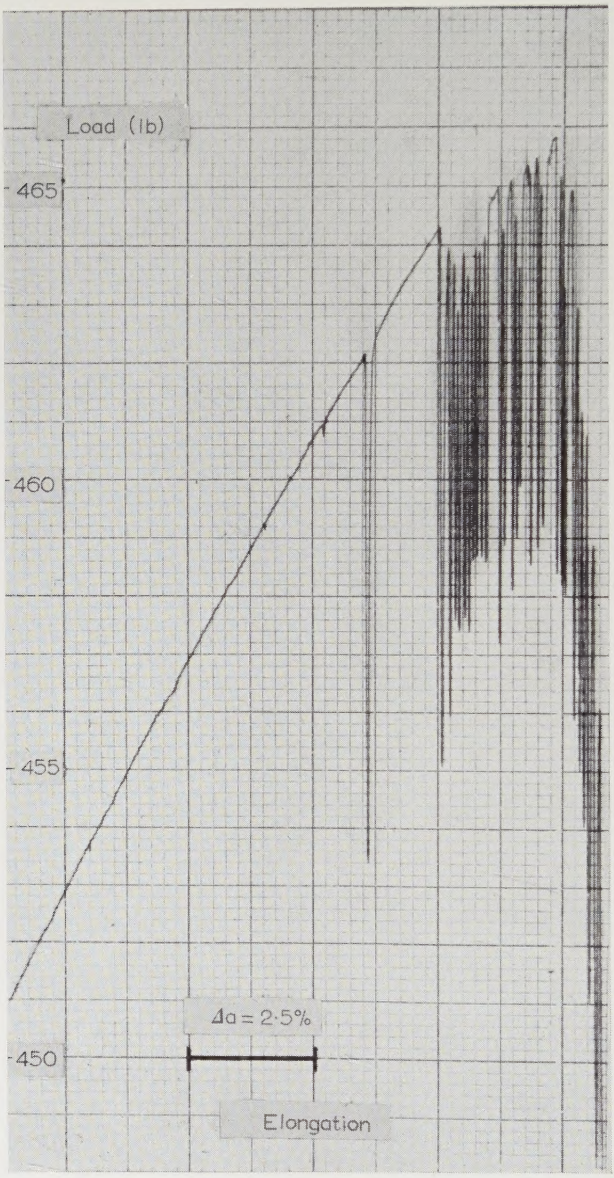

Discontinuous slip in nickel single crystal 12 at 4·2°K.

Fig. 23 (*a*)

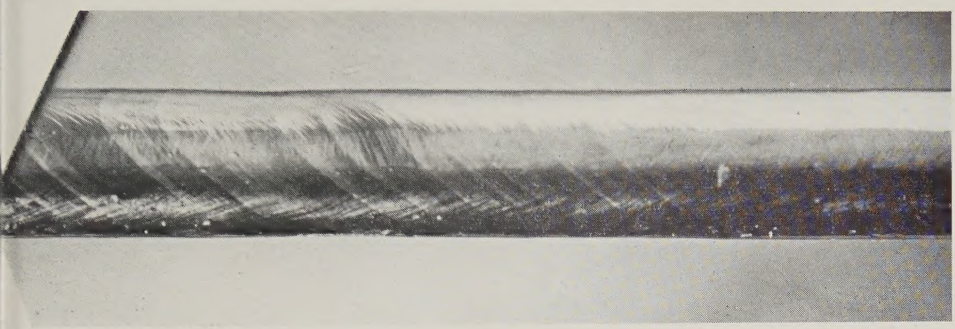

Nickel crystal 22c after 54% strain at 20°K. Magn. × 8·5.

Fig. 23 (*b*)

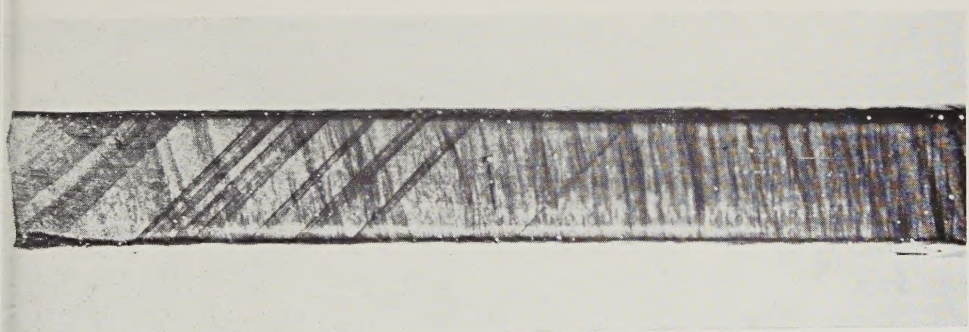

Nickel crystal 22c after 54% strain at 20°K, polishing, and etching. Magn. × 8·5. Neck at the left side of the picture.